Numerical Simulation of Stresses due to Solid State Transformations

The Simulation of Laser Hardening

Samenstelling van de promotiecommissie:

voorzitter en secretaris:	
Prof. dr. ir. H.J. Grootenboer	Universiteit Twente
promotor:	
Prof. dr. ir. J. Huétink	Universiteit Twente
leden:	
Dr. ir. J. Beyer	Universiteit Twente
Prof. dr. ir. M.G.D. Geers	Technische Universiteit Eindhoven
Prof. dr. ir. B. Koren	Technische Universiteit Delft
Prof. dr. ir. J. Meijer	Universiteit Twente
Prof. dr. I.M. Richardson	Technische Universiteit Delft
Prof. dr. ir. H. Tijdeman	Universiteit Twente

Numerical Simulation of Stresses due to Solid State Transformations
The Simulation of Laser Hardening
Geijselaers, H.J.M.

Thesis University of Twente, Enschede - with ref. with summary in Dutch.
ISBN 90-365-1962-4

Keywords: phase transformations, plasticity, residual stress, laser hardening, ALE method, steady state.

Cover designed by Karin van Beurden.
Printed by Ponsen & Looijen, Wageningen.

NUMERICAL SIMULATION OF STRESSES DUE TO SOLID STATE TRANSFORMATIONS

THE SIMULATION OF LASER HARDENING

PROEFSCHRIFT

ter verkrijging van
de graad van doctor aan de Universiteit Twente,
op gezag de rector magnificus,
prof. dr. F.A. van Vught,
volgens besluit van het College voor Promoties
in het openbaar te verdedigen
op vrijdag 17 oktober 2003 om 13.15 uur

door

Hubertus Josephus Maria Geijselaers

geboren op 20 april 1954
te Berg en Terblijt

Dit proefschrift is goedgekeurd door de promotor:

Prof. dr. ir. J. Huétink

Contents

summary

The properties of many engineering materials may be favourably modified by application of a suitable heat treatment. Examples are precipitation hardening, tempering and annealing. One of the most important treatments is the transformation hardening of steel. Steel is an alloy of iron and carbon. At room temperature the sollubility of carbon in steel is negligible. The carbon seggregates as cementite (Fe_3C). By heating the steel above austenization temperature a crystal structure is obtained in which the carbon does solve. When cooled fast the carbon cannot seggregate. The resulting structure, martensite is very hard and also has good corrosion resistance.

Traditionally harding is done by first heating the whole workpiece in an oven and then quenching it in air, oil or water. Other methods such as laser hardening and induction hardening are charaterized by a very localized heat input. The quenching is achieved by thermal conduction to the cold bulk material. A critical factor in these processes is the time required for the carbon to dissolve and homogenize in the austenite.

This thesis consists of two parts. In the first part algorithms and methods are developed for simulating phase transformations and the stresses which are generated by inhomogeneous temperature and phase distributions. In particular the integration of the constitutive equations at large time increments is explored. The interactions between temperatures, stresses and phase transformations are cast into constitutive models which are suitable for implementation into a finite element model.

The second part is concerned with simulation of steady state laser hardening. Two different methods are elaborated, the Arbtrary Lagrangian Eulerian (ALE) method and a direct steady state method. In the ALE method a transient calculation is prolonged until a steady state is reached. An improvement of the convection algorithm enables to obtain accurate results within acceptable calculation times.

In the steady state method the steadiness of the process is directly incorporated into the integration of the constitutive equations. It is a simplified version of a method recently published in the literature. It works well for calculation of temperatures and phase distributions. When applied to the computation of distortions and stresses, the convergence of the method is not yet satisfactory.

samenvatting

Van veel metalen kunnen de eigenschappen beinvloed worden door het toepassen van een geschikte warmtebehandeling. In de techniek is de belangrijkste warmtebehandeling het transformatieharden van staal. Staal is een legering van ijzer en koolstof. Op kamertemperatuur is de oplosbaarheid van koolstof in ijzer vewaarloosbaar, het scheidt uit in de vorm van cementiet (Fe_3C). Door het staal te verwarmen tot boven de austenitiseringstemperatuur wordt een kristalstructuur bewerkstelligd, waarin de koolstof wel oplost. Bij snelle afkoeling heeft het koolstof geen gelegenheid om uit te scheiden. De resulterende structuur, martensiet is zeer hard en heeft ook goede corrosie eigenschappen. Op de traditionele manier gebeurt het harden van staal door het werkstuk in zijn geheel op te warmen en vervolgens voldoende snel af te koelen. Bij andere methoden, zoals laser harden en inductie harden, wordt de warmte zeer lokaal toegevoerd. De snelle afkoeling wordt dan bereikt door warmtegeleiding naar het koude basismateriaal. Bij deze processen is het vooral van belang, dat een voldoende hoge temperatuur bereikt wordt om in zeer korte tijd de koolstof op te lossen en homogeen te verdelen in het austeniet.

Dit proefschrift bestaat uit twee delen. In het eerste deel worden de algorithmes en methoden uitgewerkt, waarmee het mogelijk wordt om de omvang van de fase transformaties te voorspellen alsmede de hiermee gepaard gaande restspanningen. Vooral aan een nauwkeurige beschrijving van de interacties tussen de temperaturen, spanningen en fase transformaties wordt aandacht besteed. Dit resulteert in een stelsel consistente vergelijkingen, waarmee het verloop van temperaturen, spanningen en fase transformaties kan worden beschreven. Een eindige elementen model is geformuleerd, waarin deze vergelijkingen zijn opgenomen.

In het tweede deel gaat de aandacht vooral uit naar beschrijving van stationair laserharden. Hiervoor worden twee verschillende methoden gebruikt, de Arbitrary Lagrangian Eulerian (ALE) methode en een directe stationaire methode. In de ALE methode wordt een transiente berekening net zolang doorgezet, totdat een stationaire situatie ontstaat. Mede door het gebruik van een verbeterd convectie algorithme is het mogelijk om hierbij met acceptabel rekentijden goede resultaten te behalen.

In de tweede methode is het stationair zijn van het process gelijk verwerkt in de integratie van de constitutieve vergelijken. Ze bouwt voort op een onlangs in de literatuur gepubliceerde methode, waarbij gepoogd is deze enigszins te vereenvoudigen. Toepassing voor berekening van temperaturen en fase verdelingen levert uitstekende resultaten. Bij de berekening van spanningen en vervormingen wordt echter nog geen bevredigende convergentie bereikt.

Nomenclature

Roman symbols

A_{M}	equivalent stress influence parameter for the martensite transformation
A_{τ}	equivalent stress influence parameter for the pearlite transformation
B_{M}	pressure influence parameter for the martensite transformation
B_{τ}	pressure influence parameter for the pearlite transformation
F	transformation plasticity function
G	shear modulus
H	enthalpy
K	transformation plasticity parameter
T	temperature
T_{Ms}	martensite start temperature
T_{A1}	A1 temperature 727°C
T_{A3}	A3 temperature
b	bulk related constitutive parameter
c	carbon content
c_{p}	specific heat
d	deviatoric constitutive parameter
f	generic data
$h_{(.)}$	normalized hardening parameter
k_{b}	bulk modulus
n	Avrami exponent
p	hydrostatic pressure
t	time
v	volume

Greek symbols

Δ	increment
Φ	yield surface
α	implicit time step parameter
α	thermal expansion coefficient
β	parameter in the Koistinen-Marburger equation
β	implicit time step parameter
γ	convective heat transfer coefficient
γ_{ij}	shear strain component
δ	iterative increment
ε^{p}	equivalent plastic strain

θ	implicit time step parameter
κ	thermal conductivity
λ	consistency parameter for plastic flow
ρ	mass density
σ_{eq}	von Mises equivalent stress
σ_{y}	yield stress
τ	phase transformation time constant
φ	phase fraction
$\bar{\varphi}$	equilibrium phase fraction
φ_0	initial phase fraction
φ^{α}	ferrite phase fraction
φ^{p}	pearlite phase fraction
φ^{γ}	austenite phase fraction
φ^{m}	martensite phase fraction

Vectors and tensors

$\mathbf{1}$	second order unit tensor
$\mathbf{D}$	constitutive stress strain behaviour
$\mathbf{E}$	fourth order elasticity tensor
$\mathbf{F}$	deformation gradient
$\mathbf{I}$	fourth order unit tensor
$\mathbf{Y}$	yield tensor
$\mathbf{c}_{\mathrm{T}}$	thermal stress constitutive terms
$\mathbf{c}_{\varphi}$	phase transformation stress constitutive terms
$\mathbf{d}$	strain rate tensor
$\mathbf{e}$	deviatoric strain tensor
$\mathbf{n}$	normal vector
$\mathbf{q}$	heat flow vector
$\mathbf{s}$	deviatoric stress
$\mathbf{t}$	boundary traction
$\mathbf{u}$	displacement vector
$\mathbf{v}$	velocity vector
$\boldsymbol{\varepsilon}$	strain tensor
$\boldsymbol{\sigma}$	Cauchy stress tensor
$\boldsymbol{\sigma}_1$	final stress
$\boldsymbol{\sigma}_{\mathrm{t}}$	trial stress

General subscripts and superscripts

$(.)^{\mathrm{el}}$	elastic part
$(.)^{\mathrm{m}}$	martensite
$(.)^{(\mathrm{m})}$	matrix material
$(.)^{\mathrm{p}}$	pearlite
$(.)^{\mathrm{pl}}$	plastic part
$(.)^{\mathrm{th}}$	thermal part
$(.)^{\mathrm{tp}}$	transformation plastic part
$(.)^{\mathrm{tr}}$	transformation part
$(.)^{\mathrm{v}}$	volume

$(.)^{\alpha}$	ferrite
$(.)^{\gamma}$	austenite
$(.)_0$	initial value
$(.)_1$	final value
$(.)_{\mathrm{c}}$	convective
$(.)_{\mathrm{eq}}$	equivalent
$(.)_{\mathrm{g}}$	grid
$(.)_{\mathrm{h}}$	discretized field
$(.)_{\mathrm{m}}$	material
$(.)_{\mathrm{n}}$	normal component
$(.)_{\mathrm{rc}}$	recovery
$(.)_{\mathrm{t}}$	trial value

Operators

$\dot{f}$	material time derivative of f
f'	derivative of f
$\mathbf{a}^{\mathrm{T}}$	transpose of a second order tensor
$\mathbf{ab}$	diadic tensor product: $C_{ijkl} = a_{ij} b_{kl}$
$\mathbf{a} \cdot \mathbf{b}$	vector dot product: $c = a_i b_i$
$\mathbf{a} \cdot \mathbf{b}$	single tensor contraction: $c_{ik} = a_{ij} b_{jk}$
$\mathbf{A} : \mathbf{b}$	double tensor contraction: $c_{ij} = A_{ijkl} b_{kl}$
$\mathrm{sym}(.)$	symetric part of a second order tensor: $\mathrm{sym}(\mathbf{a}) = \frac{1}{2}(\mathbf{a}^{\mathrm{T}} + \mathbf{a})$
$\mathrm{tr}(.)$	trace of a second order tensor
$\|.\|$	Euclidean norm
∇x	gradient of x

Part I

SIMULATION OF SOLID STATE TRANSFORMATIONS

1. Introduction

The equilibrium arrangement of atoms in metals in the solid state is an ordered regular pattern, the crystal structure. Which crystal structure is in equilibrium, often depends on the temperature. A phase with a certain crystal structure can be defined as a portion of a system, for instance an alloy, whose properties and composition are homogeneous and which is physically distinct from other parts of the system. Many alloys, steel in particular, have a mixture of different phases present at the same time.

The study of phase transformations is concerned with how one or more phases in an alloy change into a new phase or mixture of phases. Since it deals with changes towards equilibrium, thermodynamics is a very powerful tool. However, the rate at which equilibrium is reached cannot be determined by thermodynamics alone. The time dependence has to be taken into account through the kinetics of the process (Porter and Easterling, 1992).

An important technological process is transformation hardening by quenching. It may be applied to steel to improve wear resistance, fatigue strength and often corrosion resistance. The phases with their specific microstructural characteristics are a design variable which within certain restrictions may be varied to obtain favourable properties. By applying various heat treatments in a way that insufficient time is available to form the equilibrium phase(s), the steel transforms to martensite. For specific applications a mixture of martensite with other (stable or metastable) phases such as pearlite, ferrite , bainite or austenite may be required. Examples are maraging steels, TRIP steels and dual phase steels.

Phase transformations require a specific thermal treatment to obtain the desired (micro)structure. In surface hardening the heating and cooling is usually applied to the surface of the workpiece rather than homogeneously to the whole bulk. As a consequence the temperature distribution and the heating or cooling rate at any time during the process will be inhomogeneous. Due to the inhomogeneous temperature distributions inhomogeneous transformations will occur. The kinetics of the transformation varies locally. Moreover, each phase has a different specific volume. The combination of both inhomogeneous temperatures and inhomogeneous transformations causes complicated stress states. The eventual product may come out warped and distorted and will contain residual stresses.

Conventional surface hardening is done by heating the workpiece in an oven and keeping it at an elevated temperature for some time in order to obtain austenite. After thorough austenization it is rapidly cooled and the whole surface will be hardened. Hardening of steel workpieces hinges strongly on experience. lt is done in specialized shops by specialized workmen. Yet, prediction of the results in terms of hardness, hardening depth and shape stability is only done qualitatively. A proper hardness is often essential to the service life of a product. When the heat treatment results in excessive distortions additional machining

is required to obtain the specified dimensions. During manufacturing, knowledge of the dimensions and the residual stresses after thermal treatment may yield substantial savings in machining costs. Numerical simulations can yield a number of benefits in this respect. The thermal cycles can be optimized to obtain the desired hardening result at a minimum cost, without extensive tests on the actual hardware. Benefits are gained in manufacturing as well as during service.

1.1 Numerical simulations of hardening

The possibilities of numerical simulations for prediction of hardening results were first explored some 30 years ago. Early attempts to predict residual stresses due to transformations relied on modification of thermal expansion in the temperature range where a transformation was expected to happen. In this primitive way the density differences between phases were accounted for (e.g. Rammerstorfer *et al.* (1981)). Hildenwall and Ericson (1977) and Inoue and Raniecki (1978) were the first to include explicit phase transformation kinetics in their models. Although more complicated, this had the advantage that it actually allowed to carry out realistic calculations of phase distributions in the workpiece.

Further research lead to refinements, notably inclusion of influence of stress state on transformation kinetics (Denis *et al.*, 1985) and of transformation plasticity (Leblond and Devaux, 1984; Abbasi and Fletcher, 1985; Sjöström, 1985; Denis and Simon, 1986). The numerical methods developed have also been applied to other technological processes such as cladding and welding (Ronda and Oliver, 2000; Lindgren, 2001).

1.2 Laser hardening

When only a few selected parts of the surface are to be hardened, laser hardening is an ideal technique (Stähli, 1979; Steen and Courtney, 1979; Chatterjee-Fischer *et al.*, 1984). With the help of a laser beam which scans the surface of the workpiece, locally very high temperatures can be obtained. Since this heating is very local, there are very high temperature gradients so that after the laser beam has passed cooling occurs very quickly. The temperature rates during heating as well as cooling are of the order of 1000 - 10000 K/s. The cooling rate is high enough to guarantee formation of martensite from all austenite formed during heating.

Due to the short interaction times, the time available for austenization is very short. In order for the material to sufficiently austenitize, the process parameters (power density and interaction time) have to be chosen such that the maximum temperature approaches the melting temperature. The importance of sufficiently high temperatures has already been recognized by Stähli (1979) and is very clearly explained in Ashby and Easterling (1984).

1.2.1 numerical simulation of laser hardening

The procedures developed for simulation of transformation hardening have also been applied to laser hardening (Farias *et al.*, 1990; Huétink *et al.*, 1990a; Ohmura *et al.*, 1991). The model of phase transformation kinetics had to be adapted to account for specific phenomena connected to rapid thermal cycles, such as incomplete austenization and grain growth at high temperatures.

The results of these studies can be directly applied to welding. The base material next to the weld goes through a thermal cycle which strongly resembles a laser hardening cycle. During multi-pass welding also reheating of previously laid down material occurs so that the same material is thermally cycled several times. To capture the behavior of the material in just a few state variables still remains a challenge (Lindgren, 2001).

1.2.2 steady state laser hardening

When a window is defined fixed to the laser beam and the material is made to pass through the window, hardening with a scanning laser can be viewed as a steady state process. In solid mechanics the regular way to numerically simulate a steady process is to carry out a transient calculation and prolong it until a steady state has been reached. For laser hardening this means that the heat affected zone has to be paved with a very dense element mesh in order to be able to capture the highly localized behaviour in sufficient detail.

Considerable savings in computation times can be gained when it is possible to exploit the specific properties of a steady process in a numerical model and directly evaluate the steady state. A number of methods which directly calculate steady states, applied to thermal processing, have been published (Bergheau *et al.*, 1991; Gu and Goldak, 1994; Hacquin *et al.*, 1996; Ruan, 1999; Balagangadhar *et al.*, 1999; Shanghvi and Michaleris, 2002)

The main points of interest when performing simulations are the thickness of the hardened layer, the residual stresses and the final distortion of the workpiece. Since calculation of residual stresses is desired, an elastic-plastic material model must be used. The inclusion of elasticity causes stability problems in steady state simulations (Thompson and Yu, 1990).

1.3 About this thesis

The objective of this work is to present methods which can be used for numerical simulations of phase transformations at the workpiece level. The emphasis is on description of macroscopic phenomena, rather than on what exactly happens within the crystals. The fraction of each phase present is treated as a state variable. The variation of this phase fraction is subject to kinetic equations, so that different thermal histories may yield different phase fraction distributions. Eventually phase distribution, residual stresses and distortions are to be predicted.

This thesis consists of two parts. The first part is concerned with simulations of phase transformations. In Chapter 2 the models of phase transformation are described as well as phenomena which are connected to the coupling between phase transformations and a stress field. A new method has been developed for determining the kinetic parameters for phase transformation simulations. This is described in Appendix B.

How the models of Chapter 2 are cast into constitutive relations is shown in Chapter 3 where rate equations for temperature and stress are derived. In Chapter 4 the rate equations are adapted for finite time steps and cast into a finite element model in Chapter 5. While the rate equations are still quite simple and standard, the extension to finite steps adds considerable complexity, which has not yet been reported in the literature. The assessment whether it is worthwhile to use these complex coupled equations instead of the simpler rate equations is part of this thesis and is addressed in Chapter 6.

The second part deals with the simulation of steady state laser hardening. Two methods will be presented here. The first method (Chapter 7) is based on the Arbitrary Lagrangian-Eulerian (ALE) method. This is essentially a transient simulation method on a largely Eulerian grid. The contribution to the ALE method as presented in this thesis is a major improvement in the modeling of the transient convective terms in the evolution of the state variables.

The second method is a truly steady state model (Chapter 8). It resembles a Total Lagrangian method, however, the steady nature of the problem is incorporated in the integration of the state variables. The use of a Discontinuous Galerkin method for the streamline integration as well as the streamline differentiation are original contributions.

2. Phase Transformation Models

This thesis mainly concerns finite element simulations of stresses and distortions due to transformation hardening. Inevitably this means that of all the different processes going on during phase transformations we only focused on those that influence the macroscopic behaviour of the workpiece. More than ten different kinds of microstructures have been identified to occur during the thermal processing of steel (Zhao and Notis, 1995). The phase which is usually desired as a result of transformation hardening is martensite. Of all the other phases which may exist at room temperature only ferrite, pearlite and austenite are considered. In this chapter the phenomenological models which are used to describe phase transformations in the finite element simulations are detailed. Incorporating other phase transformations is expected to be possible using these models with appropriate parameters.

In Section 2.2 the equations which describe the kinetics of diffusion controlled transformations are given. Here special attention is paid to the modeling of superheating and supercooling, which are important phenomena in a rapid process like laser hardening. In Section 2.4 the modifications to kinetics due to applied stresses are explained as well as transformation plasticity.

In Sections 2.5 and 2.6 two additional subjects which are not directly connected to phase transformations are treated. In Section 2.5 an estimate for the yield stress of a mixture of a soft phase with hard inclusions is given. This is relevant during the martensite transformation. In Section 2.6 a simple model for high temperature recovery is presented. This is added because during laser hardening locally temperatures are reached which are far higher than during regular case hardening.

In this work the unalloyed steel Ck45 was used because of the ample amount of data which is available on the behaviour of this steel. Where other steels show a different behaviour, transformation hardening of such steels may still be described by models similar to those presented here.

2.1 Introduction

From a macroscopic point of view we distinguish two types of transformations: diffusion controlled transformations and displacive lattice changes. For numerical simulations, the main difference is that the former require a certain time to take effect, whereas the latter may be viewed as an instantaneous change in the crystal lattice.
The proportion of the various phases in an alloy at a given temperature is described by the equilibrium phase diagram. The phase diagram of iron-carbon alloy is shown in Figure 2.1.

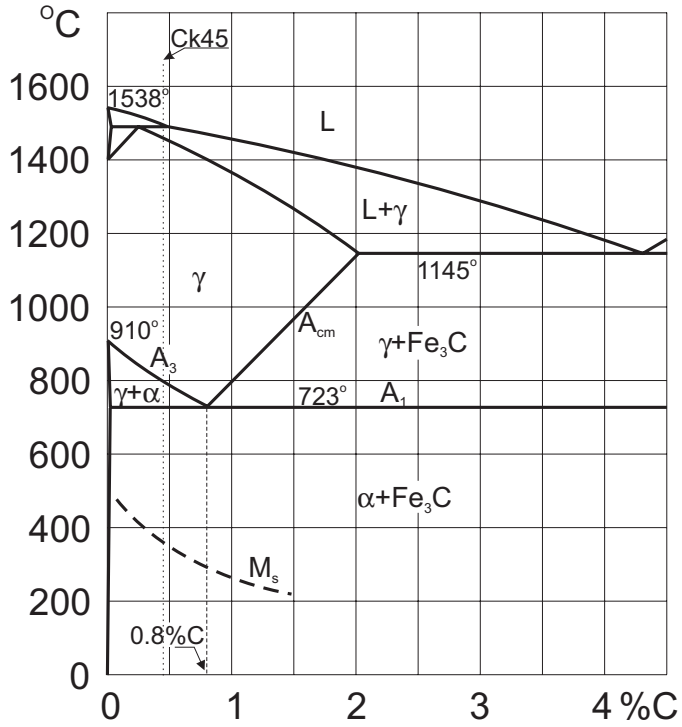

Figure 2.1: Iron-carbon phase diagram

Ck45 nominally contains 0.45 % carbon. When cooled from the liquid state (L) it solidifies as austenite (γ). After further cooling the A_3 temperature (T_{A3}) is reached. Below this temperature ferrite (α), a phase with practically no solubility of carbon, forms. Through diffusion the carbon is rejected into the remaining austenite. Below the A_1 temperature (T_{A1}) this austenite, which then contains approximately 0.8 % C, transforms eutectically into a mixture of ferrite and cementite (Fe_3C) called pearlite. Usually the cementite is dispersed in lamellae, giving the pearlite the mother-of-pearl appearance from which it derives its name. The austenite/pearlite reaction requires diffusion of carbon and takes time to materialize. When the cooling proceeds rapidly no or not all austenite transforms. The remaining austenite transforms to martensite (α') below the martensite-start (M_s) temperature.

2.2 Diffusion controlled transformations

As can be seen in Figure 2.1 the solubility of carbon in the parent phase differs with temperature. Excess alloying element quantity must be removed from the matrix and will aggregate as a different phase either in a solution or as a compound with other alloying elements.

The transformation proceeds via nucleation and subsequent growth. The kinetics shows two phases. Initially the new phase nucleates at preferred lattice sites and each nucleus starts

to grow steadily into a new grain. In time the available nucleation sites become exhausted and the growing grains will start impinging upon one another. Different mathematical models have been proposed to describe the transformation kinetics. Usually the growth of any phase is initially assumed to obey $\varphi(t) = kt^n$. Throughout this thesis φ stands for the volume fraction of the considered phase. The Avrami exponent n depends on the ratio between nucleation rates and growth rates. With progressing transformation the available nucleation volume becomes exhausted. It is related to the amount of parent phase left $(1 - \varphi)$. Also, retardation due to impingement is described by this term. This leads to a general rate equation:

$$\dot{\varphi} = (1 - \varphi)^r \, knt^{n-1} \tag{2.1}$$

Choosing $r = 1$ we obtain the Avrami equation, $r = 2$ leads to the Austin-Rickett equation (Austin and Rickett, 1939), see also Appendix B. The relative merits of different models have been investigated by Starink (1997). The overall differences appear small. In this work the Avrami equation was chosen.

2.2.1 kinetics, Avrami equation

When (2.1) is appropriately integrated the Johnson-Mehl-Avrami-Kolmogorov expression for diffusional phase changes (Avrami, 1939, 1940, 1941) is obtained. Leblond and Devaux (1984) corrected it to account for transformations which do not saturate to the full 100 % (Figure 2.2):

$$\varphi(t) = \varphi_0 + (\bar{\varphi} - \varphi_0) \left(1 - \mathrm{e}^{-(t/\tau)^n}\right) \tag{2.2}$$

Here $\bar{\varphi}(T)$ is the equilibrium phase content, φ_0 is the initial phase content. The coefficients n and $\tau(T)$ depend on the nucleation frequency and on the growth rate. Instead of the factor k in Equation (2.1), which has the awkward dimension $time^{-n}$ we prefer to use a reaction time constant τ. Both $\bar{\varphi}$ and τ are functions of the temperature T. The exponent n is constant when the nucleation rate and the growth rate have identical temperature dependence.

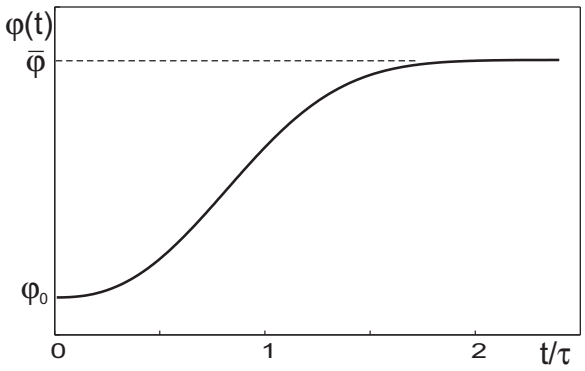

Figure 2.2: Avrami S-curve

Equation (2.2) has been derived for isothermal phase change. To describe non-isothermal processes, we cannot rely on a function $\varphi(t, T)$. Rather, a form has to be used which relates

the rate of phase change to the instantaneous state. Assuming that the additivity principle holds (Cahn, 1956; Leblond and Devaux, 1984) a rate equation may be used of the form:

$$\dot{\varphi} = \dot{\varphi}(\varphi, T) \tag{2.3}$$

After solution of the time from (2.2) and substitution into (2.1) the following rate equation is derived:

$$\dot{\varphi} = (\bar{\varphi} - \varphi)\,\frac{n}{\tau}\left(\ln\frac{\bar{\varphi} - \varphi_0}{\bar{\varphi} - \varphi}\right)^{(n-1)/n} \tag{2.4}$$

The time constant τ can be obtained from TTT diagrams (Figure 2.3) or estimated from CCT diagrams (Figure 2.4) as outlined in Appendix B.

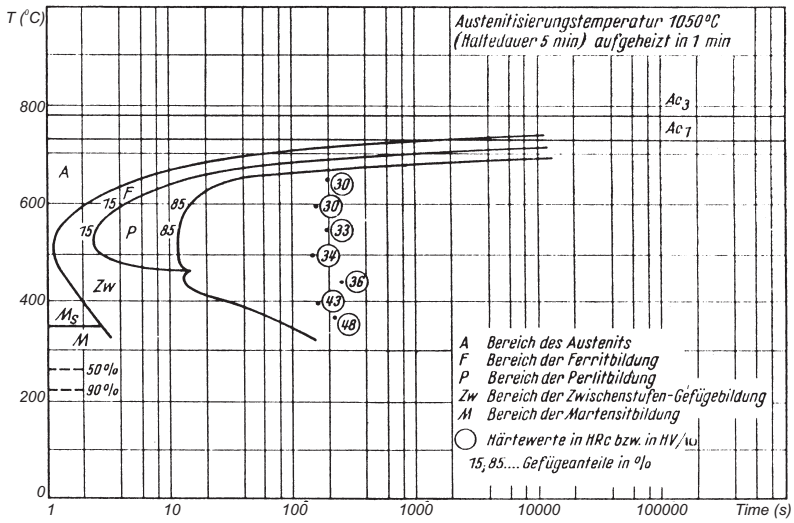

Figure 2.3: Time Temperature Transformation (TTT) diagram of steel Ck45 (Wever and Rose, 1961)

2.2.2 austenite-pearlite transformation

In steel the main diffusion related transformation is the pearlite transformation. In the austenitic phase (γ) the solubility of carbon in iron is very good. Upon cooling below T_{A3} the stability of the austenite drastically changes. Now the material consists of a mixture of two phases, low carbon ferrite (α) on the one hand and high carbon austenite on the other hand. The carbon content of the latter is given by the A_3-line in Figure 2.1.

At temperatures below 727°C (T_{A1}) the carbon within the remaining austenite will form a reaction with the iron Fe_3C, so called cementite. This is a very hard but also brittle phase. The cementite is dispersed in the ferrite matrix in globes or lamellae. The ferrite with dispersed cementite lamellae is called pearlite. Pearlite contains approximately 0.8 % carbon. The amount of pearlite can be determined from the lever rule. In steel Ck45,

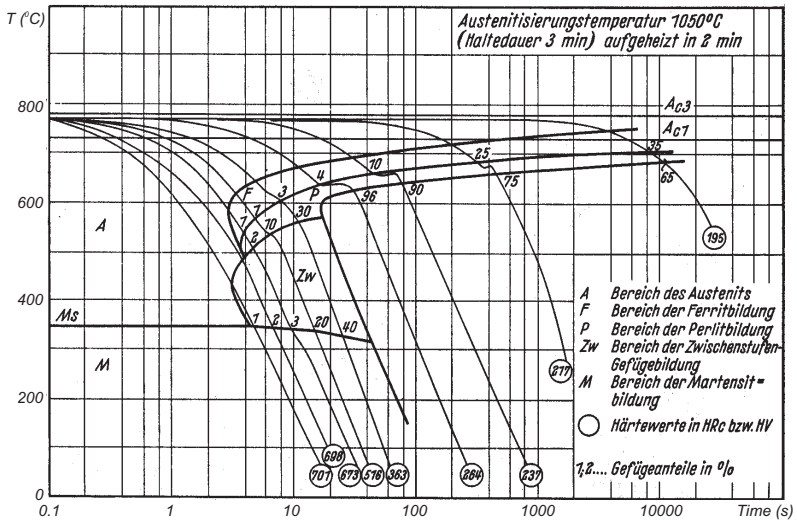

Figure 2.4: Continuous Cooling Transformation (CCT) diagram of steel Ck45 (Wever and Rose, 1961)

which nominally contains 0.45 % C, at room temperature the equilibrium volume fraction of pearlite $\bar{\varphi}_0^{\mathrm{p}} = 0.45/0.8 = 56\%$. The remainder is ferrite.

One of our goals is the prediction of phase fraction distributions after laser hardening. Laser hardening is characterized by a high power input and a short interaction time. Events happen very fast and equilibrium states are usually not obtained.

In large regions of the heat affected zone austenization will occur, but for subsequent homogenization not enough time is available. Locally low carbon austenite is still present when cooling has already started. No carbon diffusion is required for it to transform back to ferrite (Ashby and Easterling, 1984; Farias *et al.*, 1990; Ohmura *et al.*, 1991). Transformation starts instantaneously when the temperature drops below 910°C.

It is necessary to distinguish between low carbon austenite and homogenized austenite. As long as the homogenization is not complete, the low carbon austenite fraction is conveniently treated as superheated ferrite, ferrite still present at temperatures at which, according to the equilibrium diagram, it no longer should exist. To this ferrite fraction the additivity principle is applied by strictly applying $\dot{\varphi}^{\alpha} = \dot{\varphi}^{\alpha}(\varphi^{\alpha}, T)$. During cooling the ferrite transformation then starts in the steeper part of the Avrami S-curve. Transformation from austenite to ferrite is then possible even at high cooling rates.

To capture the delay in the transformations during heating as well as during cooling a model was devised based on a carbon balance. This model ensures that during heating the pearlite dissolves before homogenization of the austenite can occur. During cooling, ferrite has to be formed first, before pearlite can form.

heating

Above T_{A1} the phase diagram indicates an equilibrium fraction for pearlite of $\bar{\varphi}^{p} = 0$. The pearlite colonies transform to austenite with a high carbon content. The isothermal rate of change of the pearlite fraction is described by the Avrami equation (2.4):

$$\dot{\varphi}^{p} = -\varphi^{p} \frac{n^{p}}{\tau^{p}} \left(\ln \frac{\bar{\varphi}_0^{p}}{\varphi^{p}} \right)^{(n^{p}-1)/n^{p}} \tag{2.5}$$

The small spacing of the cementite lamellae suggests that the pearlite transformation will be very rapid. Experiments (Figure 2.6), however, show considerable superheating. This can be explained by the cementite lamellae dissolving from their ends rather than by lateral carbon diffusion (Ashby and Easterling, 1984), see figure 2.5.

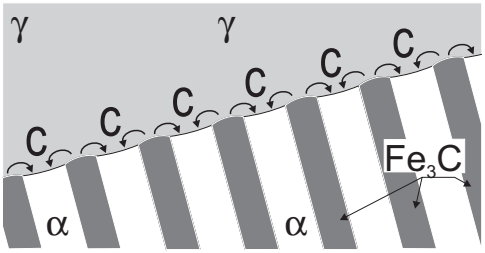

Figure 2.5: Dissolution of pearlite by carbon diffusion from ends of lamellae after Ashby and Easterling (1984).

The equilibrium fractions ferrite ($\bar{\varphi}^{\alpha}$) and austenite ($\bar{\varphi}^{\gamma}$) are determined from the phase diagram. At temperatures above T_{A1}, $\bar{\varphi}^{\gamma} = c/c_{A3}$ and $\bar{\varphi}^{\alpha} = 1 - \bar{\varphi}^{\gamma}$. Here c is the carbon content of the steel and c_{A3} is the content according to the A_3-line.

However, until all the pearlite has been transformed into austenite, there is not sufficient carbon available to transform the ferrite into austenite of the required carbon content. The rate equation for the $\alpha - \gamma$ transformation is therefore modified. While pearlite is still present the equilibrium fractions austenite and ferrite are corrected for the carbon deficiency:

$$\begin{aligned} \bar{\varphi}_{s}^{\gamma} &= \bar{\varphi}^{\gamma} \left(1 - \frac{\varphi^{p}}{\bar{\varphi}_0^{p}} \right) \\ \bar{\varphi}_{s}^{\alpha} &= \bar{\varphi}^{\alpha} + (\varphi_0^{\alpha} - \bar{\varphi}^{\alpha}) \frac{\varphi^{p}}{\varphi_0^{p}} \end{aligned} \tag{2.6}$$

The index s indicates superheating. The difference between volume and mass fractions is neglected. Substitution into (2.4) yields:

$$\begin{aligned} \dot{\varphi}^{\alpha} &= \left(\bar{\varphi}_{s}^{\alpha} - \varphi^{\alpha} \right) \frac{n^{\alpha}}{\tau^{\alpha}} \left(\ln \frac{\bar{\varphi}_{s}^{\alpha} - \varphi_0^{\alpha}}{\bar{\varphi}_{s}^{\alpha} - \varphi^{\alpha}} \right)^{(n^{\alpha}-1)/n^{\alpha}} \\ \text{and } \dot{\varphi}^{\gamma} &= -\dot{\varphi}^{\alpha} - \dot{\varphi}^{p} \end{aligned} \tag{2.7}$$

Upon reaching a temperature of approximately 910°C, the remaining ferrite transforms to austenite with a low carbon content. By diffusion the carbon concentration will level out and the austenite is homogenized (Ashby and Easterling, 1984). This is shown quantitatively in a TTA diagram (Figure 2.6).

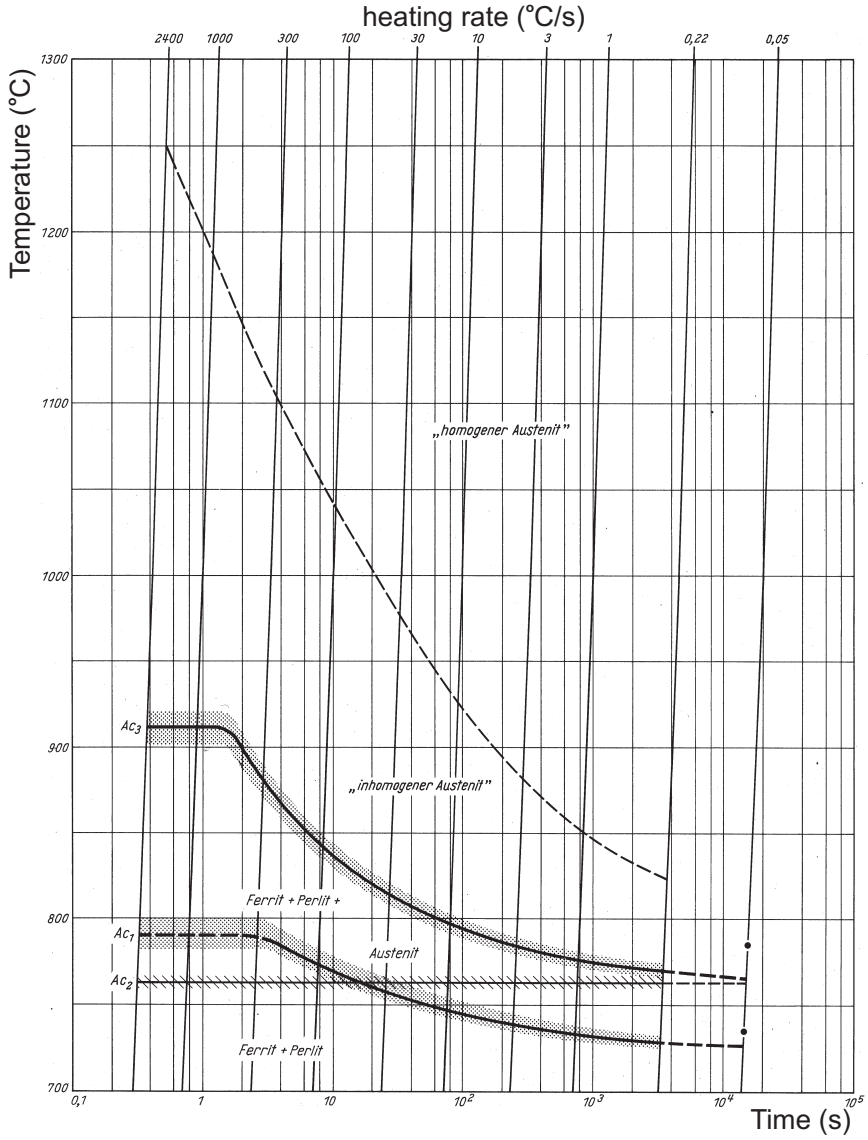

Figure 2.6: Time-Temperature-Austenization (TTA) diagram of steel Ck45 (Orlich *et al.*, 1973).

cooling

During cooling of fully homogenized austenite a first transformation occurs when the temperature drops below T_{A3}. Ferrite forms after local diffusion of carbon from the matrix. This ferrite is usually labeled pro-eutectoid or primary ferrite (Krielaart, 1995). The equilibrium fraction is again determined from the phase diagram using the lever rule:

$$\bar{\varphi}^{\alpha} = 1 - \frac{c}{c_{A3}} \tag{2.8}$$

This transformation is modeled by the Avrami equation (2.4):

$$\dot{\varphi}^{\alpha} = \left(\bar{\varphi}^{\alpha} - \varphi^{\alpha}\right) \frac{n^{\alpha}}{\tau^{\alpha}} \left(\ln \frac{\bar{\varphi}^{\alpha}}{\bar{\varphi}^{\alpha} - \varphi^{\alpha}} \right)^{(n^{\alpha}-1)/n^{\alpha}} \tag{2.9}$$

Below T_{A1} the remaining austenite transforms to pearlite. The ferrite reaction usually does not keep pace with the equilibrium as dictated by the temperature. The carbon content of the austenite remaining at T_{A1} is not yet according to that of the eutectic mixture. The pearlitic reaction is slowed down by the deficiency of the carbon. Therefore the equilibrium content of the pearlite must be corrected for carbon deficiency:

$$\begin{aligned} \bar{\varphi}_{u}^{p} &= \bar{\varphi}_{0}^{p} \frac{\varphi^{\alpha}}{\bar{\varphi}_{0}^{\alpha}} \\ \dot{\varphi}^{p} &= \left(\bar{\varphi}_{u}^{p} - \varphi^{p}\right) \frac{n^{p}}{\tau^{p}} \left(\ln \frac{\bar{\varphi}_{u}^{p}}{\bar{\varphi}_{u}^{p} - \varphi^{p}} \right)^{(n^{p}-1)/n^{p}} \end{aligned} \tag{2.10}$$

The index u indicates undercooling.

2.3 Martensite transformations

An expression for the amount of martensite which fits experiments very well is based on the assumption that, as soon as the temperature drops below the M_s temperature, there exists a linear relation between martensite growth and temperature decrease $\dot{\varphi}^{m} = -\beta \dot{T}$. This relation has to be corrected for the vanishing parent phase so that we end up with $\dot{\varphi}^{m} = -(\varphi_{Ms}^{\gamma} - \varphi^{m})\beta \dot{T}$. Integration from T_{Ms} yields the Koistinen and Marburger (1959) equation:

$$\varphi^{m}(T) = \varphi_{Ms}^{\gamma} \left(1 - e^{\beta(T - T_{Ms})}\right) \qquad \text{for } T < T_{Ms} \tag{2.11}$$

where φ_{Ms}^{γ} is the amount of austenite still present at T_{Ms}. The martensite-start temperature depends to some extent on the austenization conditions (Farias *et al.*, 1990). This is caused by grain growth at elevated temperatures, which limits the amount of potential nucleation sites.

According to Zhao and Notis (1995) there is evidence that the martensite transformation is also governed by (very fast) isothermal kinetics. Here, however, the general concept is followed and martensite formation is treated as an athermal reaction. Reverse transformation from martensite to austenite is assumed to be only possible at temperatures above M_s.

2.4 Stress-transformation interaction

A phase transformation is usually accompanied by a change of the specific volume of the material. Inhomogeneous temperature distributions and inhomogeneous transformations will cause high stresses and sometimes excessive distortions and cracking of the workpiece.

The presence of stresses during phase transformations has two major effects, (i) it modifies the kinetics of the transformation and (ii) it causes an irreversible strain even in the presence of a small stress, termed transformation induced plasticity. An extensive bibliography as well as additional experimental work on both aspects are given by Aeby-Gautier (1985) and Denis *et al.* (1985)

2.4.1 modifications to the kinetics

The modification of the transformation kinetics has been a subject of many studies. The classics in the field are the papers by Patel and Cohen (1953) on the effect of stress on martensitic transformation and of Bhattacharyya and Kehl (1955) on bainite transformation. An extensive literature review is given by Aeby-Gautier (1985) of which the highlights are resumed by Simon *et al.* (1994). The martensite transformation in particular (Videau *et al.*, 1996; Liu *et al.*, 2000b) but also the austenite-pearlite reaction (Veaux *et al.*, 2001; Liu *et al.*, 2000a) have received attention in recent years.
The stress state $\boldsymbol{\sigma}$ can be decomposed into a deviatoric stress $\mathbf{s}$ and a hydrostatic pressure p:

$$\begin{aligned} \boldsymbol{\sigma} &= \mathbf{s} - p\mathbf{1} \\ p &= -\frac{1}{3}\operatorname{tr}(\boldsymbol{\sigma}) = -\frac{1}{3}\boldsymbol{\sigma} : \mathbf{1} \end{aligned} \tag{2.12}$$

Here $\mathbf{1}$ is the second order unit tensor. A norm for the deviatoric stress is the equivalent stress or Von Mises stress σ_{eq}:

$$\sigma_{\text{eq}} = \sqrt{\frac{3}{2}\mathbf{s} : \mathbf{s}} \tag{2.13}$$

In general the effect of the stress on the kinetics is divided into separate effects due to hydrostatic pressure and stress deviator. By carrying out torsion tests as well as tension and compression tests during transformation these two effects can be separated (Videau *et al.*, 1996).

hydrostatic pressure

The influence of hydrostatic pressure on both the austenite/pearlite and the martensite transformation is qualitatively the same. A positive pressure impairs the transformation. This appears as an overall lowering of the characteristic lines in the equilibrium phase diagram. T_{A1} as well as T_{Ms} is lowered. For the pearlitic reaction this means that it evolves at lower temperatures and therefore the overall kinetics is slower. For the martensite transformation cooling to lower temperatures is needed to obtain comparable amounts of martensite.

deviatoric stress

Under the action of deviatoric stresses similar effects are found for both the pearlite transformation and the martensitic transformation. Both transformations are enhanced by a deviatoric stress. In the case of martensite transformations an increase of T_{Ms} is seen (Patel and Cohen, 1953; Videau *et al.*, 1996).
Pearlitic reaction times are considerably shortened (Bhattacharyya and Kehl, 1955; Aeby-Gautier, 1985; Simon *et al.*, 1994; Veaux *et al.*, 2001).

kinetic model

The influence of the stresses on the kinetics as described above is partly incorporated in the kinetic models used in this work. The stress influence on the kinetics of the pearlite transformation during cooling is present as a stress dependent time constant τ in the Avrami equation (2.4):

$$\tau(T, \sigma_{\mathrm{eq}}, p) = f(\sigma_{\mathrm{eq}}, p)\tau(T) = \tau(T)\exp(-A_\tau \sigma_{\mathrm{eq}} + B_\tau p) \tag{2.14}$$

The decrease in T_{A1} due to hydrostatic pressure is not implemented.

For the martensite transformation a correction is applied to the $\mathrm{M_s}$ temperature in the Koistinen-Marburger equation (2.11):

$$T_{\mathrm{Ms}}(\sigma_{\mathrm{eq}}, p) = T_{\mathrm{Ms0}} + A_{\mathrm{M}}\sigma_{\mathrm{eq}} - B_{\mathrm{M}} p \tag{2.15}$$

Here T_{Ms0} is the $\mathrm{M_s}$ temperature under stress-free conditions.

2.4.2 transformation induced plasticity

When a stress is applied, while a phase transformation occurs, a permanent strain results. This also applies for stress levels way below the yield stress of the weakest phase (de Jong and Rathenau, 1961; Greenwood and Johnson, 1965).

The first attempts to model this effect in numerical simulations employed an artificial lowering of the overall yield stress in the transformation temperature range (Rammerstorfer *et al.*, 1981; Abbasi and Fletcher, 1985). More refined models, in which the increase in transformation plasticity is linked to the progress of the transformation, were implemented by Denis *et al.* (1985) and Sjöström (1985). Reviews of the literature are found in Aeby-Gautier (1985) and Fischer *et al.* (1996).

Two mechanisms are held responsible for transformation plasticity, the Greenwood-Johnson mechanism and the Magee mechanism. The classical analysis by Greenwood and Johnson (1965) considers a phase with a volume mismatch growing in the original soft phase. The superposition of the global stress field on the local field due to the mismatch facilitates plastic flow of the soft parent phase. Only the total strain at the end of the transformation is given:

$$\varepsilon^{tp} = \frac{5}{6}\frac{\delta v}{v}\frac{\sigma}{\sigma_{\mathrm{y}}} \tag{2.16}$$

Here $\delta v/v$ is the volume strain during transformation; σ_{y} is the yield stress of the soft parent phase. This expression fits very well to experiments for relative applied stress levels

$\sigma/\sigma_y < 0.5$. Zwigl and Dunand (1997) extended the theory to include the non-linear behaviour for $0.5 < \sigma/\sigma_y < 1$.

For a three-dimensional stress state Equation (2.16) can be generalized to:

$$\boldsymbol{\varepsilon}^{tp} = \frac{3}{2} K \frac{\mathbf{s}}{\sigma_y}; \text{ with } K = \frac{5}{6} \frac{\delta v}{v} \tag{2.17}$$

Several micromechanical (Leblond *et al.*, 1989; Ganghoffer *et al.*, 1997) as well as experimental (Aeby-Gautier, 1985; Videau *et al.*, 1996) studies have been published to quantify the transformation plasticity with progressing transformation. The results are summarized in a general rate formula:

$$\mathbf{d}^{tp} = \frac{3}{2} K F'(\varphi) \frac{\mathbf{s}}{\sigma_y} \dot{\varphi} \qquad \text{where} \quad F' = \frac{\mathrm{d}F}{\mathrm{d}\varphi}; \; F(0) = 0 \text{ and } F(1) = 1 \tag{2.18}$$

Here φ is the fraction of the growing phase. A list with different expressions for $F'(\varphi)$ is summarized by Fischer *et al.* (1996). A practical and easily understood relation which reflects the saturation of transformation plasticity due to the vanishing of the soft parent phase is:

$$F'(\varphi) = 2(1 - \varphi) \tag{2.19}$$

This expression for $F(\varphi)$ is adopted in this work.

The Magee mechanism explains transformation plasticity as the result of a preferential crystal orientation of the product phase due to the applied stress. Especially the martensitic transformation involves a considerable lattice shear, which can occur along different potential habit planes (Patel and Cohen, 1953; Schumann, 1979). Due to the stress certain directions along certain planes are favoured, which causes an overall strain. The lattice shear can exhibit different complications such as twinning, which makes derivation of analytical models difficult. Micromechanical finite element models have been reported by Ganghoffer *et al.* (1991) and Fischer *et al.* (2000). For macromechanical modeling also Equation (2.18), with appropriate values of K is usually applied.

2.5 Composite constitutive relations

It is customary to calculate the yield stress of the mixture of the different phases by a linear mixture rule (Inoue and Raniecki, 1978; Sjöström, 1985; Denis *et al.*, 1987; Ronda and Oliver, 2000). This is accurate enough when all coexisting phases are of comparable hardness. Unfortunately the transformation which mainly dominates the final stress distribution, i.e. the austenite to martensite transformation, involves the two extremes in phase hardnesses. The martensite yield stress is typically an order of magnitude higher than that of austenite so that a linear mixture rule is not appropriate. It is clear that the linear mixture rule, which postulates identical strain in all involved phases constitutes an upper bound for the compound yield stress. In reality the plastic strain will tend to concentrate in the softer phases, making the overall response softer than according to linear mixing. This was investigated for viscoplastic behaviour by Stringfellow and Parks (1991). Their final model is rather complicated and the dependence on the phase fraction is presented in an implicit way.

Leblond *et al.* (1986) postulated that as long as the phase fraction of the hard phase is small the average deviatoric stress in all phases is equal. This they back up by finite element simulations. They arrive at a modification of the linear mixture rule which requires interpolation between data points of their finite element results which is not very practical.

In Appendix C an estimate is given based on a set of simple assumptions on the deformations of a soft matrix with periodically distributed small hard inclusions. An approximation for the compound yield stress is given as:

$$\begin{aligned} \sigma_{\mathrm{y}} &= \varphi^{\alpha}\sigma_{\mathrm{y}}^{\alpha} + \varphi^{\mathrm{p}}\sigma_{\mathrm{y}}^{\mathrm{p}} + \varphi^{\gamma}\sigma_{\mathrm{y}}^{\gamma} + f(\varphi^{\mathrm{m}})\sigma_{\mathrm{y}}^{\mathrm{m}} \\ \text{with: } f(\varphi^{\mathrm{m}}) &= \varphi^{\mathrm{m}}(C + 2(1-C)\varphi^{\mathrm{m}} - (1-C)(\varphi^{\mathrm{m}})^2) \\ \text{where: } C &= 1.383\frac{\sigma_{\mathrm{y}}^{\gamma}}{\sigma_{\mathrm{y}}^{\mathrm{m}}} \end{aligned} \tag{2.20}$$

The results using this equation are almost identical to the finite element results reported by Leblond *et al.* (1986). This equation should only be used when the differences in hardness between martensite and austenite are large. It has been derived by assuming all strain concentrated in the softer phase. It is clear that application to a mixture of two phases with equal yield stress will give incorrect results.

2.6 Plastic strain and recovery

A permanent strain of a crystal requires sliding or slip of the atoms along one or more habit planes of maximum resolved shear stress. The work required to overcome the energy barrier in the crystal is less when the atoms hop one after the other, rather than in concert. This causes structural defects which are called dislocations and which move upon prolonged straining.

For one crystal to strain, a number of slip systems has to be active. In a polycrystalline metal these slip systems are generally not compatible among neighbouring grains. Extra slip is required to enforce boundary compatibility. The movement of the dislocations is impaired by imperfections of the crystal structure, such as precipitates, grain boundaries and also other dislocations. During plastic flow, the dislocation density increases and the dislocation mobility decreases as straining progresses. This is apparent from the increase of the resistance against straining as a function of the applied strain, work hardening. To capture this effect in this thesis a parameter is used which accounts for the dislocation density due to cumulative plastic straining, the equivalent plastic strain ε^{p}.

At elevated temperatures, the work hardening effect diminishes. Following application of a fixed strain rate, plastic flow commences at the initial (temperature dependent) yield stress, but with further straining the stress soon reaches a steady state value. This indicates that apart from dislocation movements, other dynamic effects also play a role. Due to thermally activated atomic movements in the lattice, dislocations are continuously being formed, reordered and annihilated. This effect depends exponentially on temperature ($\sim \exp(RT/Q)$, where Q is an activation energy) and is called recovery. At high temperatures apart from recovery also recrystallization and grain growth will occur.

A laser hardening cycle evolves extremely fast, leaving little time for dynamic effects. This is offset by the high temperatures, which are reached in large parts of the heat affected

zone. Recovery and recrystallization are important in the sense that when they occur, the plastic history which is generated during the initial heating phase of the process, is annihilated and plays no role during subsequent cooling (Hong *et al.*, 1998). It is modeled as static recovery (Estrin, 1998) by adding a relaxation type term $-c_{\mathrm{rc}}\varepsilon^{\mathrm{p}}$ to the evolution of the equivalent plastic strain.

2.7 Summary

In this section a number of topics from materials science which are relevant for transformation hardening simulations have been dealt with and have been cast into models suitable for use in simulations. Most of these models are more or less standard for this type of simulation. However, the laser hardening process involves a number of extra complications.
The model for the superheating of pearlite and ferrite deviates from the often advocated notion that reaching the temperature A_3 is a sufficient condition for the formation of austenite. Rapid heating may cause incomplete austenization even above $T_{\mathrm{A}3}$ and this influences the reverse transformation during cooling.
The stress dependence of the martensite transformation is important for prediction of the amount of retained austenite. Retained austenite is a problem in the laser processing of specific materials.
Since laser hardening involves a thermal cycle from room temperature to almost melting temperature and back to room temperature it is important to include a recovery model. In this way the plastic deformation generated during the initial stages of the process is annihilated in locations where sufficiently high temperatures are reached.
Finally, the simple model for the composite yield stress of an austenite-martensite mixture is more realistic than the popular linear mixing model.

Two phenomena have been treated in the literature but were not included here. At high temperatures the average size of the austenite grains will increase. Small grains are annexed by their bigger neighbours. The average grain size affects the transformation kinetics during cooling. The second aspect is the bainite transformation. Bainite is a very fine phase which has a hardness which is in between that of martensite and pearlite. In this thesis no distinction is made between ferrite/pearlite and bainite. The emphasis is on properly predicting the martensite fraction. When necessary, bainite transformation may be included using similar kinetic equations as used for ferrite and pearlite.

3. Thermo-Mechanical Analysis with Phase Transformations

In this chapter the equations which describe the interactions between stress, temperature and phase change are derived.

First, the phase transformation is considered as an autonomous process influenced neither by the stress state nor by the temperature. It is shown how phenomena like latent heat, transformation strain and transformation plasticity are described.
The resulting equations are all linearized rate equations. When these equations are integrated over finite time steps additional terms appear which will be elaborated in Chapter 4.

3.1 Thermal analysis

The heat flow in a solid is described by Fourier's law:

$$\mathbf{q} = -\kappa \nabla T \tag{3.1}$$

Here $\mathbf{q}$ is the heat flow, T is the temperature and κ is the thermal conductivity. The temperature evolution is governed by the equation for conservation of energy:

$$-\nabla \cdot \mathbf{q} + \boldsymbol{\sigma} : \mathbf{d} - \rho \dot{H} = 0 \tag{3.2}$$

where ρ is the mass density, H is the enthalpy, $\boldsymbol{\sigma}$ is the Cauchy stress and $\mathbf{d}$ is the deformation rate. For solids it can be shown that the enthalpy is the dominant term in the internal energy. The enthalpy is a summation of the enthalpies per phase:

$$H = \sum_i \varphi^i H^i \tag{3.3}$$

Here φ^i is the volume phase fraction of phase i. For each fraction the enthalpy is a function of the temperature, obtained by integration of the specific heat $c_{\mathrm{p}}^i(T)$ as obtained from DSC scans:

$$H^i(T) = \int_{T_0}^{T} c_{\mathrm{p}}^i(T)\, \mathrm{d}T + H_0^i \tag{3.4}$$

The rate of the enthalpy change is found from:

$$\dot{H} = \sum_i \varphi^i c_{\mathrm{p}}^i \dot{T} + \sum_i \dot{\varphi}^i H^i \tag{3.5}$$

The first term is the regular specific heat, the second term is the latent heat of phase transformation. The effect of mechanical dissipation has been shown by Leblond *et al.* (1985) to be at least one order of magnitude lower than that of the latent heat and three orders lower than the applied external heat. Therefore it has been neglected here. The resulting rate equation of thermal equilibrium is:

$$\rho c_{\mathrm{p}} \dot{T} = -\nabla \cdot \mathbf{q} - \rho \dot{H}_\varphi \tag{3.6}$$

where:

$$\rho c_{\mathrm{p}} = \sum_i \varphi^i \rho^i c_{\mathrm{p}}^i$$

$$\rho \dot{H}_\varphi = \sum_i \rho^i H^i \dot{\varphi}^i$$

3.2 Stress analysis

The equilibrium equation in the absence of inertia and body forces can be written as:

$$\boldsymbol{\sigma} \cdot \nabla = \mathbf{0} \tag{3.7}$$

Here $\boldsymbol{\sigma}$ is the Cauchy stress tensor. When deformation gradients remain small, the rate form of this equation is:

$$\dot{\boldsymbol{\sigma}} \cdot \nabla = \mathbf{0} \tag{3.8}$$

The stresses depend on the strains and the strains depend on the displacements. The theory in this section is based on small strains. For most hardening calculations this is sufficient:

$$\boldsymbol{\varepsilon} = \tfrac{1}{2}(\mathbf{u}\nabla + \nabla\mathbf{u}) \tag{3.9}$$

The strain rate depends on the velocities:

$$\mathbf{d} = \tfrac{1}{2}(\mathbf{v}\nabla + \nabla\mathbf{v}) \tag{3.10}$$

The total strain $\boldsymbol{\varepsilon}$ is assumed to consist of a number of independent contributions:

$$\boldsymbol{\varepsilon} = \boldsymbol{\varepsilon}^{\mathrm{el}} + \boldsymbol{\varepsilon}^{\mathrm{pl}} + \boldsymbol{\varepsilon}^{\mathrm{th}} + \boldsymbol{\varepsilon}^{\mathrm{tr}} + \boldsymbol{\varepsilon}^{\mathrm{tp}} \tag{3.11}$$

where *el* is the elastic part, *pl* is the plastic strain, *th* is the thermal dilatation, *tr* is the strain due to phase transformation and *tp* is due to transformation plasticity. The stress is assumed proportional to the elastic strain:

$$\boldsymbol{\sigma} = \mathbf{E} : \boldsymbol{\varepsilon}^{\mathrm{el}} \tag{3.12}$$

Here $\mathbf{E}$ is the fourth order elasticity tensor $\mathbf{E} = 2G(\mathbf{I} - (1/3)\mathbf{11}) + k_\mathrm{b}\mathbf{11}$, where G and k_b are the shear modulus and the bulk modulus. The elastic properties are assumed identical for all phases and to depend on the temperature only. For the stress rate we then find:

$$\begin{aligned}
\dot{\boldsymbol{\sigma}} &= \mathbf{E} : \mathbf{d}^{\mathrm{el}} + \dot{\mathbf{E}} : \boldsymbol{\varepsilon}^{\mathrm{el}} \\
\dot{\boldsymbol{\sigma}} &= \mathbf{E} : (\mathbf{d} - \mathbf{d}^{\mathrm{pl}} - \mathbf{d}^{\mathrm{tp}} - \mathbf{d}^{\mathrm{th}} - \mathbf{d}^{\mathrm{tr}}) + \dot{\mathbf{E}} : \mathbf{E}^{-1} : \boldsymbol{\sigma} \\
\dot{\boldsymbol{\sigma}} &= \mathbf{E} : (\mathbf{d} - \mathbf{d}^{\mathrm{pl}} - \mathbf{d}^{\mathrm{tp}} - \mathbf{d}^{\mathrm{th}} - \mathbf{d}^{\mathrm{tr}}) + \left(\frac{1}{G}\frac{\mathrm{d}G}{\mathrm{d}T}\mathbf{s} - \frac{1}{k_\mathrm{b}}\frac{\mathrm{d}k_\mathrm{b}}{\mathrm{d}T} p\mathbf{1} \right) \dot{T}
\end{aligned} \tag{3.13}$$

3.2.1 transformation and thermal strain

The mass density can be written as a weighted sum of the phase fraction densities

$$\rho = \sum_i \varphi^i \rho^i \tag{3.14}$$

The mass density of each fraction is a function of the temperature. The rate of change is written as:

$$\frac{\mathrm{d}\rho}{\mathrm{d}t} = \sum_i (\dot{\varphi}^i \rho^i + \varphi^i \frac{\mathrm{d}\rho^i}{\mathrm{d}T}\dot{T}) \tag{3.15}$$

The first term on the right hand side is the density change due to phase transformation, the second term, due to thermal expansion. For isotropic materials density change and strain are related by:

$$\mathrm{d}\varepsilon = -\frac{1}{3}\frac{\mathrm{d}\rho}{\rho} \tag{3.16}$$

The strain rates due to phase transformation and thermal expansion are:

$$\begin{aligned}
\mathbf{d}^{\mathrm{tr}} &= -\frac{1}{3}\sum_i \frac{\rho^i}{\rho}\dot{\varphi}^i \mathbf{1} \\
\mathbf{d}^{\mathrm{th}} &= -\frac{1}{3}\sum_i \frac{\varphi^i}{\rho}\frac{\mathrm{d}\rho^i}{\mathrm{d}T}\dot{T}\mathbf{1} = \alpha\dot{T}\mathbf{1}
\end{aligned} \tag{3.17}$$

Here α is the phase fraction dependent coefficient of thermal expansion.

3.2.2 transformation induced plasticity

The usual generalization of the results of one-dimensional tests as performed by de Jong and Rathenau (1961) and as described in section 2.4.2 to a multidimensional stress state is to express transformation plasticity proportional to the deviatoric stress:

$$\mathbf{d}^{\mathrm{tp}} = \frac{3}{2}\sum_i K^i F^{i\prime}\dot{\varphi}^i \frac{\mathbf{s}}{\sigma_\mathrm{y}} \tag{3.18}$$

The functions $F^i(\varphi^i)$ determine how the transformation plasticity varies during the course of the transformation. The constants K^i depend on the chemical composition of the steel and on the type of transformation. The values of K^i are either obtained experimentally or estimated using the formula derived by Greenwood and Johnson (1965).

3.2.3 constitutive equations

Here we focus on the description of plastic behaviour during phase transformation. The derivation of equations for elastic behaviour is straightforward and its result is implicitly included in the equations for plastic behaviour. The description of plastic deformation is based on the Von Mises yield criterion with isotropic hardening. Isotropic hardening is in general sufficient since at high temperatures recovery occurs and any plastic history disappears.

Plastic deformation occurs when the deviatoric stress exceeds the yield surface:

$$\Phi(\mathbf{s}, \varepsilon^{\mathrm{p}}, T, \varphi) = \mathbf{s} : \mathbf{s} - \frac{2}{3}(\sigma_{\mathrm{y}}(\varepsilon^{\mathrm{p}}, T, \varphi))^2 = 0 \tag{3.19}$$

Here the equivalent plastic strain ε^{p} is defined by:

$$\varepsilon^{\mathrm{p}} = \int_0^t \dot{\varepsilon}^{\mathrm{p}}\,\mathrm{d}t \qquad \text{where} \qquad \dot{\varepsilon}^{\mathrm{p}} = \sqrt{\tfrac{2}{3}\mathbf{d}^{\mathrm{pl}} : \mathbf{d}^{\mathrm{pl}}} - c_{\mathrm{rc}}\varepsilon^{\mathrm{p}} \tag{3.20}$$

The last term is added to account for high temperature recovery (Section 2.6). Using classical flow theory for plasticity, the plastic strain rate is given by:

$$\mathbf{d}^{\mathrm{pl}} = \frac{3}{2}\frac{\dot{\lambda}}{\sigma_{\mathrm{y}}}\mathbf{s} \tag{3.21}$$

Substituting this expression into (3.20) we find that:

$$\dot{\lambda} = \dot{\varepsilon}^{\mathrm{p}} + c_{\mathrm{rc}}\varepsilon^{\mathrm{p}} \tag{3.22}$$

Differentiating the yield criterion (3.19) with respect to time and substituting (3.13) for the stress rate and bearing in mind that $\mathbf{s} = \boldsymbol{\sigma} - \frac{1}{3}\,\mathrm{tr}(\boldsymbol{\sigma})\mathbf{1}$ and that $\mathbf{s} : \mathbf{1} = 0$ we obtain:

$$\mathbf{s} : \mathbf{E} : (\mathbf{d} - \mathbf{d}^{\mathrm{pl}} - \mathbf{d}^{\mathrm{tp}} - \mathbf{d}^{\mathrm{th}} - \mathbf{d}^{\mathrm{tr}}) + \frac{2}{3}\sigma_{\mathrm{y}}^2\left(\frac{1}{G}\frac{\mathrm{d}G}{\mathrm{d}T} - \frac{1}{\sigma_{\mathrm{y}}}\frac{\partial\sigma_{\mathrm{y}}}{\partial T}\right)\dot{T} - \frac{2}{3}\sigma_{\mathrm{y}}\frac{\partial\sigma_{\mathrm{y}}}{\partial\varepsilon^{\mathrm{p}}}\dot{\varepsilon}^{\mathrm{p}} - \frac{2}{3}\sigma_{\mathrm{y}}\sum_i \frac{\partial\sigma_{\mathrm{y}}}{\partial\varphi^i}\dot{\varphi}^i = 0 \tag{3.23}$$

Substitution of (3.17), (3.18), and (3.21) into Equation (3.23), while using $\mathbf{s} : \mathbf{E} = 2G\mathbf{s}$ and Equation (3.19) yields an expression for $\dot{\varepsilon}^{\mathrm{p}}$:

$$\dot{\varepsilon}^{\mathrm{p}} = \frac{1}{1 + h_\varepsilon}\left(\frac{1}{\sigma_{\mathrm{y}}}\mathbf{s} : \mathbf{d} + (\frac{\sigma_{\mathrm{y}}}{3G}\frac{1}{G}\frac{\mathrm{d}G}{\mathrm{d}T} - h_{\mathrm{T}})\dot{T} - \sum_i \left(K^i F^{i\prime} + h_\varphi^i\right)\dot{\varphi}^i - c_{\mathrm{rc}}\varepsilon^{\mathrm{p}}\right) \tag{3.24}$$

where the normalized hardening parameters $h_{(\cdot)}$ are defined as:

$$\begin{aligned} h_\varepsilon &= \frac{1}{3G}\frac{\partial\sigma_{\mathrm{y}}}{\partial\varepsilon^{\mathrm{p}}} \\ h_{\mathrm{T}} &= \frac{1}{3G}\frac{\partial\sigma_{\mathrm{y}}}{\partial T} \\ h_\varphi^i &= \frac{1}{3G}\frac{\partial\sigma_{\mathrm{y}}}{\partial\varphi^i} \end{aligned} \tag{3.25}$$

Substitution of this expression into (3.21) gives an expression for the plastic strain rate:

$$\mathbf{d}^{\mathrm{pl}} = \frac{1}{1+h_\varepsilon}\frac{3\mathbf{ss}}{2\sigma_{\mathrm{y}}^2} : \mathbf{d} + \frac{1}{1+h_\varepsilon}\frac{\mathbf{s}}{2G}\left(\frac{1}{G}\frac{\mathrm{d}G}{\mathrm{d}T} - \frac{3Gh_{\mathrm{T}}}{\sigma_{\mathrm{y}}}\right)\dot{T} - \frac{1}{1+h_\varepsilon}\frac{3\mathbf{s}}{2\sigma_{\mathrm{y}}}\sum_i \left(K^i F^{i\prime} + h_\varphi^i\right)\dot{\varphi}^i + \frac{h_\varepsilon}{1+h_\varepsilon}\frac{3\mathbf{s}}{2\sigma_{\mathrm{y}}}c_{\mathrm{rc}}\varepsilon^{\mathrm{p}} \quad (3.26)$$

This in turn is substituted into (3.13) to yield the desired expression for the stress rate:

$$\begin{aligned}\dot{\boldsymbol{\sigma}} = (\mathbf{E} - \frac{1}{1+h_\varepsilon}\frac{3G\mathbf{ss}}{\sigma_{\mathrm{y}}^2}) : \mathbf{d} \\ + \left(k_{\mathrm{b}}\sum_i \frac{\varphi^i}{\rho}\frac{\mathrm{d}\rho^i}{\mathrm{d}T}\mathbf{1} - \frac{1}{k_{\mathrm{b}}}\frac{\mathrm{d}k_{\mathrm{b}}}{\mathrm{d}T}p\mathbf{1} + \frac{1}{1+h_\varepsilon}\left(\frac{h_\varepsilon}{G}\frac{\mathrm{d}G}{\mathrm{d}T} + \frac{3Gh_{\mathrm{T}}}{\sigma_{\mathrm{y}}}\right)\mathbf{s}\right)\dot{T} \\ + k_{\mathrm{b}}\sum_i \frac{\rho^i}{\rho}\dot{\varphi}^i\mathbf{1} + \frac{1}{1+h_\varepsilon}\sum_i \left(h_\varphi^i - h_\varepsilon K^i F^{i\prime}\right)\frac{3G\mathbf{s}}{\sigma_{\mathrm{y}}}\dot{\varphi}^i \\ - \frac{h_\varepsilon}{1+h_\varepsilon}\frac{3G\mathbf{s}}{\sigma_{\mathrm{y}}}c_{\mathrm{rc}}\varepsilon^{\mathrm{p}} \quad (3.27)\end{aligned}$$

Or in shorthand:

$$\dot{\boldsymbol{\sigma}} = \mathbf{D}_\varepsilon : \mathbf{d} + \mathbf{c}_{\mathrm{T}}\dot{T} + \sum_i \mathbf{c}_\varphi^i\dot{\varphi}^i - d_{\mathrm{rc}}\mathbf{s} \quad (3.28)$$

The different terms are detailed:

$$\begin{aligned}\mathbf{D}_\varepsilon &= \mathbf{E} - \frac{1}{1+h_\varepsilon}\mathbf{Y} \\ \mathbf{c}_{\mathrm{T}} &= b_{\mathrm{T}}\mathbf{1} + d_{\mathrm{T}}\mathbf{s} \\ b_{\mathrm{T}} &= \frac{k_{\mathrm{b}}}{\rho}\sum_i \varphi^i\frac{\mathrm{d}\rho^i}{\mathrm{d}T} - \frac{1}{k_{\mathrm{b}}}\frac{\mathrm{d}k_{\mathrm{b}}}{\mathrm{d}T}p \\ d_{\mathrm{T}} &= \frac{1}{1+h_\varepsilon}\left(\frac{h_\varepsilon}{G}\frac{\mathrm{d}G}{\mathrm{d}T} + \frac{3Gh_{\mathrm{T}}}{\sigma_{\mathrm{y}}}\right) \\ \mathbf{c}_\varphi^i &= b_\varphi^i\mathbf{1} + d_\varphi^i\mathbf{s} \\ b_\varphi^i &= k_{\mathrm{b}}\frac{\rho^i}{\rho} \\ d_\varphi^i &= \frac{1}{1+h_\varepsilon}(h_\varphi^i - h_\varepsilon K^i F^{i\prime})\frac{3G}{\sigma_{\mathrm{y}}} \\ d_{\mathrm{rc}} &= \frac{h_\varepsilon}{1+h_\varepsilon}\frac{3G}{\sigma_{\mathrm{y}}}c_{\mathrm{rc}}\varepsilon^{\mathrm{p}}\end{aligned}$$

where the common notation for the yield tensor $\mathbf{Y}$ is used:

$$\mathbf{Y} = \frac{3G\mathbf{ss}}{\sigma_{\mathrm{y}}^2}$$

The stress rate is composed of four terms, a strain rate dependent part, a temperature rate dependent part, a phase transformation dependent part and a relaxation part. Each term in turn may be decomposed into a bulk term and a deviatoric term.

3.3 Summary

The thermo-plastic problem with phase changes is described by Fourier's equation (3.1) and the mechanical equilibrium equation (3.7):

$$\begin{aligned} \mathbf{q} &= -\kappa \nabla T \\ \boldsymbol{\sigma} \cdot \nabla &= \mathbf{0} \end{aligned}$$

The evolution of temperature and stress is governed by rate equations (3.6) and (3.28):

$$\begin{aligned} \dot{T} &= \frac{-1}{\rho c_{\mathrm{p}}} \nabla \cdot \mathbf{q} - \frac{1}{c_{\mathrm{p}}} \dot{H}_{\varphi} \\ \dot{\boldsymbol{\sigma}} - \mathbf{c}_{\mathrm{T}} \dot{T} &= \mathbf{D}_{\varepsilon} : \mathbf{d} + \sum_{i} \mathbf{c}_{\varphi}^{i} \dot{\varphi}^{i} - d_{\mathrm{rc}} \mathbf{s} \end{aligned}$$

By substitution of the first equation into the second, two coupled equations are obtained. These can be used to set up a coupled system of equations for the heat flow $\mathbf{q}$ and the displacements $\mathbf{u}$. This is shown in Section 5.2. It is more practical, however, to first solve the thermal system and next the mechanical system with known temperatures. This is suggested by the fact that the stresses do not appear in the thermal rate equation.

As we will see in Chapter 4 integration of the rate equations to incremental equations results in a set of fully coupled equations.

4. Finite Time Steps

After one calculation time step, the displacement increments $\Delta\mathbf{u}$ and the heat flow increments vector $\Delta\mathbf{q}$ are obtained. From these the local deformation increment $\Delta\boldsymbol{\varepsilon} = \mathrm{sym}(\nabla\Delta\mathbf{u})$ and the local heat flow divergence $\nabla\cdot(\mathbf{q}+\Delta\mathbf{q})$ are calculated. Based on these the phase fraction increments $\Delta\varphi^i$, the temperature increment ΔT and the stress increment $\Delta\boldsymbol{\sigma}$ are calculated by integration of the rate equations of Chapters 2 and 3.

Predictions for the increments $\Delta\mathbf{u}$ and $\Delta\mathbf{q}$ are calculated based on linearized constitutive equations. When the integrations are based on these predictions, due to the non-linearity the results will deviate from the predictions and residuals may be defined, $\mathbf{R}_\mathrm{q}$ for the $\Delta\mathbf{q}$ equation and $\mathbf{R}_\mathrm{u}$ for the $\Delta\mathbf{u}$ equation. Then, iterative corrections $\delta\mathbf{q}$ and $\delta\mathbf{u}$ are calculated from the residuals and linearized tangents in a Newton iteration process.

The integration of phase fractions is performed according to Section 4.1, Equations (4.1) or (4.6). For integration of the temperature increment, Equation (4.12) from Section 4.2 is used. The stresses are integrated using Equations (4.19) and (4.32) from Section 4.3.

The equations to be solved are non-linear. The integration procedures are linearized to obtain consistently linearized tangents, which should guarantee satisfactory convergence of the Newton iterations. The resulting expressions are Equations (4.2) or (4.8) for the phase transformations, (4.13) for the temperature increment and (4.52) for the stress increment.

As a result two coupled equations for the stress increment and for the temperature increment are obtained. In Section 4.5 these two equations are rewritten as a set of uncoupled equations.

In this chapter increments over a whole step $[t_{n-1}, t_n]$ are indicated as $\Delta f = f(t_n) - f(t_{n-1})$. Iterative updates are written as $\delta f = \Delta f^k - \Delta f^{k-1}$ where k is the iteration sequence number.

4.1 Phase fraction increments $\Delta\varphi$

The simplest way to integrate the phase fraction evolution equations is by multiplying the rates $\dot{\varphi}$, as determined by the state at the start of an increment, by the time increment Δt. For calculations with small time steps this explicit integration may be sufficiently accurate. In this section, however, the implicit integration which is used for larger time steps is elaborated.

Two distinct cases are again discerned when dealing with the phase fraction increment, the martensite transformation and isothermal transformations.

4.1.1 martensite transformation

The calculation of the martensite transformation increment is straightforward. The phase fraction is a function of the temperature and of the stresses ($\varphi^{\mathrm{m}}(T, \boldsymbol{\sigma})$ see Section 2.4.1). Calculation of the phase fraction increment merely involves substitution of the temperature and the stress at the end of the time step:

$$\Delta\varphi^{\mathrm{m}} = \varphi^{\mathrm{m}}(T + \Delta T, \boldsymbol{\sigma} + \Delta\boldsymbol{\sigma}) - \varphi^{\mathrm{m}}(T, \boldsymbol{\sigma}) \tag{4.1}$$

For the Newton iterations a linearized form of this equation is required. This linearized equation is easily obtained by taking the gradient with respect to the temperature and the stresses:

$$\delta\varphi^{\mathrm{m}} = \frac{\partial\varphi^{\mathrm{m}}}{\partial T}\delta T + \frac{\partial\varphi^{\mathrm{m}}}{\partial\boldsymbol{\sigma}} : \delta\boldsymbol{\sigma} \tag{4.2}$$

For the Koistinen-Marburger equation with a stress dependence as in Equation (2.15) this results in:

$$\begin{aligned} \frac{\partial\varphi^{\mathrm{m}}}{\partial T} &= -\beta(\varphi^{\gamma}_{\mathrm{Ms}} - \varphi^{\mathrm{m}}) \\ \frac{\partial\varphi^{\mathrm{m}}}{\partial\boldsymbol{\sigma}} &= \left(\frac{3}{2}\frac{\partial\varphi^{\mathrm{m}}}{\partial\sigma_{\mathrm{eq}}}\frac{\mathbf{s}}{\sigma_{\mathrm{eq}}} - \frac{1}{3}\frac{\partial\varphi^{\mathrm{m}}}{\partial p}\mathbf{1}\right) = \beta(\varphi^{\gamma}_{\mathrm{Ms}} - \varphi^{\mathrm{m}})\left(\frac{3}{2}A_{\mathrm{M}}\frac{\mathbf{s}}{\sigma_{\mathrm{eq}}} + \frac{1}{3}B_{\mathrm{M}}\mathbf{1}\right) \end{aligned} \tag{4.3}$$

4.1.2 diffusion controlled transformations

Diffusional transformations are governed by a kinetic equation which specifies the transformation rate as a function of momentary phase fraction, temperature and stress:

$$\dot{\varphi} = \dot{\varphi}(\varphi, T, \boldsymbol{\sigma}) \tag{4.4}$$

At constant T and $\boldsymbol{\sigma}$ this can be integrated and the result is presented in an isothermal Time-Temperature-Transformation diagram (Figure 2.3). This specifies the time required to obtain a certain amount of phase fraction during isothermal (and iso-stress) conditions. Note, however, that a TTT diagram does not describe a state function $\varphi(t, T)$.

Integration of (4.4) is carried out using the fictitious time method (Hildenwall and Ericson, 1977). From the current fraction a *fictitious* time is calculated which corresponds to the time required to obtain this phase fraction during purely isothermal transformation at the current temperature and stress:

$$t' = \tau\sqrt[n]{\ln(\frac{\varphi_0 - \bar{\varphi}}{\varphi - \bar{\varphi}})} \tag{4.5}$$

The time increment is added and the final fraction is calculated as is shown in Figure 4.1:

$$\Delta\varphi = \left(\varphi(t' + \Delta t) - \varphi(t')\right)\big|_{T,\boldsymbol{\sigma}} \tag{4.6}$$

For the Newton iterations the effect of temperature and stress variations is needed in a linearized form. An approximate linearization is obtained by formally writing the integration

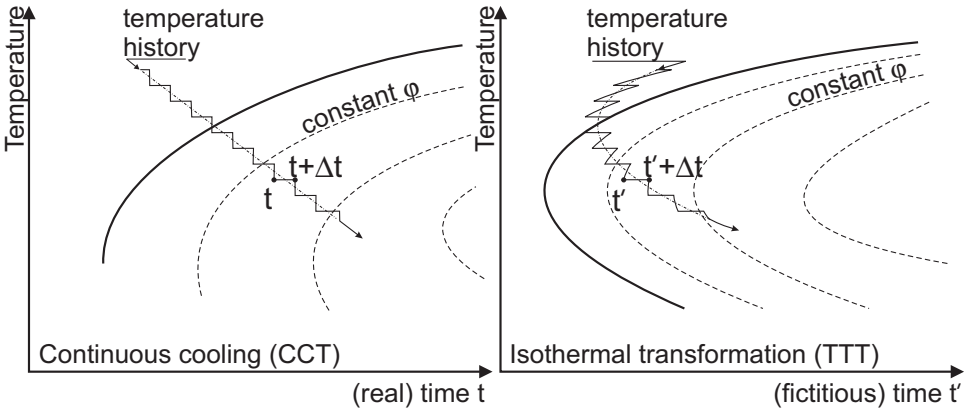

Figure 4.1: Continuous cooling projected onto a CCT diagram and a TTT diagram.

of φ as:

$$\Delta\varphi = \int_0^{\Delta t} \dot{\varphi}\,\mathrm{d}t \approx \int_0^{\Delta t} \left(\dot{\varphi}|_{(T,\boldsymbol{\sigma})} + \frac{\partial\dot{\varphi}}{\partial T}\dot{T}t + \frac{\partial\dot{\varphi}}{\partial\boldsymbol{\sigma}}\dot{\boldsymbol{\sigma}}t \right) \mathrm{d}t \tag{4.7}$$

This yields the linearized tangent for $\Delta\varphi$:

$$\delta\varphi = \frac{1}{2}\frac{\partial\dot{\varphi}}{\partial T}\delta T\,\Delta t + \frac{1}{2}\frac{\partial\dot{\varphi}}{\partial\boldsymbol{\sigma}} : \delta\boldsymbol{\sigma}\,\Delta t \tag{4.8}$$

To obtain an equation of similar form as the equation for martensite (4.2) and also for the sake of brevity we write:

$$\begin{aligned} \Delta\varphi &= \Delta\varphi|_{T,\boldsymbol{\sigma}} \\ \frac{\partial\Delta\varphi}{\partial T} &= \frac{1}{2}\frac{\partial\dot{\varphi}}{\partial T}\Delta t \\ \frac{\partial\Delta\varphi}{\partial\boldsymbol{\sigma}} &= \frac{1}{2}\frac{\partial\dot{\varphi}}{\partial\boldsymbol{\sigma}}\Delta t \end{aligned} \tag{4.9}$$

As has been indicated in Chapter 2 the temperature influences the equilibrium phase fraction $\bar{\varphi}$ as well as the reaction time constant τ. The stress mainly influences the time constant. The derivative of $\dot{\varphi}$ with respect to $\bar{\varphi}$ is evaluated from the approximate rate equation (B.7). The derivative with respect to τ is trivial.

$$\begin{aligned} \frac{\partial\dot{\varphi}}{\partial\bar{\varphi}} &\approx \frac{(1-2n)(\bar{\varphi}-\varphi)+n(\bar{\varphi}-\varphi_0)}{n(\bar{\varphi}-\varphi)(\bar{\varphi}-\varphi_0)}\dot{\varphi} \\ \frac{\partial\dot{\varphi}}{\partial\tau} &= \frac{-\dot{\varphi}}{\tau} \end{aligned} \tag{4.10}$$

Using the definitions of the pressure p and the equivalent stress σ_{eq} and the relation for the stress dependence of τ (2.14), the derivatives of $\Delta\varphi$ to T and $\boldsymbol{\sigma}$ may be evaluated:

$$\begin{aligned}\frac{\partial\Delta\varphi}{\partial T} &= \left(\frac{(1-2n)(\bar{\varphi}-\varphi)+n(\bar{\varphi}-\varphi_0)}{n(\bar{\varphi}-\varphi)(\bar{\varphi}-\varphi_0)}\frac{\partial\bar{\varphi}}{\partial T}-\frac{1}{\tau}\frac{\partial\tau}{\partial T}\right)\frac{\Delta\varphi}{2}\\ \frac{\partial\Delta\varphi}{\partial\boldsymbol{\sigma}} &= \frac{\partial\Delta\varphi}{\partial p}\frac{\partial p}{\partial\boldsymbol{\sigma}}+\frac{\partial\Delta\varphi}{\partial\sigma_{\text{eq}}}\frac{\partial\sigma_{\text{eq}}}{\partial\boldsymbol{\sigma}} = \left(\frac{B_\tau}{3}\mathbf{1}-\frac{3A_\tau}{2}\frac{\mathbf{s}}{\sigma_{\text{eq}}}\right)\frac{\Delta\varphi}{2}\end{aligned} \tag{4.11}$$

For superheated ferrite during heating and undercooled pearlite during cooling extra terms arise due to the correction to the equilibrium phase fraction for the presence of the other phase (Section 2.2.2).

4.2 The temperature increment ΔT

The basis for the computation of the temperature increment is the energy conservation equation (3.2).

$$\rho\dot{H} = -\nabla\cdot\mathbf{q}$$

In this section we concentrate on the left hand side. As far as the right hand side is concerned for the time being a constant heat flow divergence is assumed:

$$\sum_i \rho^i(\varphi^i+\Delta\varphi^i)(H^i+\Delta H^i)-\sum_i\rho^i\varphi^i H^i = -\Delta t\nabla\cdot\mathbf{q} \tag{4.12}$$

This is a non-linear equation so a local Newton iteration is performed to simultaneously solve ΔT and $\Delta\varphi$. After substitution of (4.2) or (4.8) an iterative update is found as:

$$\rho c_{\text{p}}\delta T+\rho\mathbf{h}_{\boldsymbol{\sigma}}:\delta\boldsymbol{\sigma} = -\Delta t\nabla\cdot\mathbf{q}-\rho\Delta H_{\text{T}}-\rho\Delta H_\varphi \tag{4.13}$$

where:

$$\begin{aligned}\rho c_{\text{p}} &= \sum_i\left(\left(\varphi^i+\Delta\varphi^i\right)\rho^i c_{\text{p}}^i+\rho^i H^i\frac{\partial\Delta\varphi^i}{\partial T}\right)\\ \rho\mathbf{h}_{\boldsymbol{\sigma}} &= \sum_i\rho^i H^i\frac{\partial\Delta\varphi^i}{\partial\boldsymbol{\sigma}}\\ \rho\Delta H_{\text{T}} &= \sum_i\rho^i(\varphi^i+\Delta\varphi^i)\Delta H^i\\ \rho\Delta H_\varphi &= \sum_i\rho^i H^i\Delta\varphi^i\end{aligned}$$

The last term on the right hand side is mainly the latent heat of transformation. The first term is an enhanced heat capacity, in which the dependence of the phase fraction increment on the temperature is incorporated. Because the phase fraction increment also depends on the stress increment part of this latent heat is included in the term $\rho\mathbf{h}_{\boldsymbol{\sigma}}:\Delta\boldsymbol{\sigma}$.

4.3 The stress increment $\Delta\boldsymbol{\sigma}$

The stress term is split into a deviatoric part $\mathbf{s}$ and a hydrostatic part p (pressure):

$$\boldsymbol{\sigma} = \mathbf{s} - p\mathbf{1} \tag{4.14}$$

where:

$$p = -\tfrac{1}{3}\,\mathrm{tr}(\boldsymbol{\sigma}) = -\tfrac{1}{3}\boldsymbol{\sigma} : \mathbf{1} \tag{4.15}$$

The strain partitioning of Equation (3.11) is applied to the strain increment:

$$\Delta\boldsymbol{\varepsilon} = \Delta\boldsymbol{\varepsilon}^{\mathrm{el}} + \Delta\boldsymbol{\varepsilon}^{\mathrm{th}} + \Delta\boldsymbol{\varepsilon}^{\mathrm{tr}} + \Delta\boldsymbol{\varepsilon}^{\mathrm{pl}} + \Delta\boldsymbol{\varepsilon}^{\mathrm{tp}} \tag{4.16}$$

The strain increment is, just as with the stress increment, decomposed into a deviatoric strain increment $\Delta\mathbf{e}$ and a spherical volume strain $\Delta\varepsilon^{\mathrm{v}}$:

$$\Delta\boldsymbol{\varepsilon} = \Delta\mathbf{e} + \tfrac{1}{3}\Delta\varepsilon^{\mathrm{v}}\mathbf{1} \tag{4.17}$$

The thermal strain $\Delta\boldsymbol{\varepsilon}^{\mathrm{th}}$ and the transformation dilatation $\Delta\boldsymbol{\varepsilon}^{\mathrm{tr}}$ are purely spherical contributions which give an increment in the hydrostatic pressure. This is elaborated in the following section. The plastic strain $\Delta\boldsymbol{\varepsilon}^{\mathrm{pl}}$ and transformation plasticity $\Delta\boldsymbol{\varepsilon}^{\mathrm{tp}}$ are deviatoric contributions and are detailed in Section 4.3.2

4.3.1 the pressure increment

We first consider the spherical part of the strain increment $\Delta\varepsilon^{\mathrm{v}} = \mathrm{tr}(\Delta\boldsymbol{\varepsilon}) = \Delta\boldsymbol{\varepsilon} : \mathbf{1}$. This induces an increment in the hydrostatic pressure. To calculate it, we compare the pressure at the start and at the end of an increment:

$$\begin{aligned} p &= -k_{\mathrm{b}}(\varepsilon^{\mathrm{v}} - (\boldsymbol{\varepsilon}^{\mathrm{th}} + \boldsymbol{\varepsilon}^{\mathrm{tr}}) : \mathbf{1}) \\ p + \Delta p &= -(k_{\mathrm{b}} + \Delta k_{\mathrm{b}})(\varepsilon^{\mathrm{v}} + \Delta\varepsilon^{\mathrm{v}} - (\boldsymbol{\varepsilon}^{\mathrm{th}} + \Delta\boldsymbol{\varepsilon}^{\mathrm{th}} + \boldsymbol{\varepsilon}^{\mathrm{tr}} + \Delta\boldsymbol{\varepsilon}^{\mathrm{tr}}) : \mathbf{1}) \end{aligned} \tag{4.18}$$

The elastic properties are assumed identical for all phases so that the bulk modulus k_{b} only depends on the temperature. Then $k_{\mathrm{b}} + \Delta k_{\mathrm{b}}$ is the bulk modulus at $T + \Delta T$. This gives rise to an extra term in the equation for Δp:

$$\Delta p = -(k_{\mathrm{b}} + \Delta k_{\mathrm{b}})(\Delta\varepsilon^{\mathrm{v}} - (\Delta\boldsymbol{\varepsilon}^{\mathrm{th}} + \Delta\boldsymbol{\varepsilon}^{\mathrm{tr}}) : \mathbf{1}) + \frac{\Delta k_{\mathrm{b}}}{k_{\mathrm{b}}}p \tag{4.19}$$

An expression for the contributions of the thermal strain and the transformation strain is:

$$\Delta\boldsymbol{\varepsilon}^{\mathrm{th}} + \Delta\boldsymbol{\varepsilon}^{\mathrm{tr}} = \Delta\varepsilon^{\mathrm{th+tr}}\mathbf{1} = \frac{1}{3}\left(\frac{\rho}{\rho + \Delta\rho} - 1\right)\mathbf{1} = \frac{1}{3}\frac{-\Delta\rho}{\rho + \Delta\rho}\mathbf{1} \tag{4.20}$$

The final density $\rho + \Delta\rho$ is found from:

$$\rho + \Delta\rho = \sum_i (\varphi^i + \Delta\varphi^i)(\rho^i + \Delta\rho^i) \tag{4.21}$$

It is useful to identify separate contributions due to temperature and phase fraction increments. A linear expression for $\Delta\varepsilon^{\text{th+tr}}$ is then obtained, which contains 3 terms:

$$\Delta\varepsilon^{\text{th+tr}} = \Delta\varepsilon^{\text{tr}} + \alpha\Delta T + \mathbf{f}^{\text{tr}}_{\boldsymbol{\sigma}} : \Delta\boldsymbol{\sigma} \tag{4.22}$$

where:

$$\begin{aligned}
\Delta\varepsilon^{\text{tr}} &= \frac{-1}{3(\rho+\Delta\rho)}\sum_i \Delta\varphi^i\rho^i \\
\alpha &= \frac{-1}{3(\rho+\Delta\rho)}\sum_i \left(\varphi^i\frac{\mathrm{d}\rho^i}{\mathrm{d}T} + \frac{\partial\Delta\varphi^i}{\partial T}\rho^i\right) \\
\mathbf{f}^{\text{tr}}_{\boldsymbol{\sigma}} &= \frac{-1}{3(\rho+\Delta\rho)}\sum_i \frac{\partial\Delta\varphi^i}{\partial\boldsymbol{\sigma}}\rho^i
\end{aligned}$$

The term $\Delta\varepsilon^{\text{tr}}$ is the autonomous transformation strain. The thermal expansion coefficient α is enhanced with the temperature dependence of the phase fraction increment. The stress dependence of the phase fraction increment is contained in the term $\mathbf{f}^{\text{tr}}_{\boldsymbol{\sigma}}$.

4.3.2 the radial return method

When only elastic deformation occurs, the deviatoric stress can be calculated directly from the strain deviator. We compare this deviatoric stress at the start and at the end of an increment:

$$\begin{aligned}
\mathbf{s} &= 2G\mathbf{e}^{\text{el}} \\
\mathbf{s}+\Delta\mathbf{s} &= 2(G+\Delta G)(\mathbf{e}^{\text{el}}+\Delta\mathbf{e}^{\text{el}})
\end{aligned} \tag{4.23}$$

The increment is obtained when the initial value is subtracted from the final one:

$$\Delta\mathbf{s} = 2(G+\Delta G)\Delta\mathbf{e}^{\text{el}} + \frac{\Delta G}{G}\mathbf{s} \tag{4.24}$$

This incremental relation is used to compute the so-called *elastic trial stress* $\mathbf{s}_{\text{t}}$ from which the classical radial return mapping starts:

$$\mathbf{s}_{\text{t}} = (1+\frac{\Delta G}{G})\mathbf{s} + 2(G+\Delta G)\Delta\mathbf{e} \tag{4.25}$$

From this elastic prediction the plastic terms must be subtracted to find the final stress deviator $\mathbf{s}+\Delta\mathbf{s}$ which is denoted by $\mathbf{s}_1$:

$$\mathbf{s}_1 = \mathbf{s}_{\text{t}} - 2(G+\Delta G)\Delta\boldsymbol{\varepsilon}^{\text{pl}} - 2(G+\Delta G)\Delta\boldsymbol{\varepsilon}^{\text{tp}} \tag{4.26}$$

From here on we write G instead of $(G+\Delta G)$ to indicate the current value of G.

transformation plasticity

The transformation plasticity increment is obtained from integration of the transformation plasticity strain rate:

$$\Delta\boldsymbol{\varepsilon}^{\mathrm{tp}} = \int_0^{\Delta t} \mathbf{d}^{\mathrm{tp}}\,\mathrm{d}t \tag{4.27}$$

Consistent with the radial return method for classical plasticity, the transformation plasticity increment is also approximated using an Euler backward method. In this way instabilities in the stress calculation as discussed by Oddy *et al.* (1992) are easily avoided:

$$\Delta\boldsymbol{\varepsilon}^{\mathrm{tp}} = \frac{3}{2}\sum_i K^i \Delta F^i \frac{\mathbf{s}_1}{\sigma_{\mathrm{y1}}} \tag{4.28}$$

Here σ_{y1} is the yield stress $\sigma_{\mathrm{y}}(\varepsilon^p + \Delta\varepsilon^{\mathrm{p}}, T + \Delta T, \varphi + \Delta\varphi)$. $\sum K^i \Delta F^i$ is evaluated using Equation (2.19) and only for growing phases:

$$\sum_i K^i \Delta F^i = \sum_i K^i (2 - 2\varphi^i - \Delta\varphi^i)\Delta\varphi^i \qquad \forall\, i\,|\Delta\varphi^i > 0 \tag{4.29}$$

From now on we indicate this term as $K\Delta F$. When only transformation plasticity and no regular plasticity occurs, an explicit expression for $\mathbf{s}_1$ is found as follows:

$$\mathbf{s}_1 = \frac{\sigma_{\mathrm{y1}}}{\sigma_{\mathrm{y1}} + 3GK\Delta F}\mathbf{s}_{\mathrm{t}} \tag{4.30}$$

When this value of $\mathbf{s}_1$ does not exceed the yield surface, it is the final value. When $\mathbf{s}_1$ does exceed the yield surface the radial return procedure must be executed from $\mathbf{s}_{\mathrm{t}}$ to correct for plastic strain also.

plastic strain

In the radial return method the plastic strain for the whole time step is taken in the direction of the final deviatoric stress:

$$\Delta\boldsymbol{\varepsilon}^{\mathrm{pl}} = \frac{3}{2}\Delta\lambda\frac{\mathbf{s}_1}{\sigma_{\mathrm{y1}}} \tag{4.31}$$

The value of the equivalent plastic strain increment is derived from the consistency condition, i.e. that the final stress must satisfy the yield condition (3.19). After substitution of (4.28) and (4.31) into (4.26) follows is an implicit equation for $\mathbf{s}_1$:

$$\left(1 + \frac{3G}{\sigma_{\mathrm{y1}}}(\Delta\lambda + K\Delta F)\right)\mathbf{s}_1 = \mathbf{s}_{\mathrm{t}} \tag{4.32}$$

After taking the norm of both sides, a scalar equation is obtained:

$$\sigma_{\mathrm{y1}} + 3G(\Delta\lambda + K\Delta F) = \sigma_{\mathrm{eqt}} \tag{4.33}$$

where $\sigma_{\mathrm{eqt}} = \sqrt{3\mathbf{s}_{\mathrm{t}} : \mathbf{s}_{\mathrm{t}}/2}$. The increment of the plastic multiplier $\Delta\lambda$ is linked to the equivalent plastic strain increment $\Delta\varepsilon^{\mathrm{p}}$ through Equation (3.22):

$$\dot{\varepsilon}^{\mathrm{p}} = \dot{\lambda} - c_{\mathrm{rc}}\varepsilon^{\mathrm{p}}$$

This equation is integrated under the assumption of constant $\dot{\lambda}$ and c_{rc}:

$$\Delta\varepsilon^{\mathrm{p}} c_{\mathrm{rc}}\Delta t = (\Delta\lambda - \varepsilon^{\mathrm{p}} c_{\mathrm{rc}}\Delta t)(1 - \mathrm{e}^{-c_{\mathrm{rc}}\Delta t}) \tag{4.34}$$

which is rearranged as:

$$\Delta\lambda = \frac{c_{\mathrm{cr}}\Delta t}{1 - \exp(-c_{\mathrm{rc}}\Delta t)}\Delta\varepsilon^{\mathrm{p}} + \varepsilon^{\mathrm{p}} c_{\mathrm{rc}}\Delta t = (1 + f_{\mathrm{rc}})\Delta\varepsilon^{\mathrm{p}} + \varepsilon^{\mathrm{p}} c_{\mathrm{rc}}\Delta t \tag{4.35}$$

where for small $c_{\mathrm{rc}}\Delta t$ we have that $f_{\mathrm{cr}} \approx c_{\mathrm{rc}}\Delta t/2$. With this result the consistency iteration to solve the non-linear scalar equation (4.33) is written as:

$$\delta\varepsilon^{\mathrm{p}} = \frac{\sigma_{\mathrm{eqt}} - \sigma_{\mathrm{y}} - 3G(\Delta\lambda + K\Delta F)}{3G(1 + h_{\varepsilon} + f_{\mathrm{rc}})} \tag{4.36}$$

Under the assumption of constant temperature and constant phase fraction increment, the increment of the equivalent plastic strain $\Delta\varepsilon^{\mathrm{p}}$ may be iteratively calculated up to the desired accuracy.

However, neither the temperature nor the phase fractions can be considered constant. Both are coupled to the stress increment. This requires that a coupled set of equations, also involving Equations (4.13) and (4.19) be derived.

4.3.3 consistency iteration

A relatively simple implementation of a consistency iteration is to use a staggered approach:

1 Calculate iteratively $\Delta\varphi$ and ΔT from (4.13) using current values for the stresses.

2 Calculate the pressure increment Δp from (4.19).

3 Calculate the deviatoric stress increment per fraction $\Delta\mathbf{s}^i$ from (4.32) while only iterating for $\Delta\varepsilon^{\mathrm{p}}$ using (4.36).

Repeat from step 1 until convergence is achieved.

A coupled Newton-Raphson type consistency iteration can be derived as follows. Assume that after n iterations a set of intermediate results $(\Delta T_n, \Delta\varphi_n^i, \Delta\boldsymbol{\sigma}_n)$ is available which when substituted into (4.13), (4.19) and (4.33) gives rise to residual values $R_{\mathrm{H}(n)}$, $R_{\mathrm{p}(n)}$ and $R_{\sigma(n)}$. Solve for an iterative update $(\delta T, \delta\varphi^i, \delta\boldsymbol{\sigma})$. From Equation (4.13) we have:

$$\rho c_{\mathrm{p}}\delta T + \rho \mathrm{h}_{\mathrm{p}}\delta p + \rho \mathrm{h}_{\sigma_{\mathrm{eq}}}\delta\sigma_{\mathrm{eq}} = -R_{\mathrm{H}} \tag{4.37}$$

where:

$$\rho \mathrm{h}_{\mathrm{p}} = \sum_i \rho^i H^i \frac{\partial\Delta\varphi^i}{\partial p}$$

$$\rho \mathrm{h}_{\sigma_{\mathrm{eq}}} = \sum_i \rho^i H^i \frac{\partial\Delta\varphi^i}{\partial\sigma_{\mathrm{eq}}}$$

$$R_{\mathrm{H}} = \Delta t\nabla\cdot\mathbf{q} + \rho\Delta H_{\mathrm{T}} + \rho\Delta H_{\varphi}$$

From Equation (4.19) using (4.22):

$$b_{\mathrm{T}}\delta T + (1 - 3k_{\mathrm{b}}\mathrm{f}_{\mathrm{p}}^{\mathrm{tr}})\delta p - 3k_{\mathrm{b}}\mathrm{f}_{\sigma_{\mathrm{eq}}}^{\mathrm{tr}}\delta\sigma_{\mathrm{eq}} = -R_{\mathrm{p}} \tag{4.38}$$

where:

$$\begin{aligned}
b_{\mathrm{T}} &= -3k_{\mathrm{b}}\alpha - \frac{p}{k_{\mathrm{b}}}\frac{\mathrm{d}k_{\mathrm{b}}}{\mathrm{d}T} \\
\mathrm{f}_{\mathrm{p}}^{\mathrm{tr}} &= -\frac{1}{3\rho}\sum_i \rho^i \frac{\partial\Delta\varphi^i}{\partial p} \\
\mathrm{f}_{\sigma_{\mathrm{eq}}}^{\mathrm{tr}} &= -\frac{1}{3\rho}\sum_i \rho^i \frac{\partial\Delta\varphi^i}{\partial\sigma_{\mathrm{eq}}} \\
R_{\mathrm{p}} &= \Delta p + k_{\mathrm{b}}(\Delta\varepsilon^{\mathrm{v}} - 3\Delta\varepsilon^{\mathrm{th+tr}}) - \frac{\Delta k_{\mathrm{b}}}{k_{\mathrm{b}}}p
\end{aligned}$$

In order to obtain an equation for R_σ write all variable terms in (4.33) in incremental form:

$$\delta\sigma_{\mathrm{y}} + 3\delta G(\Delta\lambda + K\Delta F) + 3G(\delta\lambda + KF'\delta\varphi) - \delta\sigma_{\mathrm{eqt}} = -R_\sigma \tag{4.39}$$

For the different terms we already have:

$$\begin{aligned}
\delta\sigma_{\mathrm{eq}} = \delta\sigma_{\mathrm{y}} &= 3Gh_{\mathrm{T}}\delta T + 3Gh_\varepsilon\delta\varepsilon^{\mathrm{p}} + 3Gh_\varphi\delta\varphi \\
\delta G &= \frac{\mathrm{d}G}{\mathrm{d}T}\delta T \\
\delta\lambda &= (1 + f_{\mathrm{rc}})\delta\varepsilon^{\mathrm{p}} \\
\delta\varphi &= \frac{\partial\Delta\varphi}{\partial T}\delta T + \frac{\partial\Delta\varphi}{\partial\sigma_{\mathrm{eq}}}\delta\sigma_{\mathrm{eq}} + \frac{\partial\Delta\varphi}{\partial p}\delta p \\
\delta\sigma_{\mathrm{eqt}} &= \frac{\sigma_{\mathrm{eqt}}}{G}\frac{\mathrm{d}G}{\mathrm{d}T}\delta T
\end{aligned} \tag{4.40}$$

After substitution and sorting out terms with δT, δp and $\delta\sigma_{\mathrm{eq}}$ the following expression remains:

$$S_{\mathrm{T}}\delta T + S_{\mathrm{p}}\delta p + (1 + S_\sigma)\delta\sigma_{\mathrm{eq}} = -R_\sigma \tag{4.41}$$

where:

$$\begin{aligned}
S_{\mathrm{T}} &= 3G\left(KF'\frac{\partial\Delta\varphi}{\partial T} - \frac{1 + f_{\mathrm{rc}}}{h_\varepsilon}(h_{\mathrm{T}} + h_\varphi\frac{\partial\Delta\varphi}{\partial T})\right) - \frac{\sigma_{\mathrm{y}}}{G}\frac{\mathrm{d}G}{\mathrm{d}T} \\
S_{\mathrm{p}} &= 3G\left(KF' - \frac{(1 + f_{\mathrm{rc}})h_\varphi}{h_\varepsilon}\right)\frac{\partial\Delta\varphi}{\partial p} \\
S_\sigma &= \frac{1 + f_{\mathrm{rc}}}{h_\varepsilon} + 3G\left(KF' - \frac{(1 + f_{\mathrm{rc}})h_\varphi}{h_\varepsilon}\right)\frac{\partial\Delta\varphi}{\partial\sigma_{\mathrm{eq}}} \\
R_\sigma &= \frac{1}{3G}(\sigma_{\mathrm{y1}} + 3G(\Delta\lambda + K\Delta F) - \sigma_{\mathrm{eqt}})
\end{aligned}$$

This is the third equation. Summarizing:

$$\begin{bmatrix} \rho c_\mathrm{p} & \rho \mathrm{h}_\mathrm{p} & \rho \mathrm{h}_\sigma \\ b_\mathrm{T} & 1-3k_\mathrm{b}\mathrm{f}_\mathrm{p}^\mathrm{tr} & -3k_\mathrm{b}\mathrm{f}_{\sigma_\mathrm{eq}}^\mathrm{tr} \\ S_\mathrm{T} & S_\mathrm{p} & 1+S_\sigma \end{bmatrix} \begin{Bmatrix} \delta T \\ \delta p \\ \delta\sigma_\mathrm{eq} \end{Bmatrix} = \begin{Bmatrix} -R_\mathrm{H} \\ -R_\mathrm{p} \\ -R_\sigma \end{Bmatrix} \tag{4.42}$$

For thermo-mechanical computations with phase transformations, consistency iteration involves the solution of a system of three coupled equations.

4.4 Consistent tangent

After having calculated consistent increments of temperature as well as stress, these can be substituted into the respective balance equations in order to be checked for convergence. Based on the unbalance, new estimates for the heat flow and displacement increments $\Delta\mathbf{q}$ and $\Delta\mathbf{u}$ are calculated.

We assume that as a result of the previous m equilibrium iterations a set of intermediate results $(\Delta\mathbf{q}^m, \Delta\mathbf{u}^m)$ is available, from which temperatures, phase fractions and stresses $(T^m, \varphi^m, \boldsymbol{\sigma}^m)$ are calculated. Now we solve for an iterative update $(\Delta\mathbf{q}^m+\delta\mathbf{q}, \Delta\mathbf{u}^m+\delta\mathbf{u})$.

For the thermal problem, Equation (4.13) with coefficients evaluated with (T^m, φ^m) is used. The increment of the hydrostatic pressure is also easily expressed in the temperature and strain variations using (4.19) and (4.22) with coefficients evaluated with (T^m, φ^m):

$$\delta p = -k_\mathrm{b}\delta\varepsilon^\mathrm{v} + 3k_\mathrm{b}\mathbf{f}_{\boldsymbol{\sigma}}^\mathrm{tr} : \delta\boldsymbol{\sigma} - b_\mathrm{T}\delta T \tag{4.43}$$

Derivation of the consistent tangential stiffness of the deviatoric stress increment starts from (4.33) which yields an expression for the variation of the equivalent plastic strain $\delta\varepsilon^\mathrm{p}$:

$$\begin{aligned}\delta\varepsilon^\mathrm{p} = -\frac{1}{1+h_\varepsilon+f_\mathrm{rc}}\left(h_\mathrm{T}+\frac{1}{G}\frac{\mathrm{d}G}{\mathrm{d}T}(\Delta\lambda+K\Delta F-\frac{\sigma_\mathrm{eqt}}{3G})\right)\delta T + \\ -\frac{1}{1+h_\varepsilon+f_\mathrm{rc}}(KF'+h_\varphi)\delta\varphi+\frac{1}{1+h_\varepsilon+f_\mathrm{rc}}\frac{\mathbf{s}}{\sigma_\mathrm{y}}:\delta\mathbf{e}\end{aligned} \tag{4.44}$$

where all coefficients and state variables are evaluated with $(T^m, \varphi^m, \boldsymbol{\sigma}^m)$. Next, (4.32) is written in a differential form:

$$\begin{aligned}\left((\frac{3\delta G}{\sigma_\mathrm{y}}-\frac{3G}{(\sigma_\mathrm{y})^2}\delta\sigma_\mathrm{y})(\Delta\lambda+K\Delta F)+\frac{3G}{\sigma_\mathrm{y}}(\delta\lambda+KF'\delta\varphi)\right)\mathbf{s}+ \\ +\left(1+\frac{3G}{\sigma_\mathrm{y}}(\Delta\lambda+K\Delta F)\right)\delta\mathbf{s}=2G\delta\mathbf{e}+\frac{1}{G}\frac{\mathrm{d}G}{\mathrm{d}T}\mathbf{s}\delta T\end{aligned} \tag{4.45}$$

Substitution of (4.44) and the relations in (4.40) into the above, yields the expression for the variation of the stress deviator $\delta\mathbf{s}$:

$$\delta\mathbf{s} = \mathbf{D}_\mathbf{e} :\ \delta\mathbf{e} + d_\mathrm{T}\mathbf{s}\delta T + \sum_i d_\varphi^i \mathbf{s}\frac{\partial\Delta\varphi^i}{\partial\boldsymbol{\sigma}} : \delta\boldsymbol{\sigma} \tag{4.46}$$

where using identical notations as in Equation (3.28):

$$\mathbf{D_e} = \frac{2G\sigma_y}{\sigma_y + 3G(\Delta\lambda + K\Delta F)}\mathbf{I} - \frac{(1+f_{rc})\sigma_y - 3Gh_\varepsilon(\Delta\lambda + K\Delta F)}{\sigma_y + 3G(\Delta\lambda + K\Delta F)}\frac{1}{1+h_\varepsilon + f_{rc}}\mathbf{Y}$$

$$d_T = \frac{1}{1+h_\varepsilon + f_{rc}}\left(\frac{h_\varepsilon}{G}\frac{\mathrm{d}G}{\mathrm{d}T} + (1+f_{rc})\frac{3Gh_T}{\sigma_y}\right) + \sum_i d_\varphi^i \frac{\partial\Delta\varphi^i}{\partial T}$$

$$d_\varphi^i = \frac{(1+f_{rc})h_\varphi^i - h_\varepsilon K^i F^{i'}}{1+h_\varepsilon + f_{rc}}\frac{3G}{\sigma_y}$$

This result is then combined with the pressure terms from (4.43) to obtain:

$$\left(\mathbf{I} - \sum_i b_\varphi^i \mathbf{1}\frac{\partial\Delta\varphi^i}{\partial\boldsymbol{\sigma}} - \sum_i d_\varphi^i \mathbf{s}\frac{\partial\Delta\varphi^i}{\partial\boldsymbol{\sigma}}\right) : \delta\boldsymbol{\sigma} - (b_T\mathbf{1} + d_T\mathbf{s})\delta T = \mathbf{D_e} : \delta\boldsymbol{\varepsilon} + \left(k_b - \frac{1}{3}\frac{2G\sigma_y}{\sigma_y + 3G(\Delta\lambda + K\Delta F)}\right)\mathbf{11} : \delta\boldsymbol{\varepsilon} \quad (4.47)$$

An explicit equation for $\delta\boldsymbol{\sigma}$ is derived by inverting the prefactor. This can be done in closed form. The phase fraction increment $\Delta\varphi$ is actually a function of the hydrostatic pressure p and the equivalent stress σ_{eq}. For the partial derivative write:

$$\frac{\partial\Delta\varphi^i}{\partial\boldsymbol{\sigma}} = -\frac{1}{3}\frac{\partial\Delta\varphi^i}{\partial p}\mathbf{1} + \frac{3}{2}\frac{\partial\Delta\varphi^i}{\partial\sigma_{eq}}\frac{\mathbf{s}}{\sigma_{eq}} \quad (4.48)$$

Substitution into (4.47) yields:

$$\left(\mathbf{I} - b_p\mathbf{11} - b_s\mathbf{1s} - d_p\mathbf{s1} - d_s\mathbf{ss}\right) : \delta\boldsymbol{\sigma} - (b_T\mathbf{1} + d_T\mathbf{s})\delta T = \mathbf{D_e} : \delta\boldsymbol{\varepsilon} + \left(k_b - \frac{1}{3}\frac{2G\sigma_y}{\sigma_y + 3G(\Delta\lambda + K\Delta F)}\right)\mathbf{11} : \delta\boldsymbol{\varepsilon} \quad (4.49)$$

where:

$$b_p = -\frac{1}{3}\frac{k_b}{\rho}\sum_i \rho^i \frac{\partial\Delta\varphi^i}{\partial p}$$

$$b_s = \frac{3}{2}\frac{k_b}{\rho\sigma_{eq}}\sum_i \rho^i \frac{\partial\Delta\varphi^i}{\partial\sigma_{eq}}$$

$$d_p = -\frac{1}{1+h_\varepsilon + f_{rc}}\frac{G}{\sigma_y}\sum_i((1+f_{rc})h_\varphi^i - h_\varepsilon K^i F'^i)\frac{\partial\Delta\varphi^i}{\partial p}$$

$$d_s = \frac{1}{1+h_\varepsilon + f_{rc}}\frac{9G}{2\sigma_y^2}\sum_i((1+f_{rc})h_\varphi^i - h_\varepsilon K^i F'^i)\frac{\partial\Delta\varphi^i}{\partial\sigma_{eq}}$$

The inverse of the prefactor is found from:

$$(\mathbf{I} + c_1\mathbf{11} + c_2\mathbf{1s} + c_3\mathbf{s1} + c_4\mathbf{ss}) : (\mathbf{I} - b_p\mathbf{11} - b_s\mathbf{1s} - d_p\mathbf{s1} - d_s\mathbf{ss}) = \mathbf{I} \quad (4.50)$$

which yields:

$$\begin{Bmatrix} c_1 \\ c_2 \\ c_3 \\ c_4 \end{Bmatrix} = \frac{1}{(1-3b_\mathrm{p})(1-\frac{2}{3}d_\mathrm{s}\sigma_\mathrm{eq}^2) - 2b_\mathrm{s}d_\mathrm{p}\sigma_\mathrm{eq}^2} \begin{Bmatrix} b_\mathrm{p} + \frac{2}{3}\sigma_\mathrm{eq}^2(b_\mathrm{s}d_\mathrm{p} - b_\mathrm{p}d_\mathrm{s}) \\ b_\mathrm{s} \\ d_\mathrm{p} \\ d_\mathrm{s} + 3b_\mathrm{s}d_\mathrm{p} - 3b_\mathrm{p}d_\mathrm{s} \end{Bmatrix} \tag{4.51}$$

Substitute this into (4.49) to find:

$$\delta\boldsymbol{\sigma} - \mathbf{c}_\mathrm{T}\delta T = \mathbf{D}_\varepsilon : \delta\boldsymbol{\varepsilon} \tag{4.52}$$

where:

$$\begin{aligned} \mathbf{c}_\mathrm{T} =& b_\mathrm{T}\mathbf{1} + d_\mathrm{T}\mathbf{s} + 3b_\mathrm{T}(c_1\mathbf{1} + c_3\mathbf{s}) + \tfrac{2}{3}d_\mathrm{T}(c_2\mathbf{1} + c_4\mathbf{s})\sigma_\mathrm{eq}^2 \\ \mathbf{D}_\varepsilon =& \frac{2G\sigma_\mathrm{y}}{\sigma_\mathrm{y} + 3G(\Delta\lambda + K\Delta F)}\left(\mathbf{I} - \tfrac{1}{3}\mathbf{11}\right) + k_\mathrm{b}\mathbf{11} \\ & - \frac{(1+f_\mathrm{rc})\sigma_\mathrm{y} - 3Gh_\varepsilon(\Delta\lambda + K\Delta F)}{\sigma_\mathrm{y} + 3G(\Delta\lambda + K\Delta F)}\frac{1}{1+h_\varepsilon+f_\mathrm{rc}}\mathbf{Y} \\ & + \frac{2Gh_\varepsilon}{1+h_\varepsilon+f_\mathrm{rc}}(c_2\mathbf{1s} + c_4\mathbf{ss}) + 3k_\mathrm{b}(c_1\mathbf{11} + c_3\mathbf{s1}) \end{aligned}$$

This is a fully coupled consistently linearized equation for the stress update, valid for small deformation gradients. The first three terms in the definition of $\mathbf{D}_\varepsilon$ may be identified as the regular consistent tangent modulus with small adaptions for transformation plasticity ($K\Delta F$) and plastic recovery (f_rc). The only modification to $\mathbf{D}_\varepsilon$ as well as to $\mathbf{c}_\mathrm{T}$ is the addition of the last two terms which contain the coupling between phase fraction increments and stresses.

4.5 Thermo-mechanical coupling

Our model now consists of two coupled equations (4.13) and (4.52).

$$\begin{aligned} \rho c_\mathrm{p}\delta T + \rho\mathbf{h}_{\boldsymbol{\sigma}} : \delta\boldsymbol{\sigma} &= -\Delta t\nabla\cdot\delta\mathbf{q} \\ \delta\boldsymbol{\sigma} - \mathbf{c}_\mathrm{T}\delta T &= \mathbf{D}_\varepsilon : \delta\boldsymbol{\varepsilon} \end{aligned} \tag{4.53}$$

Neither $\boldsymbol{\sigma}$ nor T will be primary variables in the final element model as derived in Chapter 5. Therefore both variables will be made explicit.

$$\begin{aligned} \delta T &= -\frac{\Delta t}{\rho c_\mathrm{p} + \rho\mathbf{h}_{\boldsymbol{\sigma}} : \mathbf{c}_\mathrm{T}}\nabla\cdot\delta\mathbf{q} - \frac{\rho\mathbf{h}_{\boldsymbol{\sigma}}}{\rho c_\mathrm{p} + \rho\mathbf{h}_{\boldsymbol{\sigma}} : \mathbf{c}_\mathrm{T}} : \mathbf{D}_\varepsilon : \delta\boldsymbol{\varepsilon} \\ \delta\boldsymbol{\sigma} &= -\frac{\mathbf{c}_\mathrm{T}\Delta t}{\rho c_\mathrm{p} + \rho\mathbf{h}_{\boldsymbol{\sigma}} : \mathbf{c}_\mathrm{T}}\nabla\cdot\delta\mathbf{q} + \left(\mathbf{I} - \frac{\rho\mathbf{c}_\mathrm{T}\mathbf{h}_{\boldsymbol{\sigma}}}{\rho c_\mathrm{p} + \rho\mathbf{h}_{\boldsymbol{\sigma}} : \mathbf{c}_\mathrm{T}}\right) : \mathbf{D}_\varepsilon : \delta\boldsymbol{\varepsilon} \end{aligned} \tag{4.54}$$

These equations are suited for implementation in a finite element model. An obvious implementation would be to formulate a fully coupled problem with both $\delta\mathbf{q}$ and $\delta\mathbf{u}$ as primary variables. A simpler implementation would be to formulate a staggered scheme by suitably partitioning the coupled equations.

Here a partitioning is proposed in a thermal step without distortion ($\delta\boldsymbol{\varepsilon} = \mathbf{0}$) followed by a mechanical step with constant heat conduction ($\delta\mathbf{q} = \text{const.}$).

4.6 Summary

In this chapter and in Chapter 3 constitutive equations were derived for the numerical analysis of processes involving solid state phase transformations. In Chapter 3 rate equations (3.6) and (3.28) were obtained by regarding the phase transformations as an autonomous process.

The phase transformations are governed by the temperature and the stress. The equation for the martensite transformation has the character of a state equation $\varphi^{\mathrm{m}}(T, \boldsymbol{\sigma})$. The diffusion controlled transformations from ferrite and pearlite to austenite (and back) are described by rate equations $\dot{\varphi}(\varphi, T, \boldsymbol{\sigma})$ the integration of which must be carried out with care. Proper evaluation of stress and temperature dependence and inclusion into the constitutive equations finally yields incremental equations (4.13) and (4.52) which are considerably more complex than the rate equations of Chapter 3.

In Chapter 6 an effort will be made to asses how much of this complexity is required for successful simulation of transformation hardening.

5. Finite Element Discretization

When a coupled solution of distortions and heat flow is required, the interpolations of stresses and temperatures should preferably be of the same order (Oddy *et al.*, 1990). For simulation of the residual stress due to phase transformations a finite element program has been written based on a discretization using quadratic triangular elements. This means that the displacements are continuous and piecewise quadratic. Consequently strains and stresses are discontinuous and linearly distributed per element.

In this chapter a finite element discretization of the heat conduction problem is shown which is based on a discontinuous discretization of the temperature field. The heat flow is the primary variable. The consistency of strains and temperatures is one reason for choosing this discretization. A second reason is that the numerical treatment of the convection equations which arise in the Arbitrary Lagrangian-Eulerian formulation (Chapter 7) and in the steady state formulation (Chapter 8) yields discontinuously interpolated state variable fields. So a finite element method is required which can deal with discontinuously interpolated temperatures.

The discretization of the equilibrium equations (3.7) is standard and will not be elaborated on here.

5.1 Thermal analysis using heat flow elements

The unsteady heat conduction is governed by the set of equations (3.1), i.e. Fourier's law for the heat flow due to a thermal gradient and (3.6), i.e. the constitutive equation expressing the temperature rate as a function of the heat flow divergence:

$$\mathbf{q} = -\kappa \nabla T \tag{5.1a}$$

$$\rho c_\mathrm{p} \dot{T} = -\nabla \cdot \mathbf{q} - \rho \dot{H}_\varphi \tag{5.1b}$$

The specific heat capacity ρc_p is found by summation over the phases, the heat source term $\dot{H}_\varphi$ contains the latent heat of transformation as explained in Chapters 3 and 4. The boundary conditions may be any combination of prescribed heat flow (e.g. laser irradiation or isolation), prescribed temperature or a mixed condition (e.g. convective heat transfer to the environment):

$$\mathbf{q} \cdot \mathbf{n} = q_0 \qquad \text{on } \Gamma = \Gamma_\mathrm{q} \tag{5.2a}$$

$$T = T_0 \qquad \text{on } \Gamma = \Gamma_\mathrm{T} \tag{5.2b}$$

$$\mathbf{q} \cdot \mathbf{n} = \gamma (T - T_\mathrm{e}) \qquad \text{on } \Gamma = \Gamma_\mathrm{e} \tag{5.2c}$$

The common method to solve transient heat conduction is to substitute (5.1a) into (5.1b) to obtain an equation exclusively in T. Here, however, Equation (5.1a) will be discretized to obtain a system with the heat flow $\mathbf{q}$ as the primary variable. When the temperature is also approximated by interpolation with temperature degrees of freedom as primary variables this is called a *mixed* method (Roberts and Thomas, 1991). In our implementation the temperature is treated as a state variable which is to be evaluated and integrated locally.

Following the standard Galerkin procedure the first equation is written in the weak form. The weight functions are the vector functions $\mathbf{r}$, where $\mathbf{r} \cdot \mathbf{n} = 0$ on Γ_q:

$$\int_V \mathbf{r} \cdot \mathbf{q} \, \mathrm{d}V = \int_V -\kappa \mathbf{r} \cdot \nabla T \, \mathrm{d}V \qquad \forall \mathbf{r} \tag{5.3}$$

We apply partial integration to the right hand side to obtain:

$$\int_V \mathbf{r} \cdot \mathbf{q} \, \mathrm{d}V = \int_V \kappa \nabla \cdot \mathbf{r} T \, \mathrm{d}V - \int_{\Gamma_\mathrm{T} \cup \Gamma_\mathrm{e}} \kappa \mathrm{r_n} T \, \mathrm{d}\Gamma \tag{5.4}$$

where $\mathrm{r_n} = \mathbf{r} \cdot \mathbf{n}$. The boundary conditions on Γ_T (5.2b) and Γ_e (5.2c) are substituted into (5.3) which yields:

$$\int_V \mathbf{r} \cdot \mathbf{q} \, \mathrm{d}V + \int_{\Gamma_\mathrm{e}} \frac{\kappa}{\gamma} \mathrm{r_n} \mathrm{q_n} \, \mathrm{d}\Gamma = \int_V \kappa \nabla \cdot \mathbf{r} T \, \mathrm{d}V - \int_{\Gamma_\mathrm{T}} \kappa \mathrm{r_n} T_0 \, \mathrm{d}\Gamma - \int_{\Gamma_\mathrm{e}} \kappa \mathrm{r_n} T_\mathrm{e} \, \mathrm{d}\Gamma \tag{5.5}$$

For discretization we choose interpolation functions such that the heat flow field $\mathbf{q}$ is continuous across element boundaries, whereas the temperatures T are allowed to be discontinuous. With reference to a two-dimensional discretization, the calculation domain V is divided into N_e non-overlapping triangles (or elements) V_n such that $V = \cup_{n=1}^{N_\mathrm{e}} V_n$. On V_n $\mathbf{q}$ and $\mathbf{r}$ are approximated using interpolation functions Q_n^k which are connected with nodes (k) on edges and vertices of the element. The functions Q_n^k and Q_m^k are C_0 continuous across element edges and have the value $Q_n^k(\mathbf{x}_k) = Q_m^k(\mathbf{x}_k) = 1$ and $Q_n^k(\mathbf{x}_l) = 0$ for $k \neq l$:

$$\mathbf{q}_\mathrm{h}^n(\mathbf{x}) = \sum_k Q_n^k(\mathbf{x}) \mathbf{q}_k \tag{5.6}$$

No explicit discretization of T is needed, it may be evaluated at the integration points.

5.1.1 incremental formulation

For large time steps the explicit method of Section 5.1 is not sufficient. We have to incorporate the finite time steps into our equations. In order to achieve this we write Equation (5.1) in an implicit form. We require that Fourier's equation is satisfied at the end of the time step $t \to t + \Delta t$. The temperature increment depends on the evolution of the heat flow during the time step. This is written as a generalized mid point formula (Zienkiewicz and Taylor (1991), Vol. 2, Ch. 10):

$$\begin{aligned} \mathbf{q} + \Delta \mathbf{q} &= -\kappa \nabla (T + \Delta T) \\ \rho c_\mathrm{p} \Delta T &= -\nabla \cdot (\mathbf{q} + \theta \Delta \mathbf{q}) \Delta t - \rho \Delta H_\varphi \end{aligned} \tag{5.7}$$

In Zienkiewicz and Taylor (1991) an optimal value of $\theta = 2/3$ is recommended. We substitute the second equation of (5.7) into the first:

$$\Delta\mathbf{q} - \theta\frac{\kappa\Delta t}{\rho c_\mathrm{p}}\nabla\nabla\cdot\Delta\mathbf{q} = \frac{\kappa}{\rho c_\mathrm{p}}\nabla(\nabla\cdot\mathbf{q}\Delta t + \rho\Delta H_\varphi) \tag{5.8}$$

In order to obtain a finite element model we write this in the weak form:

$$\int_V \mathbf{r}\cdot(\Delta\mathbf{q} - \theta\frac{\kappa\Delta t}{\rho c_\mathrm{p}}\nabla\nabla\cdot\Delta\mathbf{q})\,\mathrm{d}V = \int_V \frac{\kappa}{\rho c_\mathrm{p}}\mathbf{r}\cdot\nabla(\nabla\cdot\mathbf{q}\Delta t + \rho\Delta H_\varphi)\,\mathrm{d}V \qquad \forall\mathbf{r} \tag{5.9}$$

After applying partial integration, using the second line of (5.7) and substituting the boundary conditions, we finally find:

$$\int_V \left(\mathbf{r}\cdot\Delta\mathbf{q} + \theta\frac{\kappa\Delta t}{\rho c_\mathrm{p}}(\nabla\cdot\mathbf{r})(\nabla\cdot\Delta\mathbf{q})\right)\mathrm{d}V + \int_{\Gamma_\mathrm{e}}\frac{\kappa}{\gamma}\mathrm{r_n}\Delta\mathrm{q_n}\,\mathrm{d}\Gamma = - \int_V \frac{\kappa}{\rho c_\mathrm{p}}(\nabla\cdot\mathbf{r})(\nabla\cdot\mathbf{q}\Delta t + \rho\Delta H_\varphi)\,\mathrm{d}V \tag{5.10}$$

The computation of ΔT is performed element by element on the basis of Equation (4.12). Non-linear terms are present in the (temperature dependent) material properties as well as in the source term. This means that after adding ΔT to T, the residue of (5.1a) must be determined and an iterative correction $\delta\mathbf{q}$ to $\Delta\mathbf{q}$ must be calculated.

5.2 Coupled thermo-mechanical analysis

In Chapter 4 the fully coupled constitutive equations for the temperature and stress increments were derived:

$$\begin{aligned}\Delta T &= -\frac{\theta\Delta t}{\rho c_\mathrm{v}^*}\nabla\cdot\Delta\mathbf{q} - \frac{\mathbf{d}_{\mathrm{T}\varepsilon}}{\rho c_\mathrm{v}^*}:\Delta\boldsymbol{\varepsilon} - \frac{\Delta t}{\rho c_\mathrm{v}^*}\nabla\cdot\mathbf{q} - \frac{\rho\Delta H^*}{\rho c_\mathrm{v}^*}\\ \Delta\boldsymbol{\sigma} &= -\mathbf{c}_\mathrm{T}\frac{\theta\Delta t}{\rho c_\mathrm{v}^*}\nabla\cdot\Delta\mathbf{q} + \mathbf{D}_{\sigma\varepsilon}:\Delta\boldsymbol{\varepsilon} + \Delta\boldsymbol{\sigma}^*\end{aligned} \tag{5.11}$$

where:

$$\begin{aligned}\rho c_\mathrm{v}^* &= \rho c_\mathrm{p} + \rho\mathbf{h}_{\boldsymbol{\sigma}}:\mathbf{c}_\mathrm{T}\\ \mathbf{d}_{\mathrm{T}\varepsilon} &= \rho\mathbf{h}_{\boldsymbol{\sigma}}:\mathbf{D}_\varepsilon\\ \rho\Delta H^* &= \rho\Delta H_\varphi + \rho\mathbf{h}_{\boldsymbol{\sigma}}:(\mathbf{c}_\varphi\Delta\varphi + \mathbf{s}d_\mathrm{rc}\Delta t)\\ \mathbf{D}_{\sigma\varepsilon} &= \left(\mathbf{I} - \frac{\rho\mathbf{c}_\mathrm{T}\mathbf{h}_{\boldsymbol{\sigma}}}{\rho c_\mathrm{v}^*}\right):\mathbf{D}_\varepsilon\\ \Delta\boldsymbol{\sigma}^* &= \mathbf{c}_\varphi\Delta\varphi + \mathbf{s}d_\mathrm{rc}\Delta t - \frac{\mathbf{c}_\mathrm{T}}{\rho c_\mathrm{v}^*}\left(\nabla\cdot\mathbf{q}\Delta t + \rho\Delta H^*\right)\end{aligned}$$

The thermal equation is discretized as in Section 5.1.1. The mechanical equilibrium equations are discretized in the usual way:

$$\int_V \mathbf{w} \cdot ((\boldsymbol{\sigma} + \Delta\boldsymbol{\sigma}) \cdot \nabla) dV = 0 \qquad \forall \mathbf{w} \tag{5.12}$$

where $\mathbf{w}$ is a vector weight function. After substitution of the constitutive equations, partial integration and substitution of the boundary conditions, the following set of coupled discretized equations is obtained:

$$\int_V \left(\mathbf{r} \cdot \Delta\mathbf{q} + \theta \frac{\kappa \Delta t}{\rho c_v^*} (\nabla \cdot \mathbf{r})(\nabla \cdot \Delta\mathbf{q}) \right) \mathrm{d}V + \int_{\Gamma_e} \frac{\kappa}{\gamma} r_n \Delta q_n \, \mathrm{d}\Gamma + \int_V \frac{\kappa}{\rho c_v^*} (\nabla \cdot \mathbf{r}) \mathbf{d}_{T\varepsilon} : \Delta\boldsymbol{\varepsilon} \, \mathrm{d}V = - \int_V \frac{\kappa}{\rho c_v^*} (\nabla \cdot \mathbf{r})(\nabla \cdot \mathbf{q} \Delta t + \rho \Delta H^*) \, \mathrm{d}V \tag{5.13a}$$

and:

$$- \int_V \mathrm{sym}(\nabla \mathbf{w}) : \mathbf{c}_T \nabla \cdot \Delta\mathbf{q} \, \mathrm{d}V + \int_V \mathrm{sym}(\nabla \mathbf{w}) : \mathbf{D}_{\sigma\varepsilon} : \Delta\boldsymbol{\varepsilon} \, \mathrm{d}V = - \int_V \mathrm{sym}(\nabla \mathbf{w}) : (\boldsymbol{\sigma} + \Delta\boldsymbol{\sigma}^*) \, \mathrm{d}V + \int_{\Gamma_t} \mathbf{w} \cdot \mathbf{t} \, \mathrm{d}\Gamma \tag{5.13b}$$

where $\mathbf{t}$ is the prescribed traction on boundary section Γ_t:

$$\boldsymbol{\sigma} \cdot \mathbf{n} = \mathbf{t} \qquad \text{on } \Gamma_t \tag{5.14}$$

5.2.1 staggered solution approach

The Equations (5.13) constitute a coupled system in the degrees of freedom $\Delta\mathbf{q}$ and $\Delta\mathbf{u}$. This can be solved by assembly of the full system and simultaneous solution of all degrees of freedom. Alternatively an operator split may be applied by solving the thermal system first and the mechanical system next. The isochoric thermal system is readily found from (5.13a) by setting $\Delta\boldsymbol{\varepsilon} = \mathbf{0}$:

$$\int_V \left(\mathbf{r} \cdot \Delta\mathbf{q} + \theta \frac{\kappa \Delta t}{\rho c_v^*} (\nabla \cdot \mathbf{r})(\nabla \cdot \Delta\mathbf{q}) \right) \mathrm{d}V + \int_{\Gamma_e} \frac{\kappa}{\gamma} r_n \Delta q_n \, \mathrm{d}\Gamma = - \int_V \frac{\kappa}{\rho c_v^*} (\nabla \cdot \mathbf{r})(\nabla \cdot \mathbf{q} \Delta t + \rho \Delta H^*) \, \mathrm{d}V \tag{5.15}$$

From the solution $\Delta\mathbf{q}$ (with $\Delta\boldsymbol{\varepsilon} = \mathbf{0}$), the temperature increment ΔT^{th}, the phase fraction increment $\Delta\varphi^{\text{th}}$ and the thermal stress increment $\Delta\boldsymbol{\sigma}^{\text{th}}$ are calculated. Next, the mechanical problem is solved from (5.13b) with $\Delta\mathbf{q} = \mathbf{0}$:

$$\int_V \text{sym}(\nabla\mathbf{w}) : \mathbf{D}_{\sigma\varepsilon} : \Delta\boldsymbol{\varepsilon}\, \mathrm{d}V = -\int_V \text{sym}(\nabla\mathbf{w}) : (\boldsymbol{\sigma} + \Delta\boldsymbol{\sigma}^{\text{th}})\, \mathrm{d}V + \int_{\Gamma_t} \mathbf{w}\cdot\mathbf{t}\, \mathrm{d}\Gamma \quad (5.16)$$

and the final values of the increments ΔT, $\Delta\varphi$ and $\Delta\boldsymbol{\sigma}$ are calculated.

The staggered solution approach as described here was implemented in the finite element model. Each time step comprised several equilibrium iterations such that during every iteration first an update $\delta\mathbf{q}$ to $\Delta\mathbf{q}$ was calculated. Next, a new displacement increment $\Delta\mathbf{u} + \delta\mathbf{u}$ was calculated based on the current value of $\Delta\boldsymbol{\sigma}^{\text{th}}$.

5.3 Summary

The equations of Chapter 4 were discretized in a finite element model. For the thermal equations a discretization was chosen with the heatflow $\mathbf{q}$ as the primary variable. The discretization of the mechanical equilibrium was carried out in a standard way, i.e. with the displacements $\mathbf{u}$ as primary variables. The temperatures, phase fractions, stresses and strains were treated as secondary variables, only evaluated at the element integration points. The coupled thermo-mechanical problem was implemented via a staggered approach.

6. Examples

6.1 Simulations of standard hardening tests

6.1.1 Jominy test

A well known method for determining hardenability is the so-called Jominy test. A 100 mm long bar is heated to austenization temperature and held there for the required time. Next it is quenched by applying a strong water jet to one of the end faces. The hardenability is determined by measuring the hardness along the length of the bar.

When the test is carried out correctly the cooling only happens at the quenched face and the temperatures will be more or less homogeneous in each cross section. This means that a one dimensional model is sufficient to simulate it. The finite element model contains 32 triangular 6-node elements. It is biased towards the quenched face (Figure 6.1). The material data are summarized in Appendix A. The simulation includes nonlinear material properties as well as latent heat of phase transformation.

The main purpose of this calculation is to validate the data for the transformation kinetics. To this end the resulting martensite distribution is compared to the experimental results from the same source as the CCT data on which the kinetic parameters are based (Wever and Rose, 1961). This is shown in Figure 6.2. The agreement is satisfactory. The steady lowering of the hardness between 20 and 50 mm is mainly due to presence of bainite in the actual results. Bainite transformation is not included in the calculation model. The temperature history

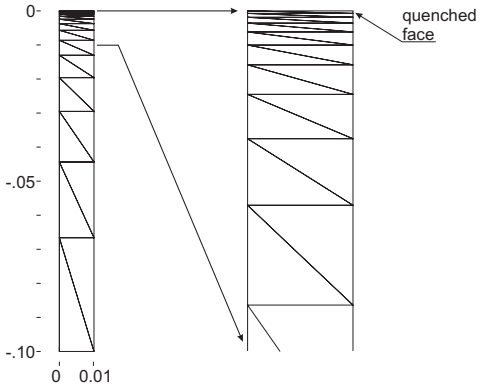

Figure 6.1: Element model for simulation of the Jominy test.

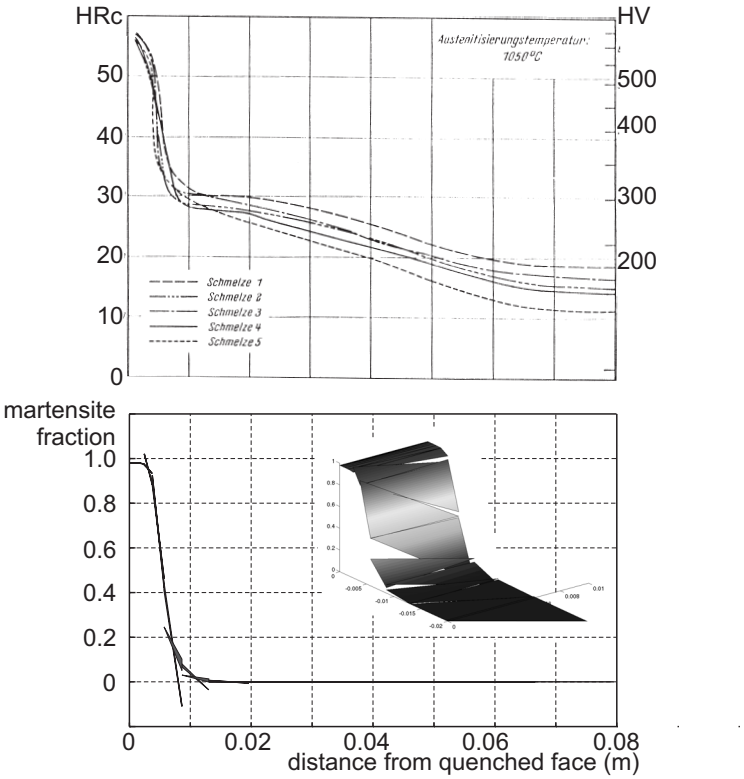

Figure 6.2: Finite element results compared to data from Wever and Rose (1961).

for two points and one phase fraction history are shown in Figure 6.3. The irregularities in the cooling due to release of latent heat are clearly visible.

For cooling down from 1050°C to room temperature 1900 seconds are required. The total analysis took 173 time steps which needed an average of 5 iterations to obtain an accuracy of 0.001 of $\Delta\mathbf{q}$. The initial time step was 0.1 s. When during one step less than 4 iterations were needed the step length for the next time step was increased. When more than 7 iterations were needed, the time step length was shortened. In general, quadratic convergence was observed. However, when the ferrite/pearlite transformation starts locally while the time step is too large the rate of convergence drops to first order.

6.1.2 transformation induced plasticity

The inclusion of transformation plasticity in stress calculations of transformation hardening is known to have a considerable influence on the final results (Abbasi and Fletcher, 1985; Denis and Simon, 1986). In the calculations of this section the model of transformation plasticity is validated. A constant value of $\nabla\cdot\mathbf{q}$ is prescribed to simulate continuous cooling. Monitoring of the strain gives a so called dilatometer curve (Figure 6.4). The occurrence of phase transformations is apparent from the deviation from regular linear thermal expansion.

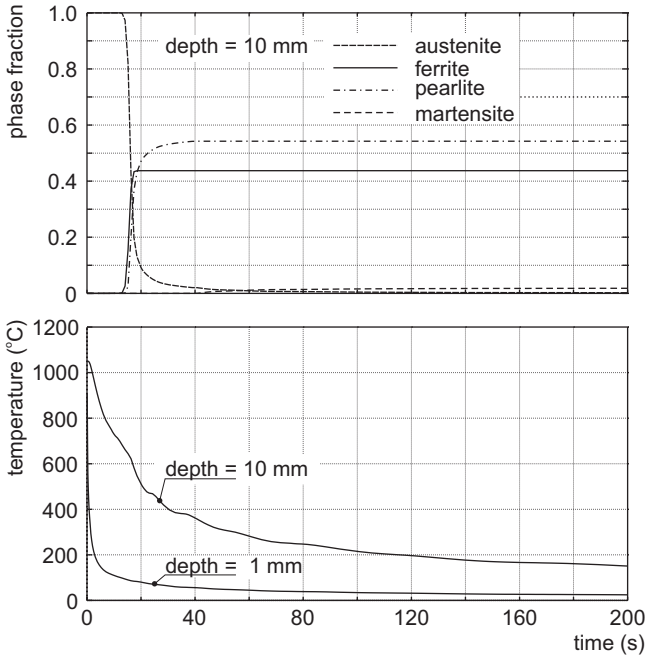

Figure 6.3: Temperature history at depths of 1 and 10 mm and phase fraction evolution at 10 mm from the quenched face.

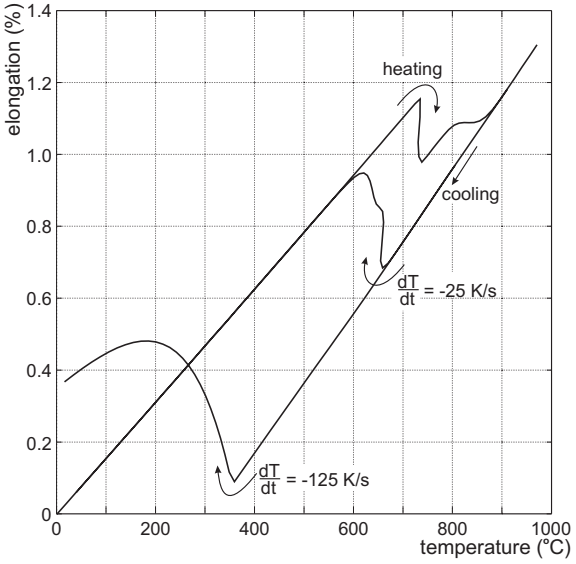

Figure 6.4: Dilatometer curves for different quench rates.

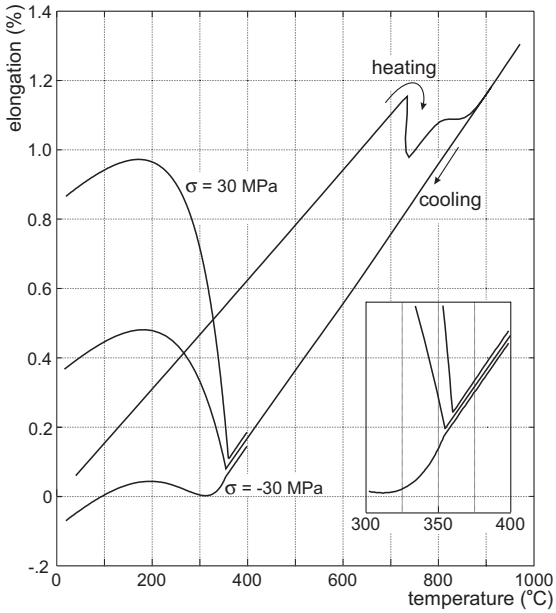

Figure 6.5: Dilatometer curves with applied uniaxial stress. Transformation plasticity and modification of the kinetics during the martensite transformation.

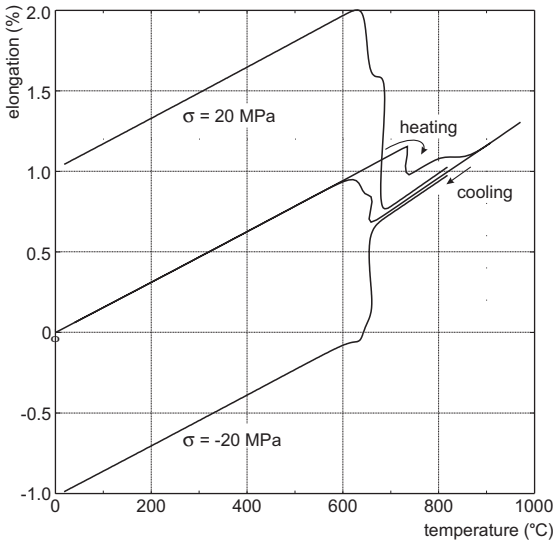

Figure 6.6: Dilatometer curves with applied uniaxial stress. Transformation plasticity and modification of the kinetics during the pearlite transformation.

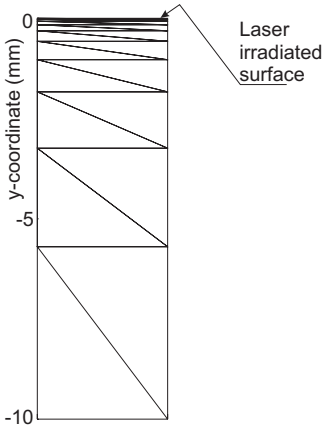

Figure 6.7: One-dimensional model of laser hardening.

When this test is repeated with an applied external stress, two phenomena are observed: modification of the kinetics and transformation plasticity. Both effects are shown for the martensite transformation in Figure 6.5 and for the pearlitic transformation in Figure 6.6.

For the martensitic transformation the M_s temperature which at zero stress is 355 °C shifts to 360 °C for applied tensile stress of 30 MPa. The data, which are summarized in Appendix A, are such that a similar compressive stress does not noticeably alter the M_s temperature.

A similar phenomenon is visible in the simulation of the pearlite transformation (Figure 6.6). Apart from the transformation plasticity a slight rise in the temperature at which the transformation starts can be seen in the curve with the tensile stress. The data are such that hardly any change occurs when a compressive stress is applied.

6.2 Laser hardening

6.2.1 1-D model

The simplest model of laser hardening is a one-dimensional model (Figure 6.7). A prescribed heat input of 25 MW/m^2 is applied during 0.6 seconds to one side of a 10 mm thick slab. For cooling after the laser pulse has been stopped, both on the bottom and at the top of the slab, convective heat transfer to the environment is modelled with a transfer coefficient γ = 100 W/m^{2}K. To mimic extension of the model in the lateral direction, the side faces of the model are thermally isolated. For structural calculations the side faces are constrained to remain straight.

Two simulations, one with and one without influence of stress on phase transformation are done. The results of the simulation without stress influence are taken as the reference.

In Figure 6.8 the temperature evolution of the top face is shown, together with the phase fraction evolution. Notice the transformation behaviour at 1 mm depth. Although a temperature above A_3 is reached, not all ferrite transforms to austenite. As a result, upon cooling already some austenite starts transforming back to ferrite even though the

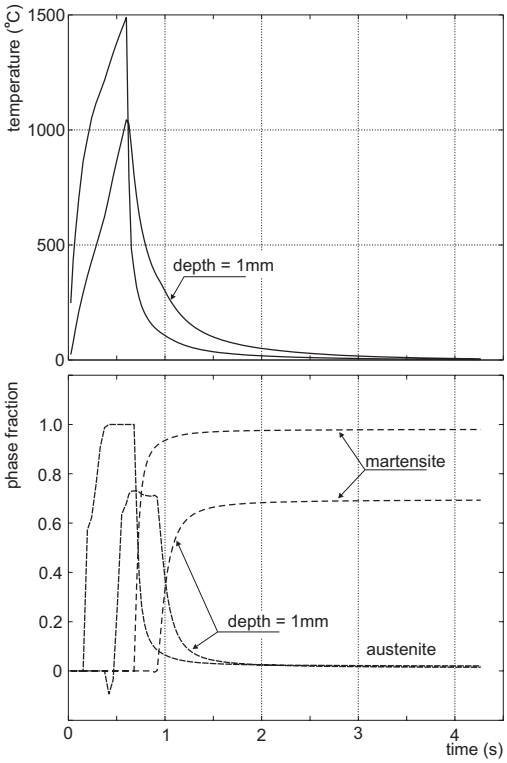

Figure 6.8: Temperature and phase fraction history at the irradiated face and at a depth of 1 mm below the surface.

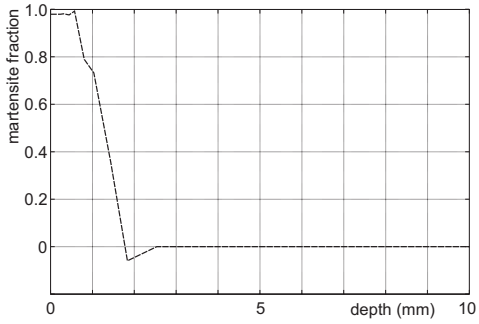

Figure 6.9: Martensite fraction through the thickness the sample.

cooling rate is far in excess of the critical cooling rate. The under-shoot at the start of the austenite transformation is caused by extrapolation from integration points, where the data are calculated, to nodal points. The fraction of martensite and the residual stress in the x-direction are shown as a function of depth below the surface in Figures 6.9 and 6.10.

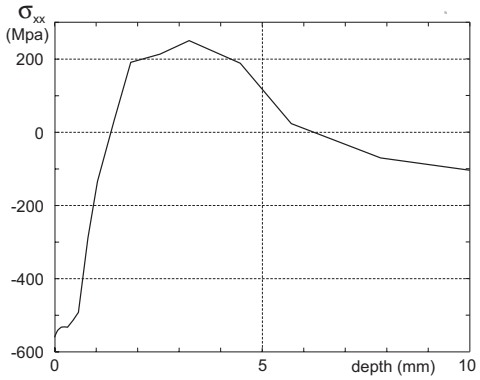

Figure 6.10: Residual stress σ_{xx} through the thickness of the sample.

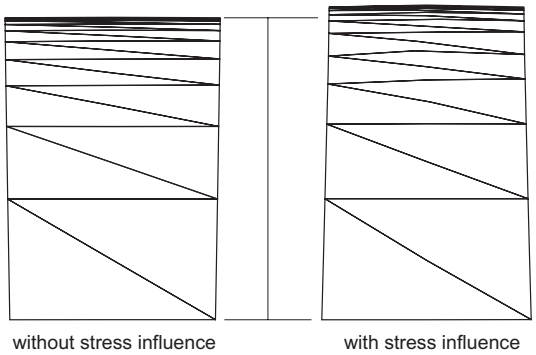

Figure 6.11: Residual distortion after laser processing, with and without stress influence (displacements scaled by a factor 20).

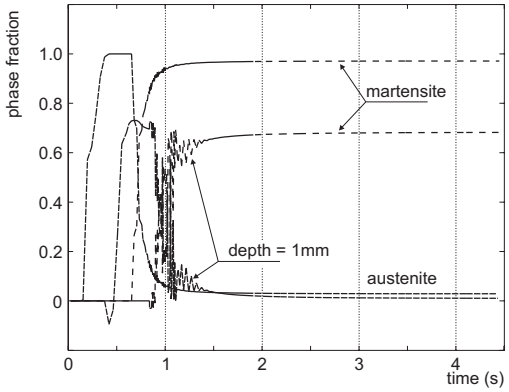

Figure 6.12: Phase fraction history with stress influence.

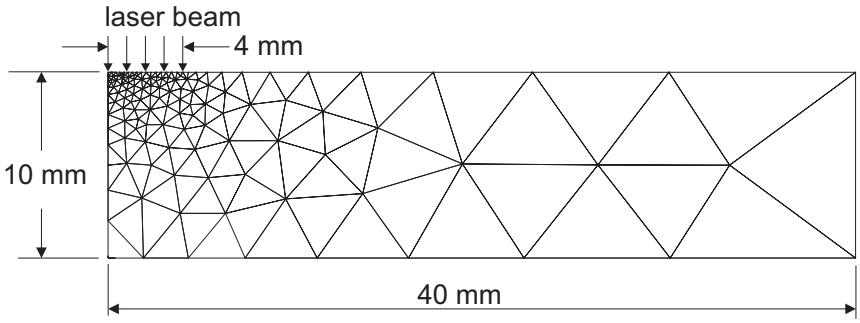

Figure 6.13: Two-dimensional model of laser hardening.

The results of the simulation with stress influence on the phase transformation are more or less similar to the above results apart from a marked difference in the final distortion. Without the stress influence the model predicts that the lasered face is convex; with stress influence a concave surface results (Figure 6.11).

In this simulation the stress influence was implemented such that the phase fraction increments were calculated with a constant stress during every time step equal to the initial stress of that step. The phase fraction history is shown in Figure 6.12. It is apparent that this implementation is rather unstable, which illustrates the necessity of properly implementing stress dependence along the lines of Chapter 4. This also raises doubts about the validity of the distortion results of Figure 6.11.

6.2.2 2-D model

The calculations of Section 6.2.1 are repeated using a two-dimensional model (Figure 6.13). The main difference is that now there is also a thermal gradient in the lateral direction. This results in a lower maximum temperature and an enhanced cooling rate after the laser irradiation has been stopped (Figure 6.14). In Figure 6.15 the deformation after totally cooling down is shown where the deformations are exaggerated by a factor 20. In Figure 6.16 a detail of the model is shown in which the extent of the martensitic region is indicated. The fraction of martensite and the residual stresses in the x- and z-directions on the centre line are shown as a function of depth below the surface in Figures 6.17 and 6.18.

6.2.3 comparison

Overall the temperatures in the 2-dimensional calculations are lower than in the 1-dimensional calculation. This can mainly be explained by the fact that in a 2-dimensional calculations a thermal gradient exists also in the lateral direction. The lower maximum temperature that is attained in the 2-D simulation obviously results in a lower hardening depth as compared to the 1-D results. This is shown in Figure 6.19. Less obvious is the difference in the level of the residual stress (Figure 6.20). An explanation may be that in the 2-D simulation the expansion accompanying the martensite transformation happens in a thinner layer while the bulk material is stiffer due to lower temperatures.

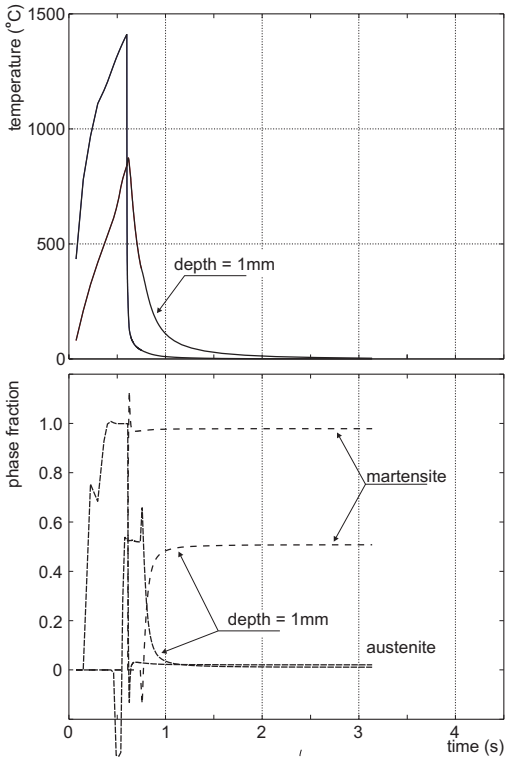

Figure 6.14: Temperature and phase fraction history at the irradiated face and at a depth of 1 mm below the surface.

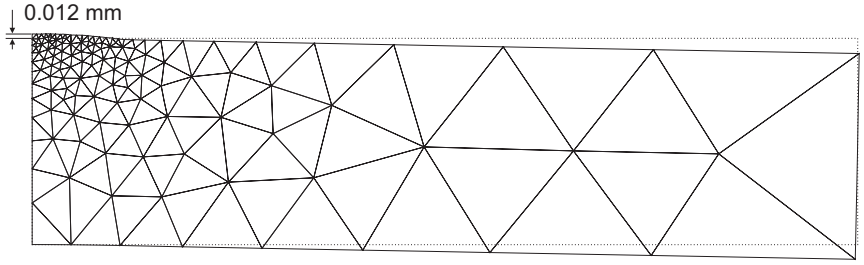

Figure 6.15: Deformation after cooling down (displacements scaled by a factor 20).

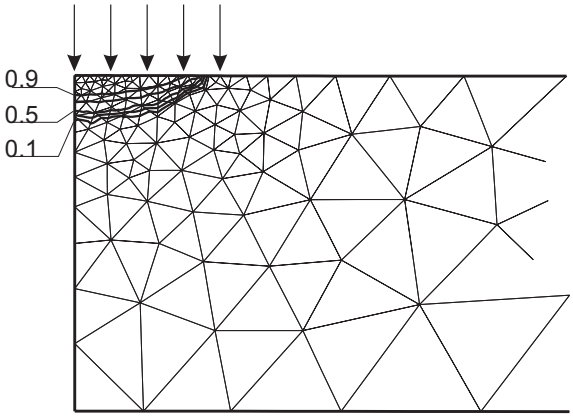

Figure 6.16: Martensite region after cooling down.

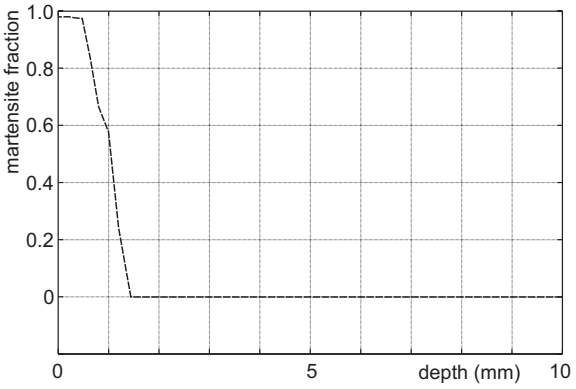

Figure 6.17: Martensite fraction through the thickness of the sample.

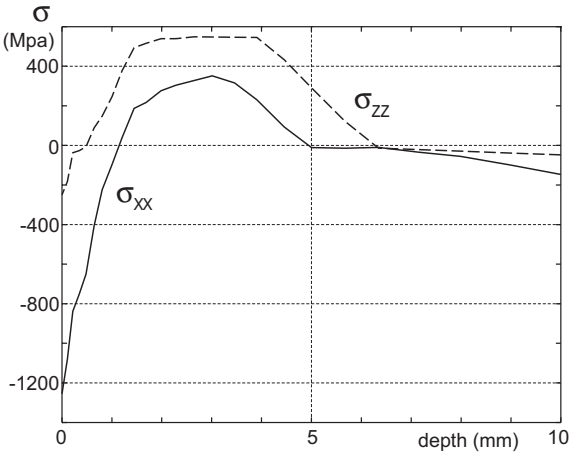

Figure 6.18: Residual stresses σ_{xx} and σ_{zz} through the thickness of the sample.

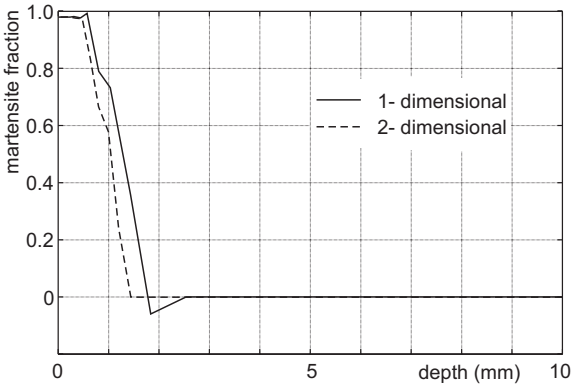

Figure 6.19: Martensite fraction through the thickness of the sample, comparison of 1-D and 2-D results.

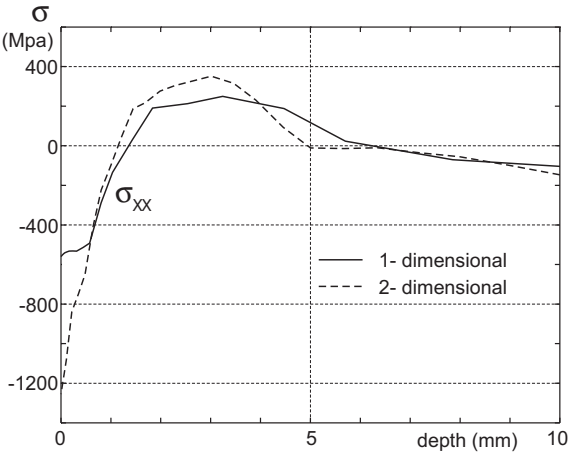

Figure 6.20: Residual stress σ_{xx} through the thickness of the sample, comparison of 1-D and 2-D results.

6.3 Conclusions

The finite element model of Chapter 5, using the constitutive equations from Chapter 4 was applied to simulations of laser hardening. Simulations of temperatures and phase fractions which involved phase transformation kinetics, latent heat of transformation, superheating of ferrite and supercooling of austenite, were performed. Good results were obtained while the convergence of the computations was satisfactory.

Simulations of stresses and distortions were carried out including thermal dilatation, dilatation due to phase change and transformation plasticity. Here also satisfactory results were obtained. When the stress influence on the transformations is included, without adapting the constitutive equations, the results showed some instability. This indicates that for inclusion of stress influence a consistent implementation is necessary. This has not yet been carried out but is recommended as future work. The high temperature plastic recovery has not been implemented either. The literature should be searched or tests should be carried out in order to obtain reliable material parameters for plastic recovery.

Comparison of the results obtained for one-dimensional and two-dimensional simulations shows considerable differences. This is mainly due to thermal diffusion in the lateral direction. One-dimensional calculations, although useful for parameter studies, should always be checked by two-dimensional or even three-dimensional simulations.

Part II

SIMULATION OF STEADY LASER HARDENING

7. Arbitrary Lagrangian Eulerian Method

7.1 Introduction

A straightforward Updated Lagrangian simulation of hardening with a scanning laser beam requires repositioning of the heat flow boundary conditions for every calculation time step to represent the movement of the heat source.

During and immediately after the passing of the laser source events happen in very rapid succession. In order to capture this highly localized behavior the path of the scanning laser must be paved with a very dense finite element mesh. A simulation performed in this way is very time consuming.

Different strategies have been devised to cope with this type of simulation. One of the most practical is the Arbitrary Lagrangian-Eulerian method (Liu *et al.*, 1988; Benson, 1989). In the implementation as proposed by Huétink (1986) and as used in this work, each calculation step is split into two phases. This is shown in Figure 7.1.

In the first phase, the Lagrangian phase, the element mesh remains attached to the material. The evolution of the state variables is monitored and the state at the end of the phase is calculated as explained in Chapter 5.

In the second phase, the Eulerian phase, the mesh is, broadly speaking, restored to its original position with respect to the window attached to the moving source. The mesh is not restored to its exact original position, but some allowance is made perpendicular to the flow direction in order to capture movement of the free surfaces.

The values of state variables such as temperatures, stresses, strains and phase fractions are now needed in the mesh at this new position. This update of state variables is expressed as a convection with respect to the mesh at the end of the first phase. In this chapter only the second phase is described. The Lagrangian first phase is identical to a transient calculation step as treated in Chapter 5.

When the coupling between mesh displacements and material displacements is released, two additions are needed to the Updated Lagrangian method:

- a strategy to calculate grid displacements, such that the mesh quality will remain acceptable in terms of element distortion and boundary compatibility. This is treated in Section 7.2;
- a method to make state variables available in the appropriate element integration points. These mesh points will move independently from the material. A mapping of the state variables is required, which can be cast in the form of a convection equation. The remapping procedures will be treated in Section 7.3.

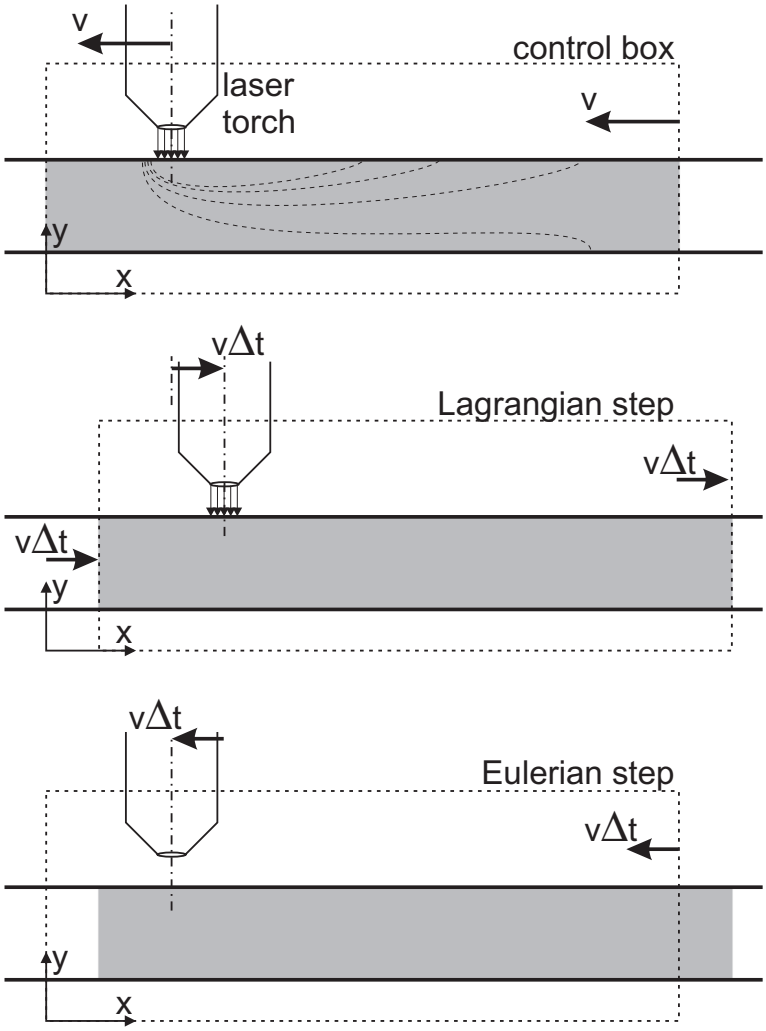

Figure 7.1: Arbitrary Lagrangian Eulerian modeling of laser hardening.

The purpose of defining a separate velocity field for the grid is usually to prevent unacceptable distortion of the element mesh. In our case the objective is to supply small enough elements in the processing zone while being able to coarsen the mesh downstream.

7.1.1 implementation of the ALE method

Several different strategies to the implementation of the Arbitrary Lagrangian-Eulerian method can be followed:

Coupled ALE Solve a coupled system which includes the material displacements and the

grid displacements simultaneously. A consistent implementation requires that the convective terms coming from the remap are also incorporated into the constitutive equations.

Decoupled ALE First, solve the Updated Lagrangian step until convergence is reached. Next, calculate the grid displacements and perform the remap of the state variables (Stoker, 1999).

Semi-coupled ALE Perform iterations comprising a Lagrangian step, followed by the repositioning of the grid and the remap. The remap is carried out at each iteration (Wisselink, 2000).

Each of these strategies has its own advantages and drawbacks. In the Coupled strategy consistently linearized equations are solved, the Newton-Raphson iterations will have good convergence. The number of unknowns in the system is doubled ($\mathbf{u}_m$ and $\mathbf{u}_g$ in Figure 7.2) which more than doubles the computational effort.
In the Decoupled strategy iterations are also performed with a consistent system matrix but now only for the material displacements. The consistency of the state variable field is lost after the remap.
By carrying out a remap during every iteration the resulting state variable field will remain consistent in the Semi-coupled strategy, but now the iteration process is no longer consistent, possibly resulting in slow convergence.
In this thesis the Decoupled strategy is used, mainly because it is the most easily implemented.

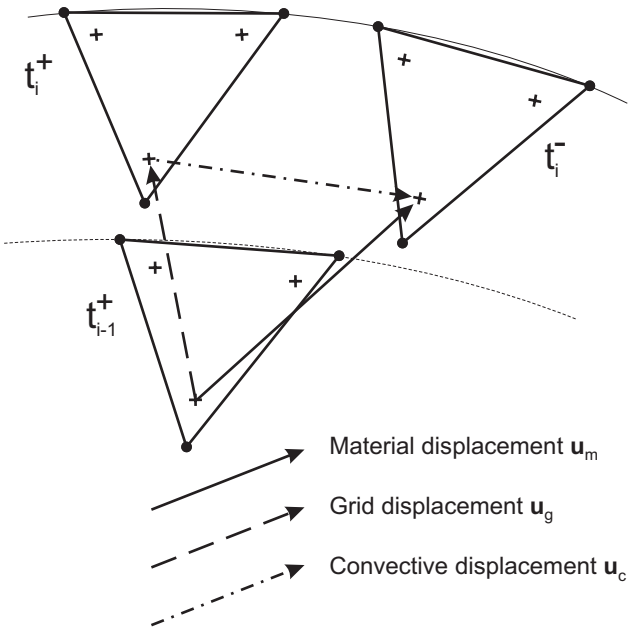

Figure 7.2: An Arbitrary Lagrangian Eulerian step, t^-, before and t^+ after mesh regularization.

7.2 Mesh management

Here we adopt the method developed by Stoker (1999). Rather than calculating the new locations of the mesh, the grid displacements are smoothened. The grid displacement $\mathbf{u}_g$ is calculated with the objective if reducing mesh distortion. To this end it is required to obey the Laplace equation:

$$\nabla^2 \mathbf{u}_g = \mathbf{0} \tag{7.1}$$

This equation tends to smoothen steep gradients in the grid displacement. The boundary conditions are such that the mesh boundary follows the material free surface as is described in Section 7.2.1. Since it is the velocity that is smoothened, an initial mesh refinement will be largely conserved. A drawback is that the quality of the grid locations proper is not guaranteed.

The implementation of Equation (7.1) can be achieved through a Galerkin discretization. It is more economical, however, to use a node by node centering method, where in a number of sweeps over all the nodes the grid displacement of each node is calculated as the average of the grid displacements of its neighbours (Stoker, 1999).

7.2.1 free surface movement

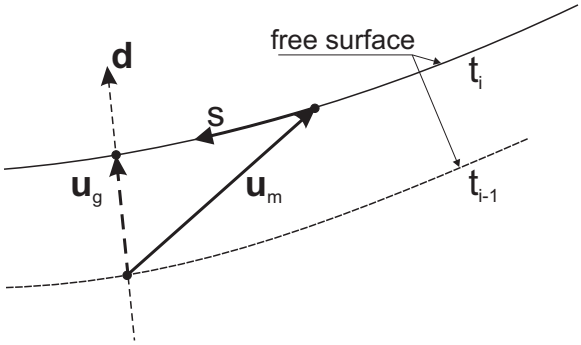

Figure 7.3: Grid displacement of a free surface node.

The grid displacements which are required for the grid to follow the free surface movements serve as boundary conditions to (7.1). The mesh is restricted in its movement perpendicular to the flow direction. Therefore in each free surface node a direction vector **d** is defined to which the grid movement is constrained. This is shown in Figure 7.3. The grid displacement is constrained to be along **d**.

$$\mathbf{u}_g = \lambda \mathbf{d} \tag{7.2}$$

In the setup of Figure 7.1 an obvious choice for **d** would be the y-direction base vector.

The parameter λ is solved such that the node ends up exactly on the parametrized free surface. Quadratic elements are used, so the surface is described by piece-wise quadratic

parameterizations. The solution of λ requires an iterative procedure in which λ is solved simultaneously with a parameter s, which locally determines the position along the free surface line.

At the inflow and outflow boundaries no free surfaces exist. Here the grid displacement is simply found as the projection of $\mathbf{u}_\mathrm{m}$ on $\mathbf{d}$, see Figure 7.4:

$$\mathbf{u}_\mathrm{g} = \frac{\mathbf{dd}}{|\mathbf{d}|^2} \cdot \mathbf{u}_\mathrm{m} \tag{7.3}$$

A choice for $\mathbf{d}$ could be along the tangent to the current position of the outflow (or inflow) surface.

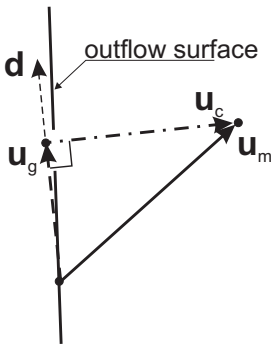

Figure 7.4: Grid displacement of an outflow surface node.

7.3 Remap of state variables

We direct our attention to an integration point of the element in its final position as shown in Figure 7.2. Our ambition is now to find at this point the value of any state variable $f(\mathbf{x}, t_i^+)$, based on its value $f(\mathbf{x}, t_i^-)$ at the end of the Lagrangian step, where f stands for temperature, stress component, equivalent plastic strain or any other state variable.

As indicated in Figure 7.2 the material undergoes a displacement $\mathbf{u}_\mathrm{m}(\mathbf{x})$, whereas the mesh moves independently with a displacement $\mathbf{u}_\mathrm{g}(\mathbf{x})$. The difference between the material displacement and the grid displacement is called the convective displacement $\mathbf{u}_\mathrm{c}(\mathbf{x}) = \mathbf{u}_\mathrm{m} - \mathbf{u}_\mathrm{g}$. When $\mathbf{u}_\mathrm{c}$ is small, then the value of $f(\mathbf{x}, t_i^+)$, can be approximated by a first order Taylor series expansion:

$$f(\mathbf{x}, t_i^+) = f(\mathbf{x} - \mathbf{u}_\mathrm{c}, t_i^-) = f(\mathbf{x}, t_i^-) - \mathbf{u}_\mathrm{c} \cdot \nabla f(\mathbf{x}, t_i^-) + \mathrm{O}(\mathbf{u}_\mathrm{c}^2) \tag{7.4}$$

The main difficulty when using (7.4) to calculate the convected values of the state variables is, that these do not constitute a continuous field. Stresses and strains are only evaluated at the integration points and are discontinuous over element boundaries. This also means that the gradients of the state variables cannot be obtained from local differentiation, since this disregards the jumps across the element boundaries. Therefore information about values in neighbouring elements is required to construct a global gradient.

Many methods for obtaining the values of the state variables $f(\mathbf{x}, t_i^+)$ have been published. The method originally developed by Huétink (1986) (Huétink *et al.*, 1990b) requires the construction of a continuous field based on nodal averaging. In Boman and Ponthot (2001) this is circumvented by defining a subgrid with the integration points as vertices. A class of methods which do not require a continuous field, are the finite volume methods. Huerta *et al.* (1995) and Rodriguez-Ferran *et al.* (2002) use the Godunov method on a sub-grid of finite volumes, where each volume contains one integration point.

In Section 7.3.2 a similar method is developed, however, this does not rely on a sub grid but directly uses the existing mesh. The proposed method is based on the *Discontinuous Galerkin* method, which is a generalization of the finite volume method. First, the discontinuous Galerkin method is introduced. Next, an extension based on a second order Taylor expansion is shown which yields a far better accuracy at minimal additional costs.

In the ALE method there is no time scale involved with the convection of the data. Both t_i^- and t_i^+ represent the same instant in time. In order to comply with the standard treatment of convection an artificial time parameter τ is introduced, which maps the "interval" $[t_i^-, t_i^+]$ onto $[0, \Delta t]$. Likewise, a convective velocity $\mathbf{v}_c = \mathbf{u}_c/\Delta t$ is defined.

7.3.1 the discontinuous Galerkin method for convection

The choice for the discontinuous Galerkin method is attractive because it does not require a continuous field for the discretization of the convection. Moreover, the result after convection will again be discontinuous, which is in aggreement with the finite element theory. The Discontinuous Galerkin method was introduced by Lesaint and Raviart (1974) and is often used for computation of viscoelastic flow (Fortin and Fortin, 1989; Verbeeten *et al.*, 1998; Pichelin and Coupez, 1998) and compressible aerodynamic flow (Lomtev and Karniadakis, 1999; Baumann and Oden, 2000; Cockburn, 2001). Most convection schemes using the Discontinuous Galerkin method are discretizations of the rate equation for transient convection:

$$\frac{\partial f}{\partial t} = -\mathbf{v}_c \cdot \nabla f \tag{7.5}$$

Here $f(\mathbf{x}, t)$ stands for any element variable, typically evaluated at the integration points, $\mathbf{v}_c$ is the convective velocity. The increment for finite time steps is then obtained by time integration:

$$\Delta f = \int_0^{\Delta t} \frac{\partial f}{\partial t}\, \mathrm{d}t \tag{7.6}$$

For accuracy high order time integration is used, e.g. a Taylor Galerkin approach by Pichelin and Coupez (1998) or 2nd or 3rd order Runge-Kutta by Cockburn (2001). For stability and monotonicity, limiters are frequently employed (Siegel *et al.*, 1997; Cockburn, 2001). Limiting procedures are (often a posteriori) non-linear operations, which have to be applied to every separate variable. In our case we prefer an explicit method which needs no limiting and which can be applied to all variables equally. The method of Section 7.3.2 fulfills this requirement. This section serves to explain the general ideas of the discontinuous Galerkin method applied to convection.

one-dimensional convection

The discontinuous Galerkin Method will first be demonstrated on the one-dimensional convection equation. Generalization to the multi-dimensional case is shown in Section 7.3.4.

We want to solve $f(x,\tau)$, ($x \in [0, L]$; $\tau \in [0, \Delta t]$), such that:

$$\begin{aligned} \frac{\partial f}{\partial \tau} + v_c \frac{\partial f}{\partial x} &= 0 \\ f(0,\tau) = f_0 \text{ and } f(x,0) &= f(x, t_i^-) \end{aligned} \tag{7.7}$$

In particular we are interested in the convective increment which is given by (7.4) as:

$$\Delta f(x) = f(x, t_i^+) - f(x, t_i^-) \approx -u_c \frac{\partial f}{\partial x} \tag{7.8}$$

The weak form is obtained by multiplication with a test function $w(x)$ and integration over $[0, L]$:

$$\int_0^L w \Delta f \, \mathrm{d}x = -\int_0^L w u_c \frac{\partial f}{\partial x} \, \mathrm{d}x \quad \forall w \tag{7.9}$$

After partial integration a global conservation equation is obtained with flux terms at the boundaries $x = 0$ and $x = L$:

$$\int_0^L w \Delta f \, \mathrm{d}x = \int_0^L \frac{\partial (w u_c)}{\partial x} f \, \mathrm{d}x + w u_c f|_{x=0} - w u_c f|_{x=L} \tag{7.10}$$

Now f_0 is substituted for f at $x = 0$. When the partial integration is reversed the following expression is obtained:

$$\int_0^L w(\Delta f + u_c \frac{\partial f}{\partial x}) \, \mathrm{d}x + w u_c (f - f_0)|_{x=0} = 0 \quad \forall w \tag{7.11}$$

This is the weak form equivalent to:

$$\begin{aligned} \Delta f + u_c \frac{\partial f}{\partial x} &= 0 \qquad \text{for } x \in [0, L] \\ f &= f_0 \qquad \text{for } x = 0 \end{aligned} \tag{7.12}$$

The spatial domain $[0, L]$ is partitioned into N_x intervals $I_n = [x_{n-1}, x_n]$, where $n \in [1, N_x]$. The field f as well as the increment Δf are discretized on I_n using discontinuous base functions $w_n(x)$ (Figure 7.5):

$$\begin{aligned} f_h^n(x,\tau) &= \sum_k w_n^k(x) \, f_k^n(\tau) \\ \Delta f_h^n(x) &= \sum_k w_n^k(x) \Delta f_k^n \end{aligned} \tag{7.13}$$

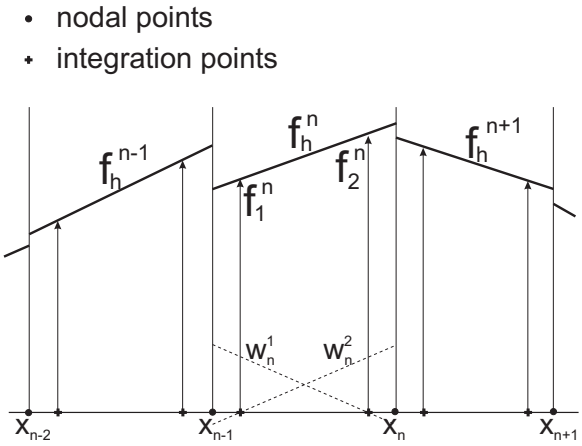

Figure 7.5: Discontinuous function discretization on I_n.

Since the f_h-field is assumed to be discontinuous across interval boundaries direct application of (7.9) is not appropriate. The discretized solution in element I_n should satisfy:

$$\begin{aligned} \Delta f_\mathrm{h}^n &= -u_\mathrm{c}\frac{\partial f_\mathrm{h}^n}{\partial x} \\ f_\mathrm{h}^n(x_{n-1}) &= f_\mathrm{h}^{n-1}(x_{n-1}) \end{aligned} \tag{7.14}$$

We follow Lesaint and Raviart (1974) and weakly enforce both the differential equation on I_n and the continuity of f_h at the upstream boundary x_{n-1}. Find Δf_h^n such that:

$$\int_{I_n} \Delta f_\mathrm{h}^n w_n^k \,\mathrm{d}x = -\int_{I_n} u_\mathrm{c}(x)\frac{\partial f_\mathrm{h}^n}{\partial x} w_n^k \,\mathrm{d}x - u_\mathrm{c} w_n^k (f_\mathrm{h}^n - f_\mathrm{h}^{n-1})\Big|_{x=x_{n-1}} \quad \forall w_n^k \tag{7.15}$$

After partial integration the jump term at the inflow boundary splits up into two flux terms, an in-flux from the upwind element and an out-flux at the outflow boundary:

$$\int_{I_n} \Delta f_\mathrm{h}^n w_n^k \,\mathrm{d}x = \int_{I_n} \frac{\mathrm{d}(u_\mathrm{c} w_n^k)}{\mathrm{d}x} f_\mathrm{h}^n \,\mathrm{d}x + u_\mathrm{c} w_n^k f_\mathrm{h}^{n-1}\Big|_{x=x_{n-1}} - u_\mathrm{c} w_n^k f_\mathrm{h}^n\Big|_{x=x_n} \quad \forall w_n^k \tag{7.16}$$

When a discretization using piece-wise constant functions is applied then the integral on the right hand side will vanish. What remains then is an equation stating that the increment is the balance of the fluxes across the inflow and outflow boundaries.

The main attraction of the discontinuous Galerkin method is apparent from the left hand side of (7.16). The support of w_n^k is restricted exclusively to interval I_n. There is no coupling with unknowns in other intervals and the resulting matrix is local. Moreover, when Δf is discretized using orthogonal polynomials the equations are uncoupled, the resulting matrix is diagonal and solution is trivial. This is also true for linear interpolation per element, based on function values in Gauss integration points as in Figure 7.5. Coupling with other intervals is only through the boundary fluxes of *known* values $f_\mathrm{h}^{n-1}(t_i^-)$. The solution of Δf_h^n can be done on an element by element basis.

The accurate and stable solution of Δf using this method requires a Runge-Kutta time integration where the optimal order of the integration is linked to the order of the interpolation functions w_n^k (Hulsen, 1991). An alternative method was presented by Siegel *et al.* (1997) in which first a convection over half the step was performed using only local f_h values, i.e. Equation (7.15) without the inflow boundary jump term. Next, the whole convection step was calculated according to (7.16) with the values obtained from the first half step. In the following section a method is developed which gives a similar result in one pass.

7.3.2 the second order discontinuous Galerkin method

In order to derive a higher order accurate discontinuous Galerkin method consider a so-called space-time slab $[0, L] \times [t_i^-, t_i^+]$ (Figure 7.6). Equation (7.7) is written in a weak form over the space×time region:

$$\int_{t_i^-}^{t_i^+} \int_0^L w \left(\frac{\partial f}{\partial \tau} + v_\mathrm{c} \frac{\partial f}{\partial x} \right) \mathrm{d}x \, \mathrm{d}\tau = 0 \qquad \forall w \tag{7.17}$$

where $w(x)$ is a weighting function which only depends on x. Partial integration yields the following balance equation:

$$\int_0^L w(f(x, t_i^+) - f(x, t_i^-)) \, \mathrm{d}x = \int_0^L \frac{\mathrm{d}v_\mathrm{c} w}{\mathrm{d}x} \int_{t_i^-}^{t_i^+} f \, \mathrm{d}\tau \, \mathrm{d}x + \int_{t_i^-}^{t_i^+} v_\mathrm{c} w f_0 \, \mathrm{d}\tau \Big|_{x=0} - \int_{t_i^-}^{t_i^+} v_\mathrm{c} w f \, \mathrm{d}\tau \Big|_{x=L} \tag{7.18}$$

Using (7.7), the evolution of f as a function of τ is written as (Donea, 1984):

$$f(x, \tau) \approx f(x, t_i^-) + \frac{\partial f}{\partial \tau} \tau = f(x, t_i^-) - v_\mathrm{c} \frac{\partial f}{\partial x} \tau \tag{7.19}$$

After substitution of this expression into (7.18) and using $u_\mathrm{c} = v_\mathrm{c} \Delta t$ we find:

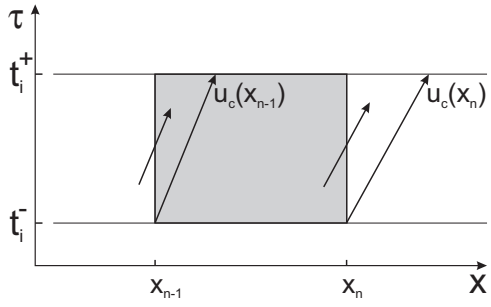

Figure 7.6: A convective step, in space-time; t^-, before and t^+ after mesh regularization.

$$\int_0^L w\Delta f \,\mathrm{d}x = \int_0^L \frac{\mathrm{d}(wu_\mathrm{c})}{\mathrm{d}x}\left(f - \frac{1}{2}u_\mathrm{c}\frac{\partial f}{\partial x}\right)\mathrm{d}x + wu_\mathrm{c}\, f_0|_{x=0} - wu_\mathrm{c}\left(f - \frac{1}{2}u_\mathrm{c}\frac{\partial f}{\partial x}\right)\Big|_{x=L} \tag{7.20}$$

where all values and gradients of f are evaluated at $t = t^-$. Reversing the partial integration yields:

$$\int_0^L w\left(\Delta f + u_\mathrm{c}\frac{\partial f}{\partial x} - \frac{1}{2}u_\mathrm{c}^2\frac{\partial^2 f}{\partial x^2}\right)\mathrm{d}x + wu_\mathrm{c}\left(f - \frac{1}{2}u_\mathrm{c}\frac{\partial f}{\partial x} - f_0\right)\Big|_{x=0} = 0 \tag{7.21}$$

The first term expresses the increment as a second order Taylor expansion. The second term is the weakly enforced boundary condition at $x = 0$. The expression obtained is the weak statement of:

$$\begin{aligned} \Delta f(x) + u_\mathrm{c}\frac{\partial f}{\partial x} - \frac{1}{2}u_\mathrm{c}^2\frac{\partial^2 f}{\partial x^2} = 0 \qquad & \text{for } x \in [0, L] \\ f - \frac{1}{2}u_\mathrm{c}\frac{\partial f}{\partial x} = f_0 \qquad & \text{for } x = x_0 \end{aligned} \tag{7.22}$$

Similar approximations for conservation type equations have been derived by Oñate (1998) and de Sampaio and Coutinho (2001) in the context of continuous Galerkin methods. Inspired by this result the discretized field on element I_n is required to satisfy:

$$\begin{aligned} \Delta f_\mathrm{h}^n &= -u_\mathrm{c}\frac{\partial f_\mathrm{h}^n}{\partial x} + \frac{1}{2}u_\mathrm{c}^2\frac{\partial^2 f_\mathrm{h}^n}{\partial x^2} \\ \left(f_\mathrm{h}^n - \frac{1}{2}u_\mathrm{c}\frac{\partial f_\mathrm{h}^n}{\partial x}\right)\Big|_{x=x_{n-1}} &= \left(f_\mathrm{h}^{n-1} - \frac{1}{2}u_\mathrm{c}\frac{\partial f_\mathrm{h}^{n-1}}{\partial x}\right)\Big|_{x=x_{n-1}} \end{aligned} \tag{7.23}$$

This is written in a weak form:

$$\int_{I_n} \Delta f_\mathrm{h}^n w_n^k \,\mathrm{d}x = -\int_{I_n}\left(u_\mathrm{c}\frac{\partial f_\mathrm{h}^n}{\partial x} - \frac{1}{2}u_\mathrm{c}^2\frac{\partial^2 f_\mathrm{h}^n}{\partial x^2}\right)w_n^k \,\mathrm{d}x - u_\mathrm{c}w_n^k\left((f_\mathrm{h}^n - \frac{1}{2}u_\mathrm{c}\frac{\partial f_\mathrm{h}^n}{\partial x}) - (f_\mathrm{h}^{n-1} - \frac{1}{2}u_\mathrm{c}\frac{\partial f_\mathrm{h}^{n-1}}{\partial x})\right)\Big|_{x=x_{n-1}} \quad \forall w_n^k \tag{7.24}$$

After partial integration the jump term at the inflow boundary splits up into two flux terms, an in-flux from the upwind element and an out-flux at the outflow boundary:

$$\int_{I_n} \Delta f_\mathrm{h}^n w_n^k \,\mathrm{d}x = \int_{I_n}\left(\frac{\mathrm{d}(u_\mathrm{c}w_n^k)}{\mathrm{d}x}f_\mathrm{h}^n - \frac{1}{2}\frac{\mathrm{d}(u_\mathrm{c}^2 w_n^k)}{\mathrm{d}x}\frac{\partial f_\mathrm{h}^n}{\partial x}\right)\mathrm{d}x + u_\mathrm{c}w_n^k\left(f_\mathrm{h}^{n-1} - \frac{1}{2}u_\mathrm{c}\frac{\partial f_\mathrm{h}^{n-1}}{\partial x}\right)\Big|_{x=x_{n-1}} - u_\mathrm{c}w_n^k\left(f_\mathrm{h}^n - \frac{1}{2}u_\mathrm{c}\frac{\partial f_\mathrm{h}^n}{\partial x}\right)\Big|_{x=x_n} \quad \forall w_n^k \tag{7.25}$$

The left hand side is identical to that of (7.16). The right hand side involves only known values and gradients of $f_{\mathrm{h}}^{n-1}(t_i^-)$ and $f_{\mathrm{h}}^{n}(t_i^-)$ so that explicit element by element solution remains possible. The explicit procedure of Equation (7.25) is equivalent to the result of the two pass procedure of Siegel *et al.* (1997).

The improved stability with respect to the scheme of Equation (7.16) stems from the second order boundary fluxes as well as from a naturally arising diffusion like term $(1/2)u_{\mathrm{c}}^2(\partial^2 f/\partial x^2)$. In 2-D or 3-D this term takes the form of stream-line diffusion.

7.3.3 element-wise point-implicit scheme

The scheme of (7.25) is stable for Courant numbers (Cr) < 0.7 (Figure 7.10). For many applications this is already sufficient. To extend the stability region we follow Baumann and Oden (2000) and apply an element-wise point-implicit scheme. To this end implicit terms (marked with α and β) are added to selected terms coming from weight functions, whose support is the domain of one element, with respect to the degrees of freedom associated with that same element:

$$\begin{aligned}\int_{I_n} \Delta f_{\mathrm{h}}^n w_n^k \,\mathrm{d}x = \\ \int_{I_n} \left(\frac{\mathrm{d}(u_{\mathrm{c}} w_n^k)}{\mathrm{d}x}(f_{\mathrm{h}}^n + \alpha \Delta f_{\mathrm{h}}^n) - \frac{1}{2}\frac{\mathrm{d}(u_{\mathrm{c}}^2 w_n^k)}{\mathrm{d}x}\frac{\partial(f_{\mathrm{h}}^n + \beta \Delta f_{\mathrm{h}}^n)}{\partial x} \right) \mathrm{d}x \\ + u_{\mathrm{c}} w_n^k \left(f_{\mathrm{h}}^{n-1} - \frac{1}{2}u_{\mathrm{c}}\frac{\partial f_{\mathrm{h}}^{n-1}}{\partial x} \right)\Bigg|_{x=x_{n-1}} - u_{\mathrm{c}} w_n^k \left(f_{\mathrm{h}}^{n} - \frac{1}{2}u_{\mathrm{c}}\frac{\partial f_{\mathrm{h}}^{n}}{\partial x} \right)\Bigg|_{x=x_{n}} \end{aligned} \tag{7.26}$$

Note that the implicit terms are only added to the terms in the integral. Adding these terms to the f_{h}^n terms at the outflow boundary x_n, as was proposed by Baumann and Oden (2000) will make the method non-conservative. When this is remedied by also adding implicit terms to the f_{h}^{n-1} terms at the inflow boundary, again a conservative method is obtained, but then the local character is lost.

Numerical experiments indicate that $\alpha = -1/60$ and $\beta = 2/3$ is a good choice. A priori it may be expected that the β-term will have a stabilizing effect. This term adds an additional (streamline) diffusion within each element. A small negative value for α seems to prevent the system from becoming over-damped.

After collecting all terms with Δf in the left hand side, the resulting matrix is no longer diagonal nor symmetric; however, it still remains local. The explicit element by element solution is still possible.

7.3.4 multi-dimensional convection

In two (or three) dimensions (7.22) is written as

$$\Delta f = -\mathbf{u}_{\mathrm{c}} \cdot \nabla f + \tfrac{1}{2}\mathbf{u}_{\mathrm{c}}\mathbf{u}_{\mathrm{c}} : \nabla\nabla f + O(\mathbf{u}_{\mathrm{c}}^3) \tag{7.27}$$

The second order term in the right hand side has the character of stream-line diffusion. The domain is divided into non-overlapping triangles on which f and Δf are discretized similar

to Equation (7.13). Equation (7.27) is written in the weak form while weakly enforcing continuity over the inflow boundary to obtain the counterpart of (7.24):

$$\int_{V_n} w_n^k \Delta f_{\mathrm{h}}^n \,\mathrm{d}V = -\int_{V_n} w_n^k \,\mathbf{u}_{\mathrm{c}} \cdot (\nabla f_{\mathrm{h}}^n - \tfrac{1}{2}(\nabla\nabla f_{\mathrm{h}}^n) \cdot \mathbf{u}_{\mathrm{c}}) \,\mathrm{d}V + \int_{\Gamma_n^-} w_n^k \,\mathbf{u}_{\mathrm{c}} \cdot \mathbf{n} \left(f_{\mathrm{h}}^n - f_{\mathrm{h}}^{n(-)} - \tfrac{1}{2}\mathbf{u}_{\mathrm{c}} \cdot (\nabla f_{\mathrm{h}}^n - \nabla f_{\mathrm{h}}^{n(-)}) \right) \mathrm{d}\Gamma \qquad \forall w_n^k \quad (7.28)$$

Here Γ_n^- is defined as that part of the boundary of the n^{th} element where $\mathbf{u}_{\mathrm{c}} \cdot \mathbf{n} < 0$, where $\mathbf{n}$ is the outward pointing normal on the element boundary. $f_{\mathrm{h}}^{n(-)}$ Is the value of f in the elements which share boundaries Γ_n^- with the n^{th} element, the upwind elements.

After partial integration the terms with α and β are added like in Eq. (7.26) and all terms containing Δf are collected on the left hand side:

$$\begin{aligned}\int_{V_n} \left(w_n^k \Delta f_{\mathrm{h}}^n - \alpha \nabla \cdot (w_n^k \mathbf{u}_{\mathrm{c}}) \Delta f_{\mathrm{h}}^n + \tfrac{1}{2}\beta \nabla \cdot (w_n^k \mathbf{u}_{\mathrm{c}} \mathbf{u}_{\mathrm{c}}) \cdot \nabla \Delta f_{\mathrm{h}}^n \right) \mathrm{d}V = \\ \int_{V_n} \left(\nabla \cdot (w_n^k \mathbf{u}_{\mathrm{c}}) \, f_{\mathrm{h}}^n - \tfrac{1}{2} \nabla \cdot (w_n^k \mathbf{u}_{\mathrm{c}} \mathbf{u}_{\mathrm{c}}) \cdot \nabla f_{\mathrm{h}}^n \right) \mathrm{d}V \\ - \int_{\Gamma_n^-} w_n^k \,\mathbf{u}_{\mathrm{c}} \cdot \mathbf{n} (f_{\mathrm{h}}^{n(-)} - \tfrac{1}{2}\mathbf{u}_{\mathrm{c}} \cdot \nabla f_{\mathrm{h}}^{n(-)}) \,\mathrm{d}\Gamma \\ - \int_{\Gamma_n^+} w_n^k \,\mathbf{u}_{\mathrm{c}} \cdot \mathbf{n} (f_{\mathrm{h}}^n - \tfrac{1}{2}\mathbf{u}_{\mathrm{c}} \cdot \nabla f_{\mathrm{h}}^n) \,\mathrm{d}\Gamma \qquad \forall w_n^k \end{aligned} \quad (7.29)$$

where Γ_n^+ is defined by ($\Gamma_n^- \cup \Gamma_n^+ = \Gamma_n$, $\Gamma_n^- \cap \Gamma_n^+ = \emptyset$).

7.3.5 accuracy of the convection scheme

The usefulness of the proposed method for Arbitrary Lagrangian Eulerian methods depends on whether large enough convective steps are possible without any stability problems or significant deterioration of the accuracy. The stability and accuracy are demonstrated by simulations of pure advection with a constant and a varying velocity field. Application to forming processes was reported in Geijselaers and Huétink (2000).

advection of a Gaussian bump

A rectangle of size 2x3.2 was divided into 1318 elements. The initial value of the field to be convected was a discontinuous least squares approximation of a Gaussian bump (Figure 7.7):

$$f = 0.01^{4(x^2+y^2)} \quad (7.30)$$

This bump was convected over a distance of 2 in $x-$direction. In Figure 7.8 the final distribution is shown when the advection is done in 81 steps. The maximum Courant number in any element was 0.95. The Courant number is defined as:

$$\mathrm{Cr}_n = \frac{1}{2V_n} \int_{\Gamma_n} \|\mathbf{u}_{\mathrm{c}} \cdot \mathbf{n}\| \,\mathrm{d}\Gamma \,; \qquad \mathrm{Cr}_{\max} = \max(\mathrm{Cr}_n) \quad (7.31)$$

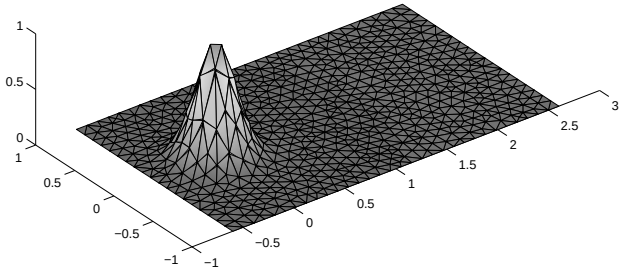

Figure 7.7: Advection of a Gaussian bump, the initial distribution.

In Figure 7.9 the evolution of the maximum and minimum values of the nodal averaged f is given. No instabilities are visible. The maximum value remains close to 1, while there is no undershoot. The error in the phase velocity is less than 10^{-5}.

A series of similar runs with different step sizes were done in order to asses the accuracy of the method in relation to the maximum Courant number. In Figure 7.10 the L_1 and the L_2 norms of the error at the end of the advection are shown. These norms are defined as:

$$E_1 = \int_V |f_h - f^{\text{ref}}| \, dV / \int_V |f^{\text{ref}}| \, dV$$
$$E_2 = \sqrt{\int_V (f_h - f^{\text{ref}})^2 \, dV / \int_V (f^{\text{ref}})^2 \, dV} \tag{7.32}$$

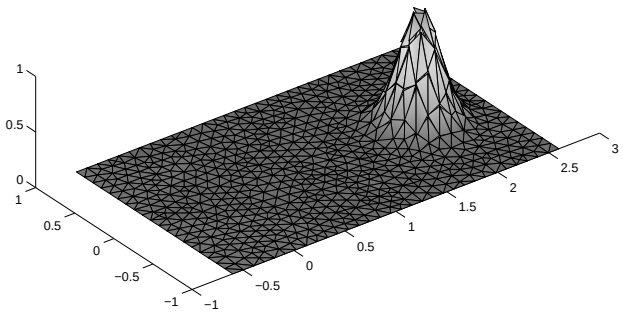

Figure 7.8: Advection of a Gaussian bump, the final profile ($\text{Cr}_{\text{max}} = 0.95$).

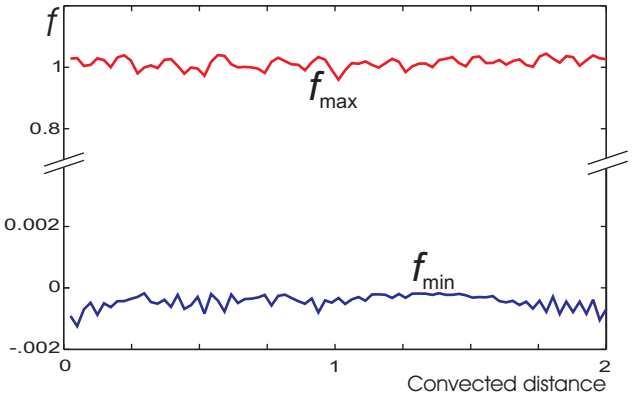

Figure 7.9: Evolution of minimum and maximum f value during advection ($\mathrm{Cr}_{\max} = 0.95$).

Also shown in Figure 7.10 are these error norms for the 2nd order method without the implicit terms. Inclusion of implicit terms according to (7.26) extends the stability region by approximately 30 %.

The smaller the step size, the smaller the error per step. However since more steps are required for smaller step sizes the cumulative error is not a monotonous function of the step size. An optimal step size exists which is approximately 0.2 for the second order method and which shifts to approximately 0.9 for the second order method with implicit terms. In Figure 7.11 the L_2 norms of the errors of several explicit discontinuous Galerkin methods are compared.

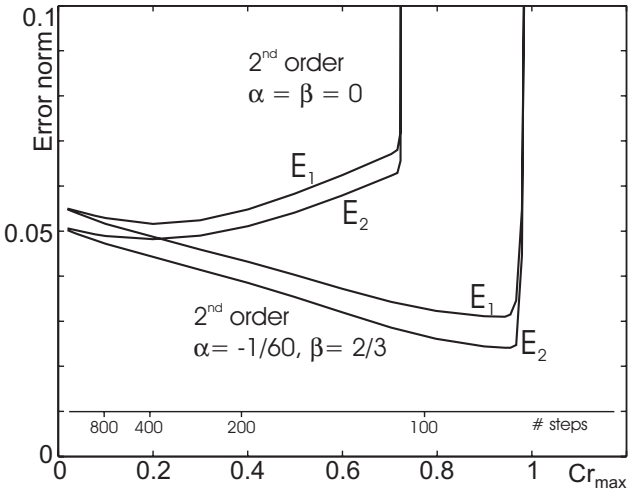

Figure 7.10: Error of the final distribution as a function of the maximum Courant number

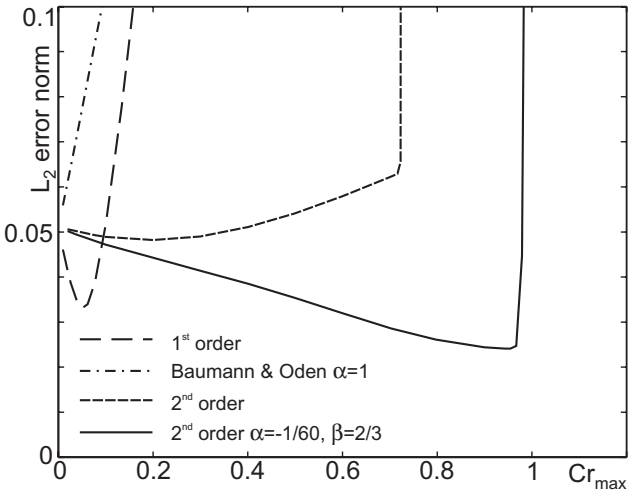

Figure 7.11: Error of the final distribution. Comparison with 1^{st} order explicit and 1^{st} order element-wise point-implicit (Baumann and Oden, 2000)

a non-uniform velocity field

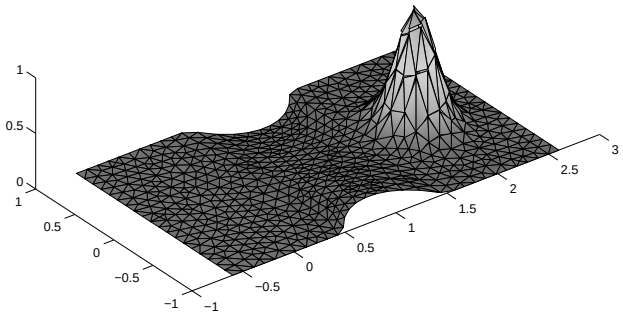

Figure 7.12: Advection of a Gaussian bump in a non-uniform velocity field, the final distribution ($\mathrm{Cr_{max}} = 0.95$).

To demonstrate pure advection in a varying velocity field, the simulation of advection of a Gaussian bump was repeated with velocities defined as:

$$\begin{Bmatrix} v_x \\ v_y \end{Bmatrix} = \begin{Bmatrix} 1 + \frac{1}{2}\cos\pi(x-1) \\ \frac{\pi y}{2}\sin\pi(x-1) \end{Bmatrix} \quad , \frac{1}{2} < x < \frac{3}{2} \quad ; \begin{Bmatrix} 1 \\ 0 \end{Bmatrix} \quad \text{elsewhere} \tag{7.33}$$

This is a divergence free velocity field. In order to avoid spurious inflow from the sides, the boundaries were adapted to follow the stream-lines.

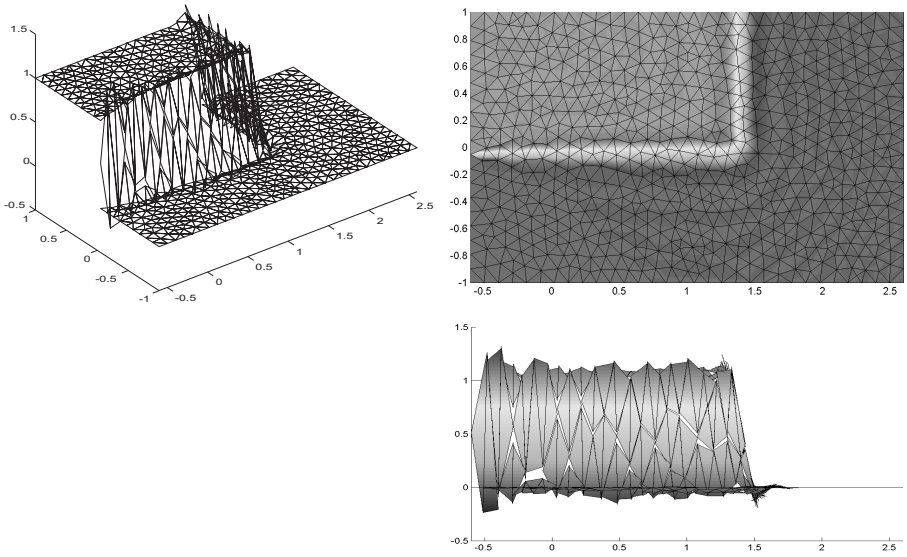

Figure 7.13: advection of a sharp front ($\mathrm{Cr}_{\max} = 0.92$).

A distance of 2 was covered in 93 steps. The maximum Courant number in any element was again 0.95. The resulting distribution is shown in Figure 7.12.

a sharp front

In these calculations the performance of the method in the presence of a sharp front is shown. The initial distribution is $f(\mathbf{x}, 0) = 0$. At the inflow boundary a condition ($f_0(y) = 0, y < -.053$; $f_0(y) = 1$ elsewhere) is prescribed. The result after 85 steps ($\mathrm{Cr}_{\max} = 0.92$) is shown in Figure 7.13. The front is typically smeared out over 3 elements. Loss of monotonicity is visible as a slight Gibbs effect.

conclusions

A convection scheme has been developed which is based on the discontinuous Galerkin method. The data to be convected are assumed to be linearly interpolated per element and may be discontinuous across element boundaries. The resulting field after convection is linear per element and discontinuous across element boundaries. The scheme is explicit and is suited for element by element treatment. It is stable and accurate for Courant numbers up to 0.9.

7.4 Simulation of steady laser hardening

A steady state model of laser hardening was set up which had identical process parameters as the the models in Chapter 6. The finite element model is show in Figure 7.14; it consists

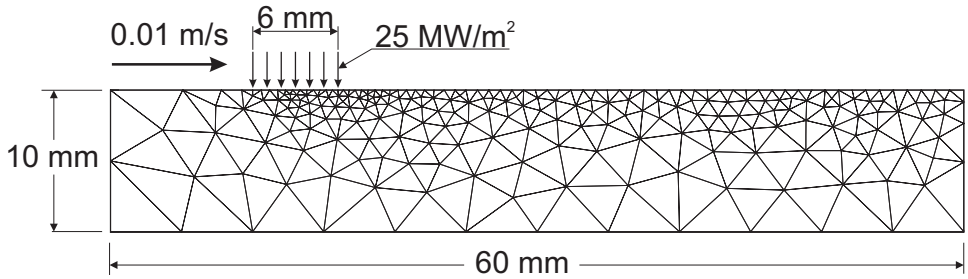

Figure 7.14: The finite element model for ALE calculations

of 892 nodes, 401 six-node triangular elements and 67 heat convection elements on the top and bottom faces.

Results were obtained for a thermal calculation with phase transformations, the inclusion of distortions has not yet succeeded. For the thermal calculation essentially a transient analysis as in Chapter 6 was performed in which every transient step was followed by a convection step. The transient calculation was prolonged until a steady state was reached. Convection was applied to the temperatures as well as to the phase fractions.

During the calculation a constant time step of 0.0153 s was used. This results in a convective displacement of 0.153 mm per step. The maximum Courant number in any element is 0.8.

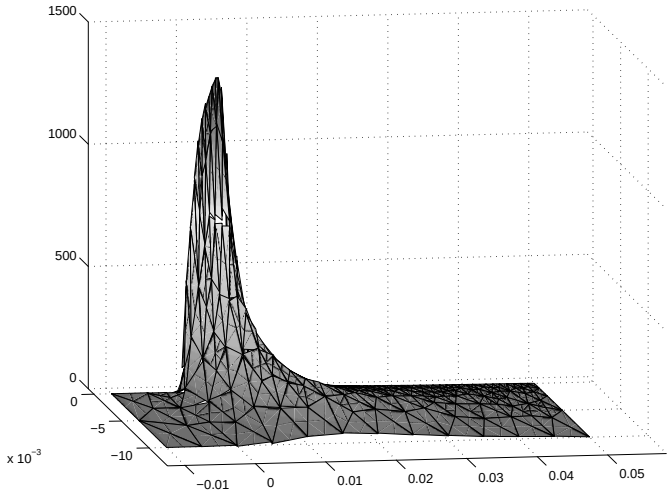

Figure 7.15: Temperature distribution during steady laser hardening

The temperature and the martensite distributions are shown in Figures 7.15 and 7.16. In Figure 7.17 the temperature and the phase fraction distributions along the top face are shown. The temperature distribution is quite smooth. The phase fractions give a very ragged

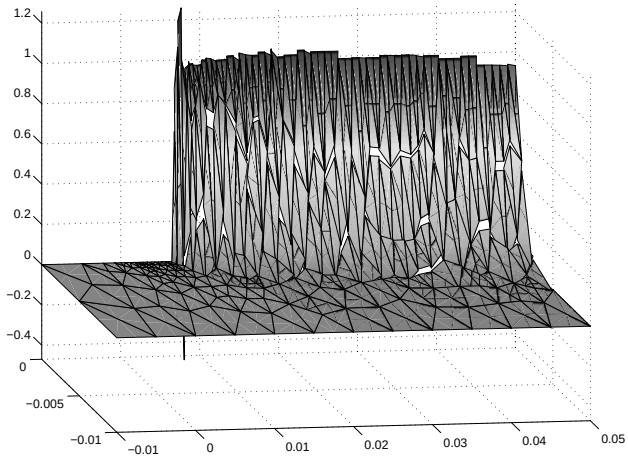

Figure 7.16: Martensite distribution during steady laser hardening

line. This is mainly caused by the extrapolation from integration points to nodal points. A second reason is very sharp gradients which have to be resolved within only one or two elements. As was shown in Section 7.3.5 this causes some local over-shoot. The martensite contents appears to be diminishing towards the end of the slab. This is an artifact which is caused by the coarsening of the grid.

Comparison of the temperature distribution along the top with the evolution during a stationary laser pulse shows that in the ALE calculation a lower value of the maximum temperature is reached. This is most probably due to the coarser mesh used in the ALE computation.

7.5 Conclusions

The Arbitrary Lagrangian-Eulerian method was applied to the process of steady laser hardening. Results were obtained for temperatures and phase fractions; the stress calculation was not yet implemented.

A new convection algorithm was developed for the remap of state variables. It is based on a second order Taylor expansion which was discretized by the discontinuous Galerkin method. It has the advantage of being able to cope with state variable fields which are discontinuous across element boundaries.

The convection method was shown to be stable and accurate for Courant numbers upto 0.9. The method is explicit and suitable for element by element calculation of the remap.

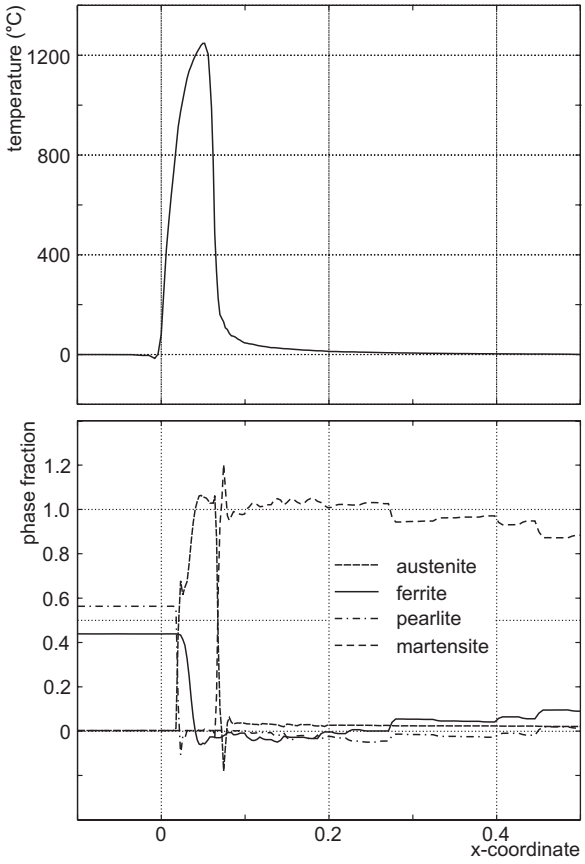

Figure 7.17: Temperature and phase fraction distributions along the top face

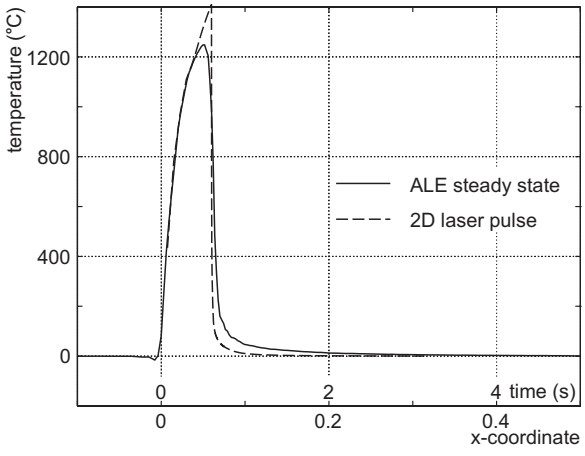

Figure 7.18: The temperature evolution at the top face; comparison of 2-D and ALE results

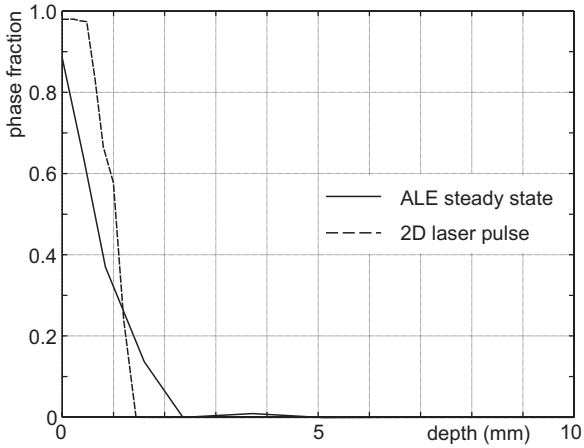

Figure 7.19: Martensite distribution at the outflow boundary

8. A One-Step Steady State method

In the previous chapter the temperatures and phase fractions due to steady state laser hardening were simulated using an essentially transient method. When the fields caused by a scanning laser are viewed in a reference frame which moves with the heat source, the spatial distribution of the field variables remains constant: it is a steady state process. In this chapter an attempt at modelling steady laser hardening is made in which the steadiness of the process is exploited.

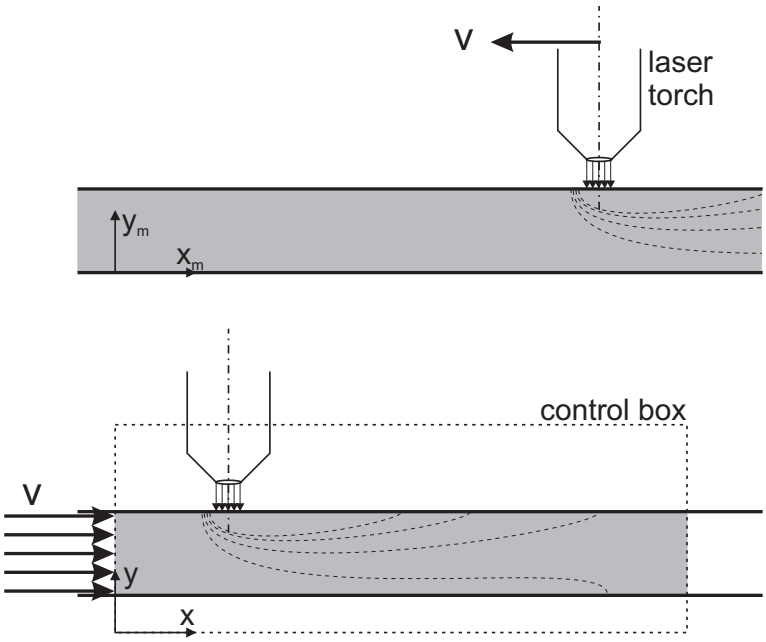

Figure 8.1: A control box for steady state laser processing.

A control box is fixed to the laser and the material is assumed to pass through this box (Figure 8.1). The material entering the box has properties constant in time. The reference system $\mathbf{x}_m$ is attached to the material, the Eulerian frame $\mathbf{x}$ is attached to the control box.

In the steady state the material derivative of any field variable f is found as:

$$\dot{f} = \mathbf{v} \cdot \nabla f \tag{8.1}$$

The time coordinate is replaced by a spatial coordinate. It is proportional to the distance along a streamline. A time derivative becomes a derivative along a streamline, integration in time is replaced by integration along streamlines. This type of modelling is termed a Eulerian description.

Eulerian methods for thermal analysis are quite common. When a continuous discretization of the temperature field is used these methods rely on the SUPG method (Brooks and Hughes, 1982) to suppress the instabilities which occur when the convection becomes dominant. A discretization with discontinuous temperatures which is inherently stable has been reported by Baumann and Oden (1999).

The mechanical problem is far from trivial. Most Eulerian simulations for structural problems such as rolling or extrusion use velocities as primary variables and viscoplastic or elasto-viscoplastic material behaviour (Gu and Goldak, 1994; Hacquin *et al.*, 1996; Ruan, 1999). Efforts along this line to include elasto-plastic material behaviour have invariably encountered stability problems (Thompson and Yu, 1990).

A different method, proposed by Balagangadhar and Tortorelli (2000) for rolling and extrusion and extended to steady thermal processing in Balagangadhar *et al.* (1999) uses displacements rather than velocities. It is called "Displacement Based Reference Frame Formulation". In Shanghvi and Michaleris (2002) it has been used for simulation of laser processing. It will also be adopted here.

8.1 The displacement based reference frame formulation

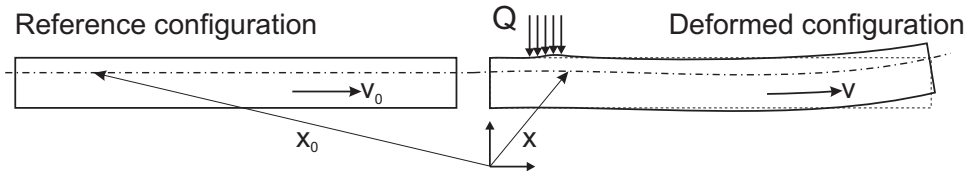

Figure 8.2: Steady state laser processing in the displacement based reference frame formulation.

Consider a steady state laser process as shown in Figure 8.2. An attractive way of analyzing this process arises when we compare an identical slab of workpiece material at two different instances in time. The reference configuration is defined when the slab has not yet entered the work zone of the process. The deformed configuration is defined when the volume under consideration has, at some later time, entered the work zone and is being processed.

Concentrating on the mechanical problem the following steps are part of a calculation using the displacement based formulation:

- Comparison of the locations of "identical" material points in both configurations directly yields the deformation gradient.

- Suitable differentiation of the deformation gradient along the streamlines yields a deformation rate.

- This deformation rate is then used to calculate a plastic deformation rate.
- Integration of the plastic deformation rate along the streamline yields the plastic deformations.
- The elastic strains are found after subtracting the plastic deformations from the actual deformations. Then the stresses are known.
- These stresses are used to check whether the deformed configuration is indeed in equilibrium. When this is not the case, the locations of the material points are updated and the calculation is reiterated.

Balagangadhar *et al.* (1999) presented an implementation in which temperatures, displacements and also plastic strains and the equivalent plastic strain appear as primary variables. All these variables are nodal variables.

In our implementation we used only displacements and heat flows as primary variables. The thermal problem with the phase transformations was solved first. Next, the distortions were calculated while keeping the temperature and the phase fraction distributions constant. The influence of the stresses on the phase transformations was not yet implemented.

8.2 Governing equations

The governing equations used were derived in Chapters 2 and 3. Here we summarize the most relevant expressions.

8.2.1 phase transformations

The evolution of diffusion related transformations is described by the Avrami equation (2.4) in rate form:

$$\dot{\varphi} = \dot{\varphi}(\varphi, T) \tag{8.2}$$

The martensite transformation is described by the Koistinen-Marburger relation (2.11) also written in rate form:

$$\dot{\varphi} = \frac{\mathrm{d}\varphi}{\mathrm{d}T}(\varphi, T)\dot{T} \tag{8.3}$$

The final phase content is found by integration along the streamlines:

$$\begin{aligned} \mathbf{v} \cdot \nabla\varphi &= \dot{\varphi} \\ \varphi &= \varphi_0 \qquad \text{at } \Gamma^- \end{aligned} \tag{8.4}$$

where Γ^- is the inflow boundary of the domain.

8.2.2 mechanical equilibrium

The mechanical equilibrium equation in the absence of body forces is:

$$\begin{aligned} \boldsymbol{\sigma} \cdot \nabla &= \mathbf{0} \\ \boldsymbol{\sigma} \cdot \mathbf{n} &= \mathbf{t} \qquad \text{on } \Gamma_\sigma \\ \mathbf{u} &= \mathbf{u}_0 \quad \text{on } \Gamma_\mathrm{u} \end{aligned} \tag{8.5}$$

The strain is the summation of an elastic strain, a plastic strain and contributions from transformation strain, thermal dilatation and transformation plasticity:

$$\boldsymbol{\varepsilon} = \boldsymbol{\varepsilon}^{\mathrm{el}} + \boldsymbol{\varepsilon}^{\mathrm{pl}} + \boldsymbol{\varepsilon}^{\mathrm{tr}} + \boldsymbol{\varepsilon}^{\mathrm{th}} + \boldsymbol{\varepsilon}^{\mathrm{tp}} \tag{8.6}$$

The sum of the thermal dilatation and of the transformation strain is:

$$\begin{aligned} \boldsymbol{\varepsilon}^{\mathrm{tr}} + \boldsymbol{\varepsilon}^{\mathrm{th}} &= (\sqrt[3]{\rho_0/\rho} - 1)\mathbf{1} \\ \text{where:} \quad \rho(\varphi, T) &= \sum_i \varphi^i \rho^i \end{aligned} \tag{8.7}$$

where $\rho^i(T)$ is the density of phase i. The transformation plasticity is linked to the deviatoric stress $\mathbf{s}$ Equation (3.18). The description of plastic deformation is based on the Von Mises yield criterion with isotropic hardening Equation (3.26). Combining these yields an equation for the sum of the plastic and transformation plastic strain rate components:

$$\begin{aligned} \mathbf{d}^{\mathrm{pl}} + \mathbf{d}^{\mathrm{tp}} = \frac{1}{1+h_\varepsilon}\frac{3\mathbf{ss}}{2\sigma_{\mathrm{y}}^2} : \mathbf{d} + \frac{1}{1+h_\varepsilon}\frac{\mathbf{s}}{2G}\left(\frac{1}{G}\frac{\mathrm{d}G}{\mathrm{d}T} - \frac{3Gh_{\mathrm{T}}}{\sigma_{\mathrm{y}}}\right)\dot{T} \\ + \frac{1}{1+h_\varepsilon}\frac{3\mathbf{s}}{2\sigma_{\mathrm{y}}}\sum_i \left(h_\varepsilon K^i F^{i\prime} - h_\varphi^i\right)\dot{\varphi}^i + \frac{h_\varepsilon}{1+h_\varepsilon}\frac{3\mathbf{s}}{2\sigma_{\mathrm{y}}} c_{\mathrm{rc}}\varepsilon^{\mathrm{p}} \end{aligned} \tag{8.8}$$

The plastic strain rate and the transformation plasticity rate per fraction are integrated along the streamlines to obtain the plastic strain:

$$\begin{aligned} \mathbf{v}\cdot\nabla(\boldsymbol{\varepsilon}^{\mathrm{pl}} + \boldsymbol{\varepsilon}^{\mathrm{tp}}) &= \mathbf{d}^{\mathrm{pl}} + \mathbf{d}^{\mathrm{tp}} \\ \boldsymbol{\varepsilon}^{\mathrm{pl}} + \boldsymbol{\varepsilon}^{\mathrm{tp}} &= \mathbf{0} \qquad \text{at } \Gamma^- \end{aligned} \tag{8.9}$$

This is a scalar equation, which applies to every component of the tensors. After integration of the plastic strain rates to plastic strains, the stress is calculated:

$$\begin{aligned} \boldsymbol{\sigma} &= \mathbf{E} : (\boldsymbol{\varepsilon} - \boldsymbol{\varepsilon}^{\mathrm{pl}} - \boldsymbol{\varepsilon}^{\mathrm{tp}} - \boldsymbol{\varepsilon}^{\mathrm{th}} - \boldsymbol{\varepsilon}^{\mathrm{tr}}) \\ &= \mathbf{E} : \boldsymbol{\varepsilon} - 2G(\boldsymbol{\varepsilon}^{\mathrm{pl}} + \boldsymbol{\varepsilon}^{\mathrm{tp}}) - 3k_{\mathrm{b}}(\varepsilon^{\mathrm{th}} + \varepsilon^{\mathrm{tr}})\mathbf{1} \end{aligned} \tag{8.10}$$

8.2.3 thermal equilibrium

The heat flow is calculated according to Fourier's equation:

$$\begin{aligned} \mathbf{q} &= -\kappa\nabla T \\ \mathbf{q}\cdot\mathbf{n} &= q_0 \qquad \text{on } \Gamma = \Gamma_{\mathrm{q}} \\ T &= T_{\mathrm{e}} \qquad \text{on } \Gamma = \Gamma_{\mathrm{T}} \\ \mathbf{q}\cdot\mathbf{n} &= \gamma(T - T_{\mathrm{e}}) \quad \text{on } \Gamma = \Gamma_{\mathrm{e}} \end{aligned} \tag{8.11}$$

The equation of conservation of energy (3.6) is used to calculate the temperature rate:

$$\rho c_{\mathrm{p}}\dot{T} = -\nabla\cdot\mathbf{q} - \rho\dot{H}_\varphi \tag{8.12}$$

To obtain the temperatures the temperature rate has to be integrated. For a steady state process the time integration is again replaced by an integration along the streamlines:

$$\begin{aligned} \mathbf{v} \cdot \nabla T &= \dot{T} \\ T &= T_0 \qquad \text{on } \Gamma^- \end{aligned} \tag{8.13}$$

8.3 Discretization

8.3.1 convection equation

The streamline integration of any quantity f, be it a strain component, phase fraction, equivalent plastic strain or temperature, is described by the convection equation:

$$\mathbf{v} \cdot \nabla f = \dot{f} \tag{8.14}$$

As is apparent from Figure 8.2 locating the streamlines in the reference configuration is a trivial task. Using the deformation gradient $\mathbf{F}$ Equation (8.14) can be transformed to the undeformed configuration:

$$\mathbf{v} \cdot \nabla f = \mathbf{v} \cdot \mathbf{F}^{\mathrm{T}} \cdot \mathbf{F}^{-\mathrm{T}} \cdot \nabla f = \mathbf{v}_0 \cdot \nabla_0 f = v_0 \frac{\partial f}{\partial x_0} \tag{8.15}$$

In the reference configuration the velocity is constant and all streamlines are parallel to the x-axis. Therefore all streamline integration is performed in the reference configuration. A very stable discretization of the convection equations (8.9) and (8.13) is the discontinuous Galerkin method (Fortin and Fortin, 1989). The field f is as in Section 7.3.2, discretized using discontinuous base functions $w_m(\mathbf{x})$:

$$f_{\mathrm{h}}^m(\mathbf{x}) = \sum_k w_m^k(\mathbf{x})\, f_k^m \tag{8.16}$$

Since the field to be solved for is discontinuous, the jump at the inflow boundary of every element is weighted upon discretization (cf. Equation (7.15)).

$$v_0 \int_{V_m} w_m^k \frac{\partial f_{\mathrm{h}}^m}{\partial x_0}\, \mathrm{d}V - v_0 \int_{\Gamma_m^-} n_x w_m^k (f_{\mathrm{h}}^m - f_{\mathrm{h}}^{m(-)})\, \mathrm{d}\Gamma = \int_{V_m} w_m^k \dot{f}\, \mathrm{d}V \quad \forall w_m^k \tag{8.17}$$

Here Γ_m^- is defined as that part of the boundary of the m^{th} element where the x-component of the outward pointing normal to the element boundary $n_x < 0$. Here also $f_{\mathrm{h}}^{m(-)}$ is the value of f in the elements which share boundaries Γ_m^- with the m^{th} element, the upwind elements.

To obtain a well posed problem the initial condition at the inflow of the domain has to be prescribed. The resulting matrix equations have the following form:

$$[\mathrm{D}]\{\mathrm{f}^{\mathrm{e}}\} = [\mathrm{B}]\{\dot{\mathrm{f}}^{\mathrm{e}}\} + [\mathrm{D}_0]\{\mathrm{f}_0\} \tag{8.18}$$

All quantities which are defined inside the elements and which are interpolated by discontinuous functions are written with the suffix $()^{\mathrm{e}}$. In effect, these are variables which are defined in the integration points such as temperatures and strains.
The solutions obtained in this way for the convection equations are free of spurious oscillations and show hardly any cross-wind diffusion.

8.3.2 thermal equations

For the thermal problem the discretization Equation (5.5) from Chapter 5 is used:

$$\int_V \mathbf{r}\cdot\mathbf{q}\,\mathrm{d}V + \int_{\Gamma_e} \frac{\kappa}{\gamma} r_n q_n \,\mathrm{d}\Gamma = \int_V \kappa \nabla\cdot\mathbf{r}T\,\mathrm{d}V - \int_{\Gamma_T\cup\Gamma_e} \kappa r_n T_e \,\mathrm{d}\Gamma \qquad \forall \mathbf{r} \tag{8.19}$$

where $\mathbf{r}$ is a vector weight function with $r_n = 0$ on Γ_q. The temperature rates are solved directly in the integration points from (8.12). The temperatures are obtained from the temperature rates by integration along the the streamlines using (8.13). The resulting matrix equations are written as:

$$\begin{aligned} [M]\{q\} &= [C]\{T^e\} + \{Q\} \\ \{\dot{T}^e\} &= [L]\{q\} + \{\dot{\Phi}_T\} \\ [D]\{T^e\} &= [B]\{\dot{T}^e\} + [D_0]\{T_0\} \end{aligned} \tag{8.20}$$

The coefficients of [C] and [L] are temperature dependent, so is the latent heat term $\{\dot{\Phi}_T\}$. The system is non-linear and requires an iterative procedure for its solution.

8.3.3 mechanical equilibrium

The mechanical equilibrium equation (8.5) is written in a weak form using a vector weight function $\mathbf{w}$, which is equal to $\mathbf{0}$ on Γ_u:

$$\int_V \mathbf{w}\cdot\boldsymbol{\sigma}\cdot\nabla\,\mathrm{d}V = \mathbf{0} \quad \forall \mathbf{w} \tag{8.21}$$

After partial integration and substitution of boundary conditions on the prescribed stress boundaries Γ_σ follows:

$$\int_V \mathrm{sym}(\mathbf{w}\nabla):\boldsymbol{\sigma}\,\mathrm{d}V = \int_{\Gamma_\sigma} \mathbf{w}\cdot\mathbf{t}\,\mathrm{d}A \quad \forall \mathbf{w} \tag{8.22}$$

Substitution of (8.10)into this expression yields:

$$\begin{aligned} \int_V \mathrm{sym}(\mathbf{w}\nabla):\mathbf{E}:\boldsymbol{\varepsilon}\,\mathrm{d}V = &\int_V 2G\,\mathrm{sym}(\mathbf{w}\nabla):(\boldsymbol{\varepsilon}^{\mathrm{pl}} + \boldsymbol{\varepsilon}^{\mathrm{tp}})\,\mathrm{d}V \\ &+ \int_V 3k_b\,\mathrm{tr}(\mathbf{w}\nabla)(\varepsilon^{\mathrm{th}} + \varepsilon^{\mathrm{tr}})\,\mathrm{d}V + \int_{\Gamma_\sigma} \mathbf{w}\cdot\mathbf{t}\,\mathrm{d}A \quad \forall \mathbf{w} \end{aligned} \tag{8.23}$$

The plastic strain rates in the elements are calculated using (8.8). The strain rates are integrated to strains using Equation (8.9). This results in a system of matrix equations:

$$\begin{aligned} [K]\{u\} &= [W]\{\varepsilon^{\mathrm{pl(e)}}\} + \{F(T,\varphi)\} + \{F_0\} \\ \{d^{\mathrm{pl(e)}}\} &= [Y]\{u\} + [G]\{\dot{T}^e\} + \{\dot{\Phi}_d\} \\ [D]\{\varepsilon^{\mathrm{pl(e)}}\} &= [B]\{d^{\mathrm{pl(e)}}\} + [D_0]\{\varepsilon_0^{\mathrm{pl}}\} \end{aligned} \tag{8.24}$$

The matrix [K] is the regular elastic stiffness matrix. The matrices [Y], [G] and the vector $\{\dot{\Phi}_d\}$ depend on the stress state. As a consequence this is a highly non-linear system.

8.3.4 the strain rate d

The displacement field **u** is C_0 continuous across element boundaries. This means that the strain field $\boldsymbol{\varepsilon}$ is discontinuous. The strain rate **d** is the material derivative of the strain:

$$\mathbf{d} = \mathbf{v} \cdot \nabla \boldsymbol{\varepsilon} \tag{8.25}$$

Just taking the derivative of the discontinuous strains in the elements does not give a proper strain rate. The jumps across boundaries with neighbouring elements have to also be taken into account. One method is to construct a continuous field by nodal averaging (Hinton and Campbell, 1974; Yu *et al.*, 2001). Alternatively some sort of gradient recovery (Zienkiewicz *et al.*, 1999) may be employed. Balagangadhar and Tortorelli (2000) on the other hand took the local derivative, disregarding inter-element jumps. They remarked that although theoretically not correct, this did not cause any problems.

In our case we need only the derivative in the streamline direction. To obtain this we resort again to the discontinuous Galerkin method of Section 8.3.1. This time, however, it is used in the opposite direction, in order to obtain material derivatives from a known discontinuous field. Compare with Equation (8.18):

$$[\mathrm{B}]\{\mathrm{d}^\mathrm{e}\} = [\mathrm{D}]\{\varepsilon^\mathrm{e}\} \tag{8.26}$$

Inspection of matrix [B] shows that the contribution from one element has no coupling with that from other elements. It is a diagonal 3x3 'mass' matrix. The only external coupling comes from [D], which refers to the upwind neighbours. Calculation of **d** is performed element by element involving upwind neighbours only.

8.4 Implementation

Quadratic triangles are used with **u** and **q** as nodal variables. Per element three integration points are used. This implies that the interpolation of the element fields $\boldsymbol{\sigma}$, $\boldsymbol{\varepsilon}$, **d**, φ and T is linear, with the integration point values as basis.

The convection equation (8.14) does not change between iterations. Therefore equation (8.18) is solved right at the beginning. This allows for solution of the the integration point temperatures $\{\mathrm{T}^\mathrm{e}\}$ in equations (8.20) in terms of the nodal point heat fluxes **q**:

$$[\mathrm{K_{qq}}]\{\mathrm{q}\} = \{\mathrm{R_q}\} \tag{8.27}$$

The matrices are evaluated as:

$$\begin{aligned} [\mathrm{K_{qq}}] &= [\mathrm{M}] - [\mathrm{C}][\mathrm{D}^{-1}][\mathrm{B}][\mathrm{L}] \\ \{\mathrm{R_q}\} &= \{\mathrm{Q}\} + [\mathrm{C}]\{\mathrm{T_0}\} + [\mathrm{C}][\mathrm{D}^{-1}][\mathrm{B}]\{\dot{\Phi}_\mathrm{T}\} \end{aligned} \tag{8.28}$$

The solution requires only a few iterations to account for temperature dependent properties and temperature dependent phase transformations.

Having the solution of the convection equation at hand also allows us to directly assemble a similar system matrix for the mechanical problem:

$$[\mathrm{K_{uu}}]\{\mathrm{u}\} = \{\mathrm{R_u}\} \tag{8.29}$$

The matrices can be evaluated as:

$$\begin{aligned} [\mathrm{K_{uu}}] &= [\mathrm{K}] - [\mathrm{W}][\mathrm{D}^{-1}][\mathrm{B}][\mathrm{Y}] \\ \{\mathrm{R_u}\} &= [\mathrm{W}][\mathrm{D}^{-1}][\mathrm{B}]([\mathrm{G}]\{\dot{\mathrm{T}}^{\mathrm{e}}\} + \{\dot{\Phi}_{\mathrm{d}}\}) + \\ &\quad + [\mathrm{W}]\{\varepsilon_0^{\mathrm{pl}}\} + \{\mathrm{F}(T, \varphi)\} \end{aligned} \tag{8.30}$$

Assembly of the element matrix of one element requires looping over all elements upwind from the considered element. This implies that assembly of the system matrices of equation (8.30) takes roughly $O(N_{\mathrm{el}}^2)$ operations. Already for an average size model this is prohibitive. Furthermore, since the element reactions of one element are determined by the distortions in all the upwind elements, matrix $[\mathrm{K_{uu}}]$ will not be sparse. This means that, when all nodal points are sorted with respect to their distance from the inflow boundary, practically all matrix elements below the diagonal will be non-zero. The required memory scales roughly with N_{node}^2.

Our experience is that a fairly good convergence can be reached when only the elastic stiffness matrix [K] is used to find feasible solution directions. This is combined with one-dimensional line searches. In this way only the right hand side $\{\mathrm{R_u}\}$ needs to be assembled. Convergence is slow but steady until after approximately 50 iterations the norm of the unbalance becomes lower than 1 % of $\|\{\mathrm{F}(T, \varphi)\}\|$, the norm of the nodal forces due to thermal and transformation dilatation. This is illustrated in Figure 8.6 for the simulations in section 8.5.

8.4.1 outlet boundary conditions

Special boundary conditions are needed at the outflow boundary in order to specify the steadiness of the stress distribution. Balagangadhar and Tortorelli (2000) propose a procedure in which the resultant stress in an element at the outflow boundary is mirrored in an identical phantom element across from this boundary. The contribution to the nodal reaction from this phantom element is then added to the nodal reactions in the boundary nodes.

Their finite element model is a structured mesh of quadrilaterals, so that the elements adjacent to the outflow boundary are easily identified. This in not the case with our unstructured mesh of triangular elements. Careful scrutiny of their procedure reveals that it results in cancellation of the components of the residual vector parallel to the flow direction. The values of perpendicular components will be doubled. The former is correct, the latter however is not justified, were it not that in a fully developed steady flow these perpendicular components ought to be zero.

Inspired by this procedure we adopt a slightly simpler working method: the residual force components parallel to the flow direction in the outlet boundary nodes are made equal to zero while the perpendicular components are left untouched. Note that this does not mean that the outlet boundary is specified as stress free. Rather this procedure specifies that it is stress increment free, i.e. the current stress is preserved.

8.5 Simulations of steady laser hardening

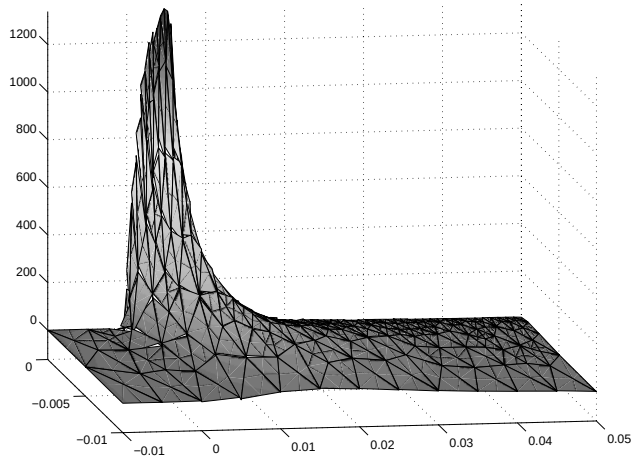

Figure 8.3: Steady laser hardening, the temperature distribution.

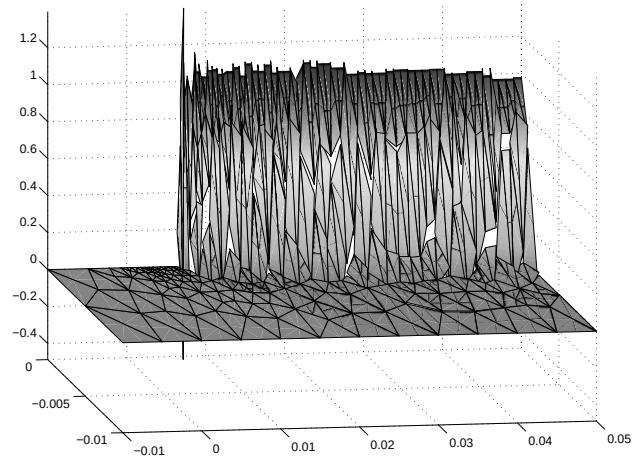

Figure 8.4: Steady laser hardening, the martensite distribution.

Results obtained with the steady state method of this chapter were already reported in Geijselaers *et al.* (2001). Here results are presented of the method applied to a simulation of a laser hardening process of a steel slab with identical parameters as in Chapters 6 and 7. The model is the same as that shown in Figure 7.14. It consists of 401 elements and 892 nodal points.

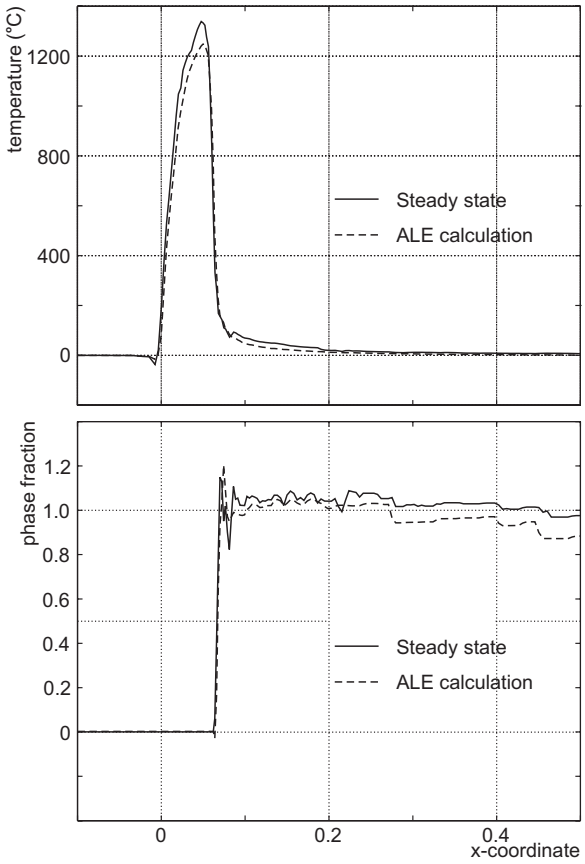

Figure 8.5: Steady laser hardening, temperature and martensite distributions along the top face.

temperatures and phase distribution

In Figures 8.3 and 8.4 the temperature and the martensite distributions are shown. The evolutions of temperature and martensite fraction along the top surface are shown in Figure 8.5 compared with results from the ALE calculation. As can be seen, the agreement of both temperature and martensite distributions is excellent. Eleven iterations were required to obtain an accuracy of 0.1% of the heat flow **q**.

The streamline integration, however, required some attention. In particular the straight calculation of phase fraction transformation rates and integration by solution of the convection equation:

$$\{\varphi^{\mathrm{e}}\} = [\mathrm{D}^{-1}][\mathrm{B}]\{\dot{\varphi}^{\mathrm{e}}\} + \{\varphi_0^{\mathrm{e}}\} \tag{8.31}$$

does not yield a stable algorithm. Therefore the following routine has been developed:

1. Sum each row of matrix $[\mathrm{D}^{-1}][\mathrm{B}]$ to obtain the (exact!) time required for the material to reach the considered integration point from the inflow boundary.

2. Sort the integration points in the order of the time from the inflow.

3. Estimate the dwelling time of the material in the region covered by each integration point. The diagonal elements of $[D^{-1}][B]$ give a good estimate of this time.

4. Calculate the increment at each integration point in sorted order, first calculating the initial value for the integration point by summing the convective contribution for this particular integration point from all upstream integration points.

5. The material rate is then obtained by dividing the increment by the dwelling time.

The sorting is applied to avoid having to iterate, since current local temperatures and phase fractions determine the temperature rates as well as the phase fraction rates. The dwelling time is used to calculate an increment. The increment is then divided by this time to obtain a rate. In this way overshoots caused by local high rates are avoided.

stresses and distortions

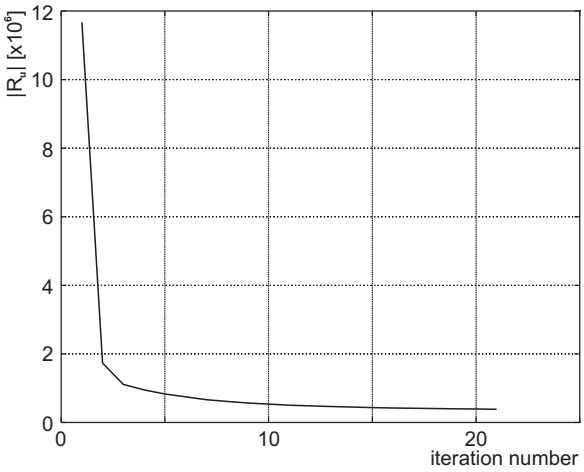

Figure 8.6: Convergence behaviour of a steady state thermo-mechanical simulation.

Calculation of the distortions was first attempted with an implementation based on the consistent system matrix $[K_{uu}]$ of Equation (8.30). This did not yield a result with satisfactory convergence. Some pertaining inconsistencies between the system matrix and the assembly of the unbalance vector $\{R_u\}$ could not be remedied. Moreover the calculation was very slow due to excessive time required for assembly of the matrix.

The time consumption statistics for this model are: assembly of the consistent matrix $[K_{uu}]$: 1800 s; assembly of the unbalance force vector $\{R_u\}$: 50 s; assembly of the elastic stiffness matrix [K]: 1.2 s. Experiments with different size models indicate that the time for assembly of $[K_{uu}]$ scales as $N_{el}^{2.1}$; the time for assembly of $\{R_u\}$ scales as $N_{el}^{1.5}$.

As already mentioned it is more stable and also cheaper to use the elastic stiffness matrix [K] to find a feasible direction. The step size in this direction is determined by a

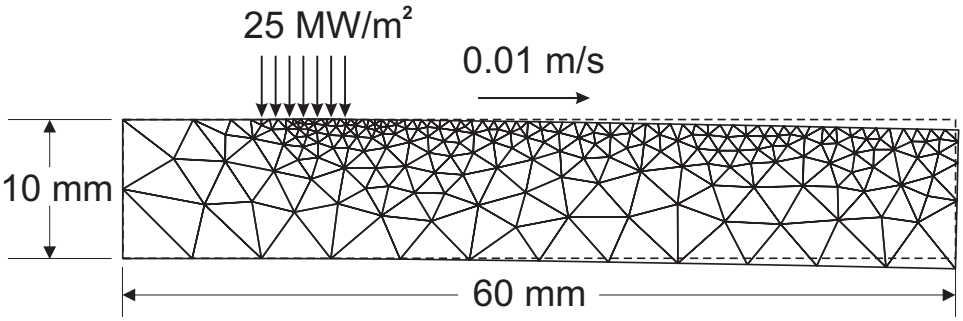

Figure 8.7: Steady laser hardening, the final distortion.

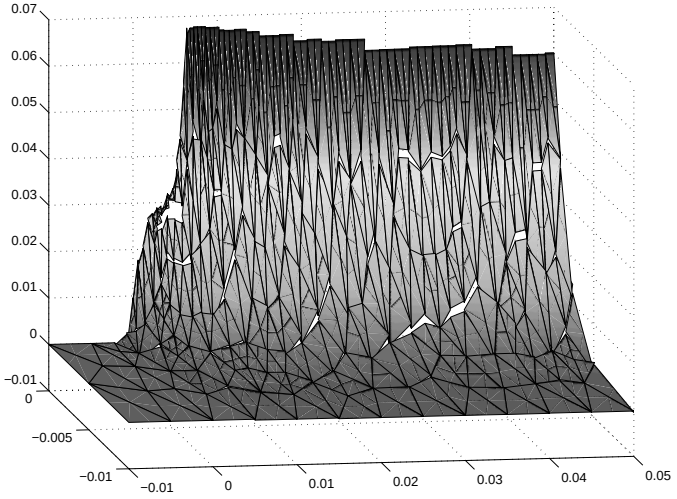

Figure 8.8: Steady laser hardening, distribution of the equivalent plastic strain.

one dimensional line search. Typically 5 to 7 evaluations of $\{R_u\}$ are required per iteration. Convergence is slow but steady as is shown in Figure 8.6.

The distortion of the slab is apparent from Figure 8.7. Consistent with the results from Chapters 6 the heat treatment causes a slightly convex upper surface. However, since this is a plane strain simulation, it may be expected that the deformations are grossly exaggerated.

In Figure 8.8 the distribution of the equivalent plastic strain is shown. Plastic deformation is seen to occur specifically at two instances, during heating and during martensite transformation.

8.6 Conclusions

A one-step steady state method was developed for simulation of steady laser processing. The method is based on the displacement based reference formulation of Balagangadhar

and Tortorelli (2000). This method was modified such that only displacements and heat flows appear as primary variables. The use of the discontinuous Galerkin method for both streamline integration and streamline differentiation was added. The steady state method was demonstrated on a thermo-mechanical calculation of steady laser hardening.

9. Conclusions and Recommendations

In this thesis the numerical simulation of solid state phase transformations has been studied. Emphasis was placed on the simulation of laser transformation hardening.

Phase transformation simulation

Laser hardening is characterized by high thermal rates and short interaction times. A kinetic model, which is based on a simple carbon balance, has been developed to describe super-heating of ferrite and super-cooling of austenite. For the determination of the required kinetic parameters a method is presented to estimate transformation time constants from continuous cooling tests rather than from isothermal tests.

Constitutive equations

A comprehensive set of constitutive equations for thermo-mechanical calculations with solid state phase transformations have been derived. The rate equations were integrated consistently to obtain incremental equations suitable for simulations with integration time steps of the order of the transformation time constants.

Implementation of the full set of equations has not yet been accomplished. Thermo-mechanical simulations with a staggered iteration scheme run well when no stress influence on transformation kinetics is modelled. The inclusion of stress influence causes instabilities when not implemented in a fully consistent manner.

ALE method

For the ALE method a convection algorithm is required which is stable and accurate at reasonably large convective displacements. The second order discontinuous Galerkin method enhanced with implicit terms is an explicit method which yields accurate results for Courant numbers up to 0.9.

This is demonstrated on simulations of steady state laser hardening. Results of ALE calculations of the thermal field during steady laser processing have been presented. No results have yet been obtained for the full thermo-mechanically coupled problem.

Steady state method

The displacement based reference formulation for steady state thermo-mechanical processes has been adapted for simulation of steady state laser hardening. The steady convection or

stream line integration is modelled using a discontinuous Galerkin formulation. The discontinuous Galerkin method can also be used for the stream line differentiation of discontinuous data fields.

Thermal as well as thermo-mechanical calculations have been performed. The results of the steady state thermal calculation agree with the results obtained with the ALE method.

A. Material Data for Ck45

The material data used in the simulations were obtained from several sources. Since the data from different sources were sometimes conflicting or dealing with other steel grades, the numerical values were treated as approximate values. In Figures A.2 through A.7 our interpretation of these data is shown.

The mechanical data and thermal material data were obtained from:
Hildenwall and Ericson (1977)
Denis *et al.* (1987)
Krielaart (1995)
Gür and Tekkaya (1996)

The data for the transformation plasticity and the data concerning stress-transformation interaction were obtained from:
Bhattacharyya and Kehl (1955)
de Jong and Rathenau (1961)
Greenwood and Johnson (1965)
Aeby-Gautier (1985)
Sjöström (1985)
Denis *et al.* (1985)
Videau *et al.* (1996)

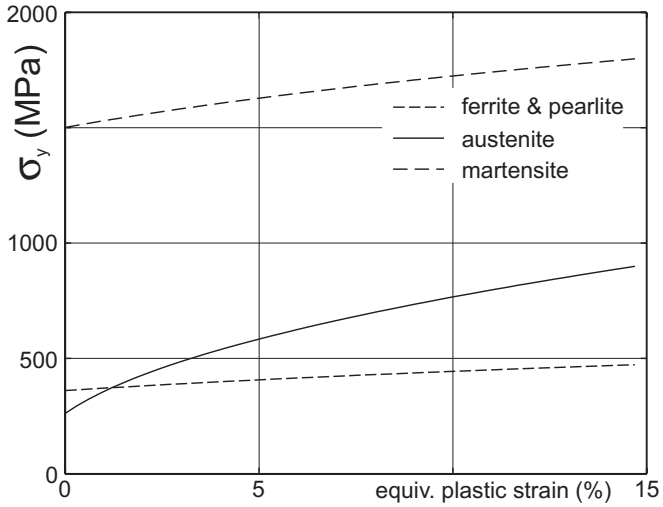

Figure A.1: The stress strain curves for each phase.

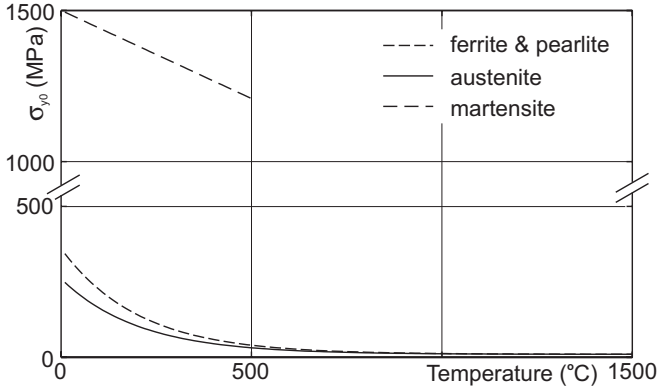

Figure A.2: The initial yield stress as a function of the temperature.

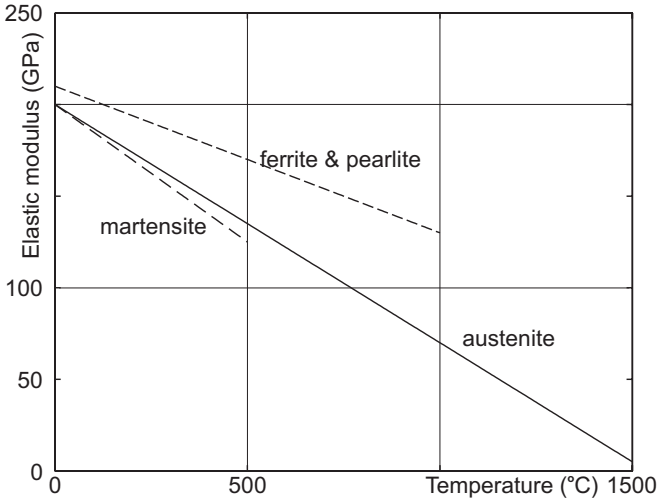

Figure A.3: The modulus of elasticity as a function of the temperature.

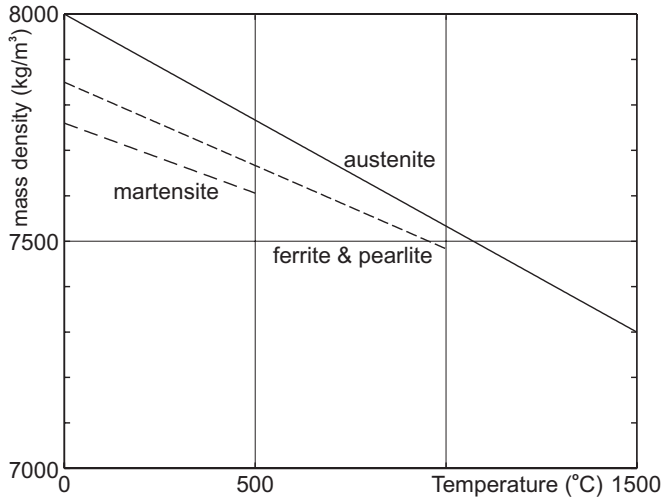

Figure A.4: The mass density as a function of the temperature.

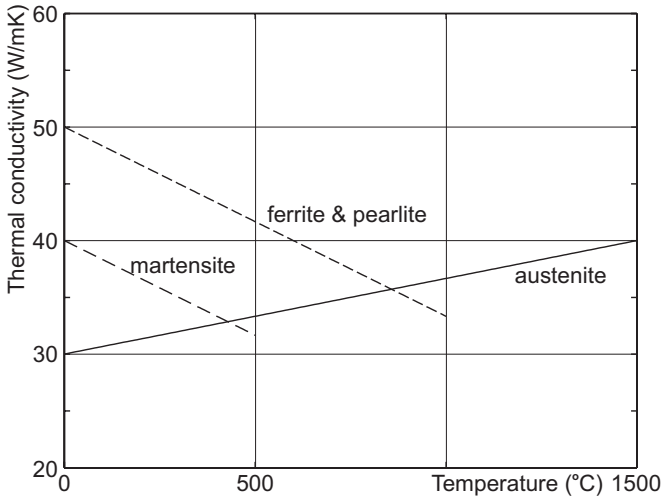

Figure A.5: The thermal conductivity as a function of the temperature.

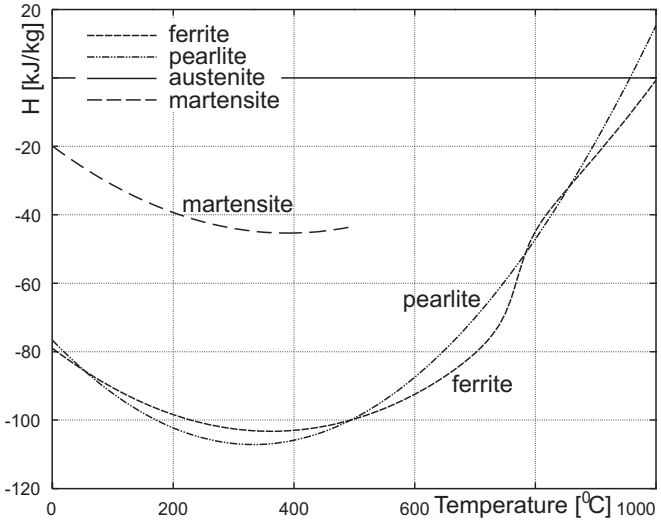

Figure A.6: The enthalpy per phase with respect to austenite.

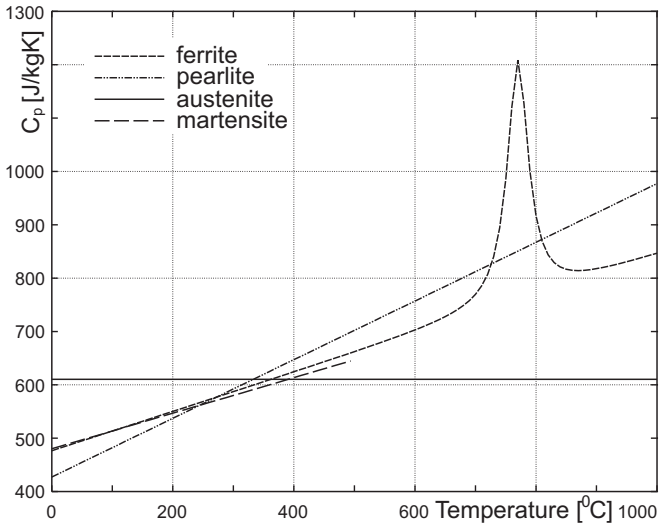

Figure A.7: Specific heat per phase.

Kinetics	
Martensite	T_{Ms0} = 355 °C
	$\beta = 0.011$
stress modification	A_{M} = 1.25 10^{-}6 K/Pa
	B_{M} = 0.75 10^{-}6 K/Pa
Pearlite	Figure B.5
	$n^{\alpha} = 3.5$
	$n^{\mathrm{p}} = 1.1$
stress modification	A_{τ} = 0.02 10^{-}6 s/Pa
	B_{τ} = 0.06 10^{-}6 s/Pa
Austenite	Figure B.7
	$n^{\gamma} = 2.5$ (pearlite to austenite)
	$n^{\gamma} = 1.0$ (ferrite to austenite)
stress modification	-
Transformation plasticity	
Martensite	K = 0.0075
Pearlite	K = 0.0150
Austenite	-

B. Estimation of Isothermal Transformation Curves from Continuous Transformation Data

B.1 Introduction

Transformation data are generally presented in two types of diagrams, isothermal TTT diagrams and continuous cooling (or heating) diagrams (CCT or TTA diagrams). After choosing an appropriate kinetic model for the description of the transformation, the parameters can be obtained from the TTT diagrams. When these parameters are used in the equations from Section B.2, the accuracy can be checked by simulations of for example continuous cooling and comparison of the results with the available continuous cooling diagrams. A calculation for cooling of Ck45 is shown in Figure B.1 . It turns out that the reaction rates are grossly underestimated.

For the calculations of hardening it may be argued that the data as obtained during continuous cooling are more relevant since these represent more closely the actual process. Therefore we need a method to extract the parameters from CCT diagrams rather than from TTT diagrams. The objective of this section is to develop this method. The overall objective of this work is to simulate phase transformations. This is done based on the additivity principle, regardless of whether it applies or not. This is also reflected in this section. The parameter extraction method is based on application of the additivity principle without questioning its validity. The benefit of this apparent simplification is that the extraction method is consistent with the simulation model.

First a general equation is derived. Next, this equation is applied to the ferrite-pearlite reaction during cooling of Ck45 steel.

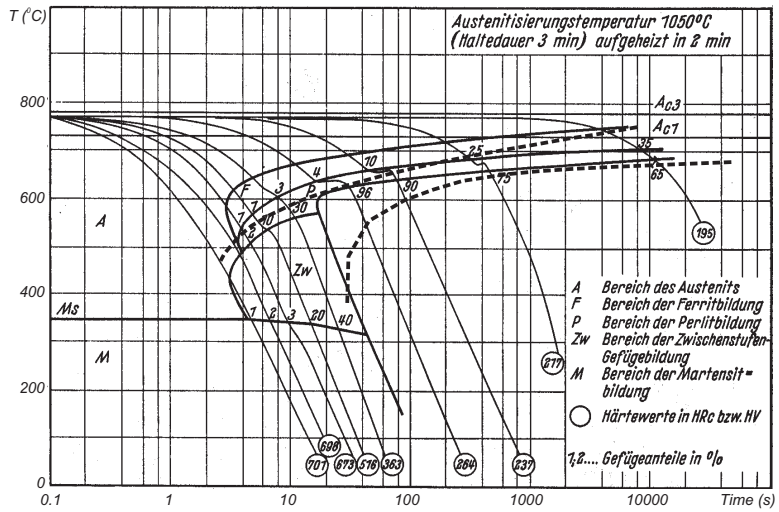

Figure B.1: Continuous cooling diagram diagram simulated with data from TTT diagram (dashed lines), overlayed on the corresponding CCT diagram. Data obtained from Wever and Rose (1961).

B.2 Kinetic models

The transformation proceeds via nucleation and subsequent growth. While the first nuclei start growing, more nuclei appear at other locations. The kinetics shows three phases, initial nucleation, growth of the first nuclei with steady nucleation and finally site saturation and impingement of the growing grains with a retardation of the growth. Different mathematical models have been proposed to describe the transformation kinetics. The fraction transformed φ is initially:

$$\varphi = kt^n \qquad \text{or alternatively: } \varphi = \left(\frac{t}{\tau}\right)^n \tag{B.1}$$

Here n is the Avrami exponent and τ is a time constant. The value of n depends on the ratio of nucleation rate and growth rate. Rather than an Avrami coefficient k with an awkward dimension ($time^{-n}$) it is preferable to use the time constant τ. Its value depends on the absolute values of both nucleation and growth rates. Both n and τ are functions of the temperature T. With proceeding transformation the available nucleation volume becomes exhausted. Also retardation due to impingement of growing crystals occurs. This is described by relating the growth to the amount of virgin material left $(1-\varphi)$. This results in a general rate equation:

$$\dot{\varphi} = (1-\varphi)^r \, \frac{n}{\tau} \left(\frac{t}{\tau}\right)^{n-1} \tag{B.2}$$

The saturation exponent r depends on the growth mode (lineal, planar, spherical). In general it is also temperature dependent. Choosing $r = 1$ the Avrami equation is obtained (Avrami, 1939, 1940), $r = 2$ leads to the Austin and Rickett (1939) equation. Other choices for r are also possible.

When Equation (B.2) is appropriately integrated the equation for phase changes by nucleation and growth is obtained (Fig. B.2):

$$\begin{array}{lll} r = 1: & \varphi(t) = 1 - \mathrm{e}^{-(t/\tau)^n} & \text{(Avrami)} \\ r = 2: & \varphi(t) = 1 - \frac{1}{1+(t/\tau)^n} & \text{(Austin-Rickett)} \\ r \neq 1: & \varphi(t) = 1 - \frac{1}{\sqrt[r-1]{1+(r-1)(t/\tau)^n}} & \end{array} \tag{B.3}$$

These equations have been derived for isothermal phase change. To describe non-isothermal processes, we can not rely on a function $\varphi(t, T)$. Rather a form has to be used, which relates the phase change rate to the instantaneous state. Assuming that the additivity principle holds (Cahn, 1956) a rate equation may be used of the form:

$$\dot{\varphi} = \dot{\varphi}(\varphi, T) \tag{B.4}$$

After elimination of the time from Eqs. (B.2) and (B.3) the following rate equations are derived:

$$\begin{array}{ll} \dot{\varphi} = (1-\varphi)\frac{n}{\tau}\,(-\ln(1-\varphi))^{\frac{n-1}{n}} & \text{Avrami} \\ \dot{\varphi} = (1-\varphi)^{\frac{n+1}{n}}\,\frac{n}{\tau}\varphi^{\frac{n-1}{n}} & \text{Austin-Rickett} \\ \dot{\varphi} = (1-\varphi)^{\frac{r+n-1}{n}}\,\frac{n}{\tau}\left(\frac{(1-\varphi)^{(r-1)}-1}{1-r}\right)^{\frac{n-1}{n}} & r \neq 1 \end{array} \tag{B.5}$$

By applying a Taylor expansion to the last factor of each of these expressions an approximate rate equation is obtained, which is simple, applicable to all values of r and remarkably accurate (Starink, 1997):

$$\dot{\varphi} \approx (1-\varphi)^{\frac{r+n-1}{n}} \frac{n}{\tau} \varphi^{\frac{n-1}{n}} \tag{B.6}$$

In the case that the transformation starts from a non-zero fraction φ_0 and saturates to an equilibrium fraction $\bar{\varphi}$ not equal to one, in stead of φ must be substituted $(\varphi-\varphi_0)/(\bar{\varphi}-\varphi_0)$. This yields:

$$\dot{\varphi} \approx \left(\frac{\bar{\varphi}-\varphi}{\bar{\varphi}-\varphi_0}\right)^{\frac{r+n-1}{n}} \frac{n}{\tau} \left(\frac{\varphi-\varphi_0}{\bar{\varphi}-\varphi_0}\right)^{\frac{n-1}{n}} \tag{B.7}$$

When both n and r are constants the transformation rate only depends on the time constant τ. The transformation is then said to be iso-kinetic. It will be shown that in that case τ can be analytically determined from continuous cooling tests.

B.3 Estimation of time constants

During isothermal transformation, $\tau_1(T)$ is the time needed to produce a certain proportion φ_1. In a TTT diagram it may be the curve indicating the start of a reaction, the end of the reaction or any constant phase fraction curve in between. It is a constant fraction of the time constant τ in the evolution equation (B.3).

The additivity rule (Cahn, 1956; Leblond and Devaux, 1984) states that in an non-isothermal iso-kinetic process this same portion is obtained when a time t_1 has passed, such that:

$$\int_0^{t_1} \frac{\mathrm{d}t}{\tau_1(T)} = 1 \tag{B.8}$$

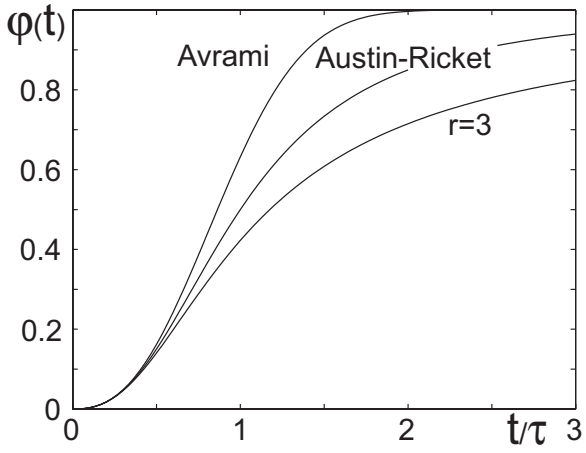

Figure B.2: Sigmoidal curves according to Equation (B.3)

Transformations are studied using continuous cooling or heating tests. The results are presented in e.g. Continuous Cooling Transformation (CCT) diagrams. If we pick one particular event then (B.8) holds for the corresponding time constant. When the temperature rate is constant the time and the temperature are related:

$$\mathrm{d}t = \frac{\mathrm{d}T}{c} \tag{B.9}$$

Here c is the temperature rate. When positive, c is the heating rate, when negative, it is the cooling rate. Assume, for the time being, a positive c. Substitution into Equation (B.8) yields:

$$\int_0^{t_1} \frac{\mathrm{d}t}{\tau_1(T)} = \frac{1}{c}\int_{T_0}^{T_1} \frac{\mathrm{d}T}{\tau_1(T)} = 1 \tag{B.10}$$

From the continuous heating or cooling diagram the temperature T_1, at which the considered event has happened can be established as a function of c: $T_1(c)$. For a small variation $\mathrm{d}c$ in the temperature rate c, the considered event will happen at a slightly different temperature $T_1 + \mathrm{d}T_1$. This is reflected in the additivity principle:

$$\frac{1}{c+\mathrm{d}c}\int_{T_0}^{T_1+\mathrm{d}T_1} \frac{\mathrm{d}T}{\tau_1(T)} = 1 \tag{B.11}$$

When we use Equation (B.10) we derive:

$$\begin{aligned} \frac{1}{c+\mathrm{d}c}\int_{T_0}^{T_1} \frac{\mathrm{d}T}{\tau_1(T)} + \frac{1}{c+\mathrm{d}c}\int_{T_1}^{T_1+\mathrm{d}T_1} \frac{\mathrm{d}T}{\tau_1(T)} &\approx \\ \frac{c}{c+\mathrm{d}c} + \frac{1}{c+\mathrm{d}c}\frac{\mathrm{d}T_1}{\tau_1(T_1)} &= 1 \\ \frac{\mathrm{d}T_1}{\tau_1(T_1)} &= \mathrm{d}c \end{aligned} \tag{B.12}$$

From this follows the expression for $\tau_1(T)$:

$$\tau_1 = \frac{\mathrm{d}T_1}{\mathrm{d}c} \tag{B.13}$$

It is easily verified that this equation also applies to continuous cooling. When c is negative, a positive $\mathrm{d}c$ just means slightly slower cooling.

B.4 Austenite-pearlite reaction

A close look at e.g. the cooling diagram in Figure B.6 and the equilibrium diagram in Figure 2.1 reveals some complexities which have to be dealt with when (B.13) is applied to the ferrite-pearlite reaction. The model for simulation of ferrite and pearlite formation is described in Chapter 2. Important events, which are easily discernible in a CCT diagram, are the start of the ferrite formation and the end of the pearlite transformation. So when dealing with ferrite τ_1^{α} is the time constant for the start of ferrite formation, whereas τ_2^{p} is the time constant for the completion of the pearlite transformation.

B.4.1 ferrite formation

First of all, between the A_1 and A_3 temperatures the equilibrium fractions of ferrite and austenite are not constant. The contribution between T_{A1} and T_{A3} to the integral in (B.8) depends on the cooling rate in a similar way as the contributions of the other temperature intervals so the result of (B.13) does not change as long as T_1 is not between A_1 and A_3.

T_1 between A_1 and A_3

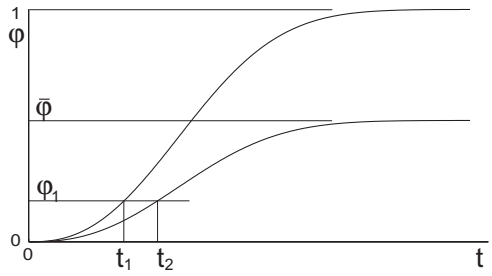

Figure B.3: The relation between t_1 and t_2.

Between the A_1 and A_3 temperatures the equilibrium fractions of ferrite and austenite are not constant. As a consequence during an isothermal transformation test the transformation will eventually produce the equilibrium fraction $\bar{\varphi}^\alpha < \bar{\varphi}_0^\alpha$. This also means that in order to obtain the reference quantity φ_1^α the time required is longer than τ_1^α, say τ_2^α. The ratio $\bar{r} = \tau_2^\alpha / \tau_1^\alpha$ is a function of temperature (see Figure B.3). Following (B.10) the amount φ_1^α is now produced when:

$$\frac{-1}{c}\int_{T_1}^{T_{A3}} \frac{\mathrm{d}T}{\tau_2^\alpha(T)} = \frac{-1}{c\bar{r}(T_1)}\int_{T_1}^{T_{A3}} \frac{\mathrm{d}T}{\tau_1^\alpha(T)} = 1 \tag{B.14}$$

Applying again a small variation $\mathrm{d}c$ to the temperature rate c, we find:

$$\frac{-1}{(c+\mathrm{d}c)(\bar{r}(T_1) + \frac{\mathrm{d}\bar{r}}{\mathrm{d}T_1}\mathrm{d}T_1)}\int_{T_1+\mathrm{d}T_1}^{T_{A3}} \frac{\mathrm{d}T}{\tau_1^\alpha(T)} = 1 \tag{B.15}$$

After some manipulations an expression for $\tau_1^\alpha(T)$ follows:

$$\tau_1^\alpha = \frac{\mathrm{d}T_1}{\mathrm{d}(c\bar{r})} \tag{B.16}$$

B.4.2 pearlite formation

The model as described in Chapter 2 ensures that pearlite formation always follows ferrite formation. To this end the reaction rate of pearlite is linked to the instantaneous ferrite fraction. The idea behind this is that the carbon, which is present in the undercooled

austenite is needed for the formation of pearlite. The pearlite formation is retarded by the presence of undercooled austenite. This is schematically shown in Figure B.4

According to (2.10) the pearlite reaction rate is lowered by a fraction $\varphi^\alpha/\bar{\varphi}_0^\alpha$. This can be incorporated into the additivity principle:

$$\frac{-1}{c}\left(\frac{1}{\bar{\varphi}_0^\alpha}\int_{T_e^\alpha}^{T_{A1}}\varphi^\alpha\frac{\mathrm{d}T}{\tau_2^p(T)}+\int_{T_2}^{T_e^\alpha}\frac{\mathrm{d}T}{\tau_2^p(T)}\right)=1 \tag{B.17}$$

Here T_e^α is the temperature at which the ferrite transformation is completed. Again this equation is perturbed to find the relation between c and T_1:

$$\frac{-1}{c+\mathrm{d}c}\left(\frac{1}{\bar{\varphi}_0^\alpha}\int_{T_e^\alpha+\mathrm{d}T_e^\alpha}^{T_{A1}}(\varphi^\alpha+\mathrm{d}\varphi^\alpha)\frac{\mathrm{d}T}{\tau_2^p(T)}+\int_{T_2+\mathrm{d}T_2}^{T_e^\alpha+\mathrm{d}T_e^\alpha}\frac{\mathrm{d}T}{\tau_2^p(T)}\right)=1 \tag{B.18}$$

After some algebraic manipulation we obtain:

$$\frac{-1}{\bar{\varphi}_0^\alpha}\int_{T_e^\alpha}^{T_{A1}}\frac{\mathrm{d}\varphi^\alpha}{\tau_2^p(T)}\mathrm{d}T+\frac{\mathrm{d}T_2}{\tau_2^p(T_2)}=\mathrm{d}c \tag{B.19}$$

Which gives as an expression for $\tau_2^p(T_2)$:

$$\tau_2^p=\frac{\mathrm{d}T_2}{\mathrm{d}c+\frac{1}{\bar{\varphi}_0^\alpha}\int_{T_e^\alpha}^{T_{A1}}\frac{\mathrm{d}\varphi^\alpha}{\tau_2^p}\mathrm{d}T} \tag{B.20}$$

This equation lacks the elegance of the Equations (B.13) and (B.16). To solve for τ^p first Equation (B.20) is evaluated without the integral accounting for the ferrite under cooling. This estimate is then used to evaluate the integral and iteratively better estimates for τ^p are obtained. After two iterations already sufficiently accurate estimates are obtained.

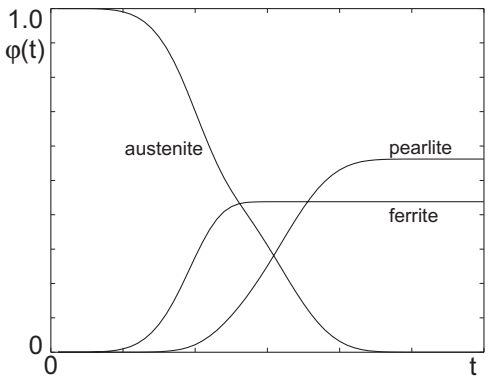

Figure B.4: The pearlite formation slowed down by incomplete ferrite transformation

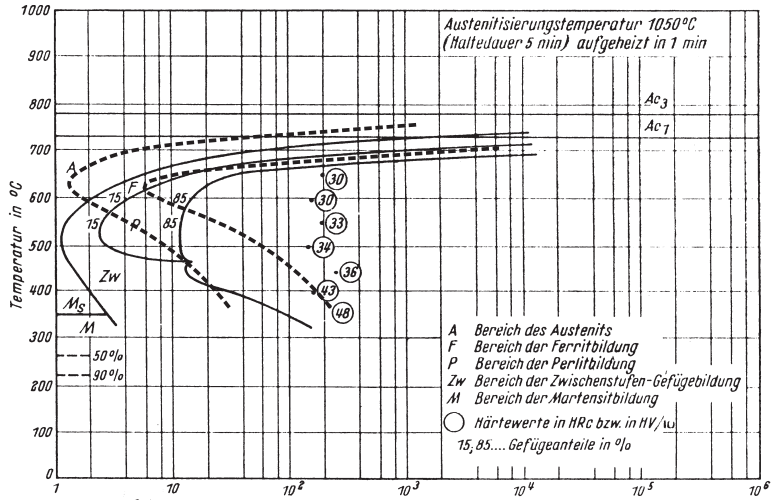

Figure B.5: Isothermal TTT diagram as estimated from CCT diagram (dashed lines) compared with literature data (Wever and Rose, 1961).

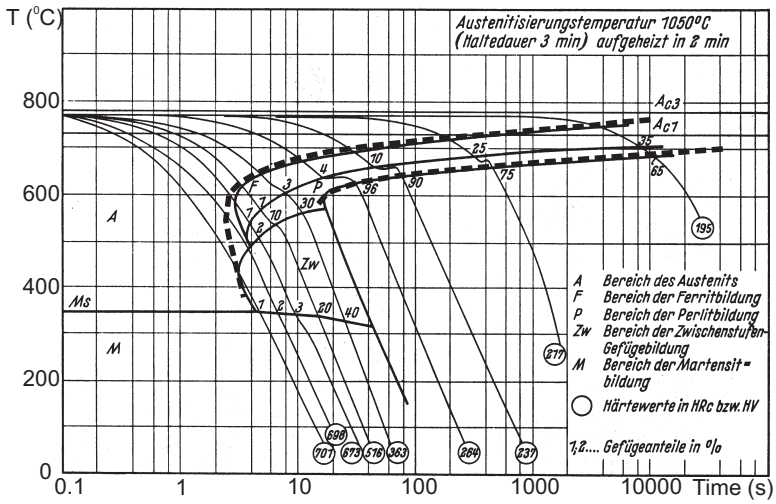

Figure B.6: Comparison of simulated cooling diagram with literature data (Wever and Rose, 1961).

B.5 Continuous cooling curves (CCT)

Time constants for the austenite-pearlite transformation of Ck45 are estimated from Figure B.6. These data are again used to simulate continuous cooling.

In Figure B.5 the TTT diagram as simulated using the estimated time constants is shown

overlayed on the data from Wever and Rose (1961). The difference is quite big. The nose of the reaction is projected at approximately 100 degrees higher temperature than experiments indicate.

The simulated cooling CCT diagram is shown in Figure B.6. The predictions of ferrite-start as well as pearlite-completion temperatures are very accurate.

The relative amounts of ferrite and pearlite after cooling depend on the cooling rate Krielaart (1995). This effect is not predicted at all. The overall reaction times compare very well so that in the end the final martensite contents will be predicted with sufficient accuracy.

B.6 Continuous heating curves (TTA)

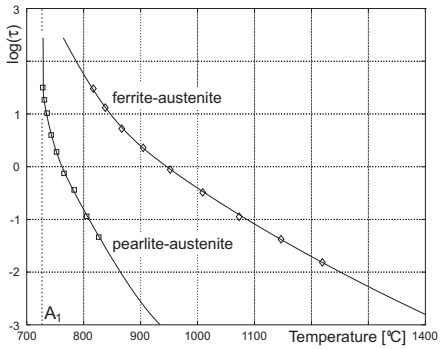

Figure B.7: Time constants for austenization based on literature data (Orlich *et al.*, 1973).

The procedure of this section has also been applied to the continuous heating austenization diagrams as given in Orlich *et al.* (1973). The time constants are shown in Figure B.7. The results of a simulation are shown in Figure B.8.

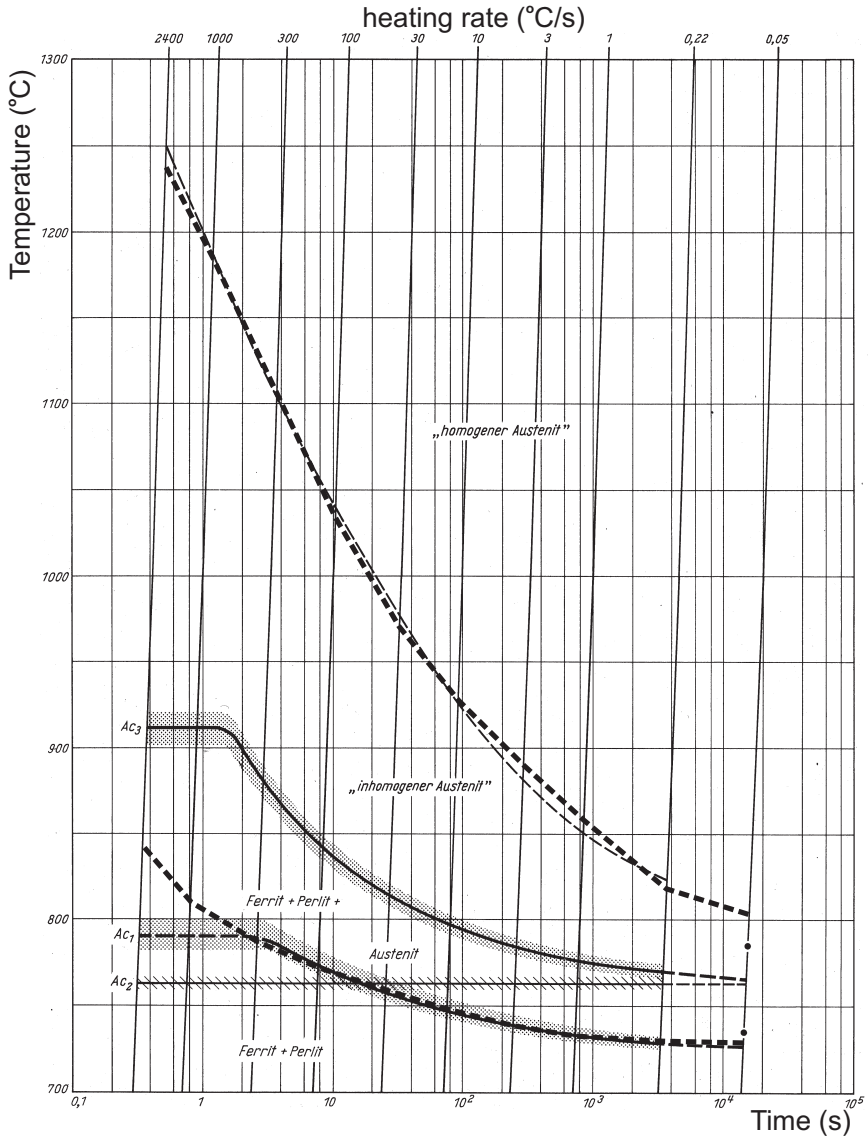

Figure B.8: Comparison of simulated austenization diagram (dashed lines) with literature data (Orlich *et al.*, 1973).

C. A Ductile Matrix with Rigid Inclusions

C.1 Introduction

In this section an estimate is given of the yield stress of a compound of a ductile matrix with rigid inclusions. The inclusions are a model of the hard martensite phase in the ductile austenite. The compound yield stress is calculated by first estimating the strain concentration in the soft phase. Next, the plastic dissipation is estimated under the assumption of ideal plastic behaviour of the soft phase.

Consider a control volume with one inclusion such that the volume ratio of inclusion and total volume equals the volume fraction of the rigid phase. The volume is a cube with dimensions 1. The inclusion is also a cube, but with dimensions a, where $a << 1$. The volume phase fraction of the inclusion φ and a are then related by $\varphi = a^3$. The model is shown in Figure C.1.

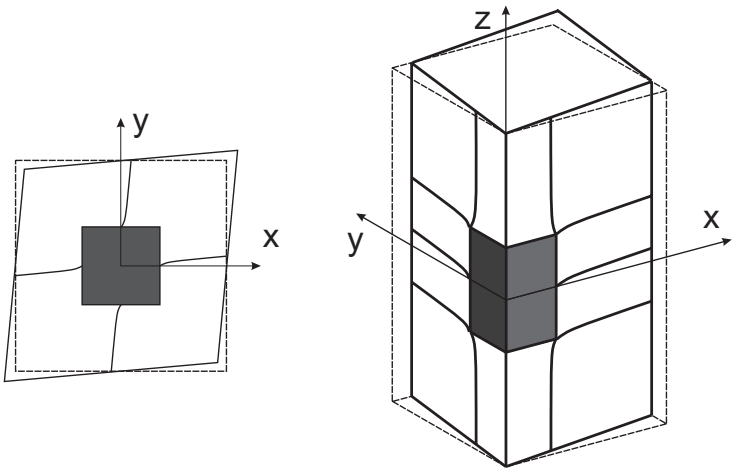

Figure C.1: A rigid inclusion in a ductile matrix

C.2 Deformations

Assume a far field displacement field:

$$\begin{aligned} u(x,y,z) &= \varepsilon_{xy} y \\ v(x,y,z) &= \varepsilon_{xy} x \\ w(x,y,z) &= 0 \end{aligned} \tag{C.1}$$

This gives an overall shear deformation $\gamma_{xy} = 2\varepsilon_{xy}$ of the compound. Now calculate the average shear strains $\bar{\gamma}_{ij}^{(\mathrm{m})}$ in the matrix using the divergence theorem:

$$\begin{aligned}
\int_{V^{(\mathrm{m})}} \gamma_{xy}\,\mathrm{d}V = (1-\varphi)\bar{\gamma}_{xy}^{(\mathrm{m})} &= \int_V \frac{\partial u}{\partial y} + \frac{\partial v}{\partial x}\,\mathrm{d}V = \int_S u n_y + v n_x \,dS \\
\int_{V^{(\mathrm{m})}} \gamma_{yz}\,\mathrm{d}V = (1-\varphi)\bar{\gamma}_{yz}^{(\mathrm{m})} &= \int_V \frac{\partial v}{\partial z} + \frac{\partial w}{\partial y}\,\mathrm{d}V = \int_S v n_z \,dS \\
\int_{V^{(\mathrm{m})}} \gamma_{zx}\,\mathrm{d}V = (1-\varphi)\bar{\gamma}_{zx}^{(\mathrm{m})} &= \int_V \frac{\partial w}{\partial x} + \frac{\partial u}{\partial z}\,\mathrm{d}V = \int_S u n_z \,dS
\end{aligned} \tag{C.2}$$

Here n_x, n_y and n_z are the components of the normal on the bounding surface of the control volume. Evaluation yields the so called self consistent strain relations:

$$\begin{aligned}
\bar{\gamma}_{xy}^{(\mathrm{m})} &= \gamma_{xy}/(1-\varphi) \\
\bar{\gamma}_{yz}^{(\mathrm{m})} &= 0 \\
\bar{\gamma}_{zx}^{(\mathrm{m})} &= 0
\end{aligned} \tag{C.3}$$

The average yz and zx shears in the matrix equal zero. As may be apparent from Figure C.1 this is due to shear strain components on opposite sides of the inclusion which cancel out. To calculate the dissipation these shears will be multiplied by stresses having the same direction. Locally $\tau_{ij}\varepsilon_{ij}$ is positive. Although opposite in sign, all shears add to the dissipation.

The integration for the average off-axis (not aligned with γ_{xy}) components is done over an eighth of the volume. Choose the octant where $\gamma_{yz} > 0$.

$$\frac{1}{8}\int_{V^{(\mathrm{m})}} |\gamma_{yz}|\,\mathrm{d}V = \frac{1}{8}(1-\varphi)|\bar{\gamma}_{yz}^{(\mathrm{m})}| = \int_{S/8} v n_z \,\mathrm{d}S \tag{C.4}$$

where "$S/8$" is the bounding surface of the octant $V/8$. This integral only has to be evaluated over the top ($n_z = 1$) surface S_{top} and the middle surface S_{mid} ($z = 0$). For the top surface follows:

$$\int_{S_{\mathrm{top}}/4} v n_z \,\mathrm{d}S = \int_0^{\frac{1}{2}}\int_0^{\frac{1}{2}} \varepsilon_{xy} x \,\mathrm{d}x\,\mathrm{d}y = \frac{1}{16}\varepsilon_{xy} \tag{C.5}$$

For the middle surface we assume that the displacement field in the matrix equals $v(x, y) = \varepsilon_{xy}x$ except for a thin boundary layer next to the inclusion. This yields an approximate expression for the integral over the middle surface:

$$\int_{(S_{\mathrm{mid}}-a^2)/4} v n_z \,\mathrm{d}S = -\int_{\frac{a}{2}}^{\frac{1}{2}}\int_{\frac{a}{2}}^{\frac{1}{2}} \varepsilon_{xy} x \,\mathrm{d}x\,\mathrm{d}y = -\frac{1}{16}(1-a^3)\varepsilon_{xy} \tag{C.6}$$

So the result is:

$$\int_{V^{(\mathrm{m})}} |\gamma_{yz}| \, \mathrm{d}V = \frac{1}{2} a^3 \varepsilon_{xy} = \frac{1}{2} \varphi \varepsilon_{xy} = \frac{1}{4} \varphi \gamma_{xy} \tag{C.7}$$

This also applies to the zx shear. From this follows that an overall shear strain γ_{xy} causes an average strain $\bar{\gamma}_{xy}$ in the matrix:

$$\bar{\gamma}_{xy}^{(\mathrm{m})} = \frac{\gamma_{xy}}{1 - \varphi} \tag{C.8}$$

and secondary off-axis strains γ_{yz} and γ_{zx} such that:

$$\begin{aligned} |\bar{\gamma}_{yz}^{(\mathrm{m})}| &= \frac{\varphi \gamma_{xy}}{4(1 - \varphi)} \\ |\bar{\gamma}_{zx}^{(\mathrm{m})}| &= \frac{\varphi \gamma_{xy}}{4(1 - \varphi)} \end{aligned} \tag{C.9}$$

C.3 Overall yield stress

To determine the yield stress of the compound the work done by the external load is set equal to the dissipation by the internal stresses. In particular for our control volume this means:

$$\bar{\tau}_{\mathrm{yld}} \, \mathrm{d}\gamma_{xy} = (1 - \varphi) \tau_{\mathrm{yld}}^{(\mathrm{m})} \, \mathrm{d}\bar{\gamma}_{\mathrm{eff}}^{(\mathrm{m})} \tag{C.10}$$

To obtain an estimate of the effective average shear $\bar{\gamma}_{\mathrm{eff}}^{(\mathrm{m})}$ observe that the additional $\gamma_{xy}^{(\mathrm{m})}$ is active on the $n_x = \pm 1$ and $n_y = \pm 1$ faces of the inclusion, whereas the components $\gamma_{yz}^{(\mathrm{m})}$ and $\gamma_{zx}^{(\mathrm{m})}$ are concentrated on the $n_z = \pm 1$ faces. The action of the γ_{xy} is uncoupled from that of the other two. To account for the effect of $\gamma_{yz}^{(\mathrm{m})}$ and $\gamma_{zx}^{(\mathrm{m})}$ the effective shear strain $\gamma_{\mathrm{eff}}^{(\mathrm{m})}$ is estimated.

$$\gamma_{\mathrm{eff}}^{(\mathrm{m})} = \sqrt{(\gamma_{yz}^{(\mathrm{m})})^2 + (\gamma_{zx}^{(\mathrm{m})})^2} \tag{C.11}$$

Linearly varying distributions are assumed on the $n_z = \pm 1$ faces of the inclusion:

$$\begin{aligned} \gamma_{yz}^{(\mathrm{m})}(x, y) &= n_z \varphi \varepsilon_{xy} x \\ \gamma_{zx}^{(\mathrm{m})}(x, y) &= n_z \varphi \varepsilon_{xy} y \end{aligned} \tag{C.12}$$

Then the total amount of the effective strain at these faces is

$$2\varepsilon_{xy} \int_{-\frac{a}{2}}^{\frac{a}{2}} \int_{-\frac{a}{2}}^{\frac{a}{2}} \sqrt{x^2 + y^2} \, \mathrm{d}x \, \mathrm{d}y = 0.765 \varphi \varepsilon_{xy} = 0.383 \varphi \gamma_{xy} \tag{C.13}$$

So the average effective strain in the matrix totals

$$\bar{\gamma}_{\mathrm{eff}}^{(\mathrm{m})} = \frac{\gamma_{xy}}{1 - \varphi} (1 + 0.383\varphi) \tag{C.14}$$

Assume that $\mathrm{d}\bar{\gamma}_{\mathrm{eff}}^{(\mathrm{m})} / \mathrm{d}\gamma_{xy} = \bar{\gamma}_{\mathrm{eff}}^{(\mathrm{m})} / \gamma_{xy}$. Substitution into (C.10) yields the effective yield stress of the compound:

$$\bar{\tau}_{\mathrm{yld}} = (1 + 0.383\varphi) \tau_{\mathrm{yld}}^{(\mathrm{m})} \tag{C.15}$$

C.4 Application to austenite-martensite mixture

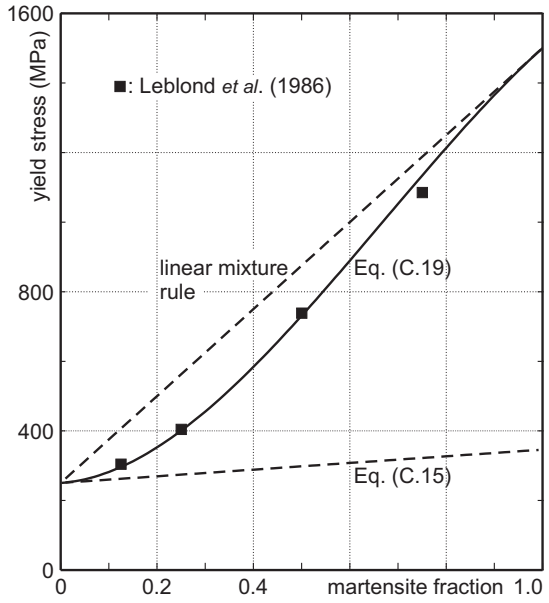

Figure C.2: Yield stress of an austenite-martensite mixture ($\sigma_y^\gamma = 250$ MPa, $\sigma_y^m = 1500$ MPa) and comparison with FE results by Leblond *et al.* (1986)

For the yield stress of the mixture of austenite and martensite an expression is desired of the form:

$$\sigma_y = \varphi^\gamma \sigma_y^\gamma + f(\varphi^m)\sigma_y^m \tag{C.16}$$

Equation (C.15) is valid for small values of φ. Initially the compound yield stress is independent of the yield stress of the hard phase.

$$f(0) = 0 \quad \text{and} \quad f'(0) = 0.383\frac{\sigma_y^\gamma}{\sigma_y^m} \tag{C.17}$$

When growing, the martensite will eventually become the dominant phase and the yield stress is described by a linear mixture law.

$$f(1) = 1 \quad \text{and} \quad f'(1) = 1 \tag{C.18}$$

This is achieved by using for $f(\varphi^m)$ a polynomial function:

$$f(\varphi^m) = \varphi^m(C + 2(1-C)\varphi^m - (1-C)(\varphi^m)^2)$$
$$\text{where: } C = 1.383\frac{\sigma_y^\gamma}{\sigma_y^m} \tag{C.19}$$

This result is illustrated in Figure C.2 for a mixture of austenite with yield stress 250 MPa and martensite with yield stress 1500 MPa.

Bibliography

Abbasi, F. and A. J. Fletcher (1985), Effect of transformation plasticity on generation of thermal stress and strain in quenched steel plates, *Mat. Sci. Techn.*, vol. 1, pp. 830–837.

Aeby-Gautier, E. (1985), *Transformations Perlitique et Martensitique sous Contrainte de Traction dans les Aciers*, Ph.D. thesis, Institut National Polytechnique de Lorraine.

Ashby, M. F. and K. E. Easterling (1984), The transformation hardening of steel surfaces by laser beams I: hypo-eutectoid steels, *Acta Metall.*, vol. 32, pp. 1935–1948.

Austin, J. B. and R. L. Rickett (1939), *Trans. AIME*, vol. 135, p. 396.

Avrami, M. (1939), Kinetics of phase change, I, general theory, *J. Chem. Phys.*, vol. 7, pp. 1103–1112.

Avrami, M. (1940), Kinetics of phase change, II, transformation-time relations for random distribution of nuclei, *J. Chem. Phys.*, vol. 8, pp. 212–224.

Avrami, M. (1941), Kinetics of phase change, III, granulation, phase change and microstructure, *J. Chem. Phys.*, vol. 9, pp. 177–184.

Balagangadhar, D., G. A. Dorai and D. A. Tortorelli (1999), A displacement-based reference frame formulation for steady-state thermo-elasto-plastic material processes, *Int. J. Solids. Struct.*, vol. 36, pp. 2397–2416.

Balagangadhar, D. and D. A. Tortorelli (2000), Design of large deformation steady elasto-plastic manufacturing processes. part I: a displacement based reference frame formulation, *Int. J. Numer. Meth. Engng.*, vol. 49, pp. 899–932.

Baumann, C. E. and J. T. Oden (1999), A discontinuous hp finite element method for convection-diffusion problems, *Comp. Meth. Appl. Mech. Engng.*, vol. 175, pp. 311–341.

Baumann, C. E. and J. T. Oden (2000), An adaptive order discontinuous Galerkin method for the solution of the euler equations of gas dynamics, *Int. J. Numer. Meth. Engng.*, vol. 47, pp. 61–73.

Benson, D. J. (1989), An efficient, accurate simple ALE method for nonlinear finite element programs, *Comp. Meth. Appl. Mech. Engng.*, vol. 72, pp. 305–350.

Bergheau, J. M., D. Pont and J. B. Leblond (1991), Three-Dimensional simulation of a laser surface treatment through steady state computation in the heat source's comoving frame, in: L. Karlsson, L.-E. Lindgren and M. Jonsson (eds.), *Mechanical Effects of Welding, IUTAM Symposium, Luleå*, Springer Verlag.

Bhattacharyya, S. and G. L. Kehl (1955), Isothermal transformation of austenite under externally applied tensile stress, *Trans ASM*, vol. 47, pp. 351–379.

Boman, R. and J.-P. Ponthot (2001), Numerical simulation of lubricated contact between solids in metal forming processes using the arbitrary Lagrangian Eulerian formulation, in: K. Mori (ed.), *Proceedings of the 7^{th} Int. Conf. Num. Meth. Ind. Forming Proc.*

NUMIFORM 2001, pp. 45–53, A.A. Balkema.

Brooks, A. and T. J. R. Hughes (1982), Streamline upwind Petrov-Galerkin formulations for convection dominated flows with particular emphasis on the incompressible Navier-Stokes equations, *Comp. Meth. Appl. Mech. Engng.*, vol. 32, pp. 199–259.

Cahn, J. W. (1956), Transformation kinetics during continuous cooling, *Acta Metall.*, vol. 4, pp. 572–575.

Chatterjee-Fischer, R., R. Rothe and R. Becker (1984), Überblick über das Härten mit dem Laserstrahl, *Härterei Techn. Mitt.*, vol. 39, pp. 91–98.

Cockburn, B. W. (2001), Devising discontinuous Galerkin methods for non-linear hyperbolic conservation laws, *J. Comp. Appl. Math.*, vol. 128, pp. 187–204.

de Jong, M. and G. W. Rathenau (1961), Mechanical properties of an iron-carbon alloy during allotropic transformations, *Acta Metall.*, vol. 9, pp. 714–720.

de Sampaio, P. A. B. and A. L. G. A. Coutinho (2001), A natural derivation of discontinuity capturing operator for advection-diffusion problems, *Comp. Meth. Appl. Mech. Engng.*, vol. 190, pp. 6291–6308.

Denis, S., E. Gautier, A. Simon and G. Beck (1985), Stress-phase-transformation interactions - basic principles, modelling and calculation of internal stresses, *Mat. Sci. Techn.*, vol. 1, pp. 805–814.

Denis, S. and A. Simon (1986), Discussion on the the role of transformation plasticity in the calculation of quench stresses in steel, in: E. Macherauch and V. Hauk (eds.), *Residual Stresses in Science and Technology*, pp. 565–572.

Denis, S., S. Sjöström and A. Simon (1987), Coupled temperature, stress, phase transformation calculation model numerical illustration of the internal stress evolution during cooling of a eutectoid steel cylinder, *Metall. Trans. A*, vol. 18A, pp. 1203–1212.

Donea, J. (1984), A Taylor-Galerkin method for convective transport problems, *Int. J. Numer. Meth. Engng.*, vol. 20, pp. 101–119.

Estrin, Y. (1998), Dislocation theory based constitutive modelling: foundations and applications, *J. Mat. Proc. Techn.*, vol. 80-81, pp. 33–39.

Farias, D., S. Denis and A. Simon (1990), Modelling of phase transformations during fast heating and cooling in steels, *Key Engineering Materials*, vol. 46 & 47, pp. 139–152.

Fischer, F. D., G. Reisner, E. Werner, K. Tanaka, G. Cailletaud and T. Antretter (2000), A new view on transformation induced plasticity (TRIP), *Int. J. Plast.*, vol. 16, pp. 723–748.

Fischer, F. D., Q. P. Sun and K. Tanaka (1996), Transformation-induced plasticity (TRIP), *Appl. Mech. Rev.*, vol. 49, pp. 317–364.

Fortin, M. and A. Fortin (1989), A new approach for the FEM simulation of viscoelasic flows, *J. Non-Newt. Fluid Mech.*, vol. 32, pp. 295–310.

Ganghoffer, J. F., S. Denis, E. Gautier, A. Simon, K. Simonsson and S. Sjöström (1991), Micromechanical simulation of martensitic transformation by finite elements, *J. Phys. I*, vol. C4, pp. 77–82.

Ganghoffer, J. F., S. Denis, E. Gautier and S. Sjöström (1997), Micromechanical analysis of the finite element calculation of a diffusional transformation, *J. Mat. Sci.*, vol. 32, pp. 4941–4955.

Geijselaers, H. J. M. and J. Huétink (2000), Semi implicit second order discontinuous Galerkin convection for ALE calculations, in: E. Oñate (ed.), *ECCOMAS 2000*, p. 649, CIMNE, Barcelona.

Geijselaers, H. J. M., Y. Yu and J. Huétink (2001), Simulation of steady state laser hardening, in: K. Mori (ed.), *Proceedings of the 7^{th} Int. Conf. Num. Meth. Ind. Forming Proc. NUMIFORM 2001*, pp. 45–53, A.A. Balkema.

Greenwood, G. W. and R. H. Johnson (1965), The deformation of metals under small stresses during phase transformations, *Proc. Roy. Soc.*, vol. 283A, pp. 403–422.

Gu, M. and J. A. Goldak (1994), Steady-state formulation for stress and distortion of welds, *J. Engng. Indust.*, vol. 116, pp. 467–474.

Gür, C. H. and A. E. Tekkaya (1996), Finite element simulation of quench hardening, *Steel Res.*, vol. 7, pp. 298–306.

Hacquin, A., P. Montmitonnet and J.-P. Guillerault (1996), A steady state thermo-elastoviscoplastic finite element model of rolling with coupled thermo-elastic roll deformation, *J. Mat. Proc. Techn.*, vol. 60, pp. 109–116.

Hildenwall, B. and T. Ericson (1977), Prediction of residual stresses in case hardening steels, in: D. V. Doane and J. S. Kirkaldy (eds.), *Hardenability concepts with application to steel*, pp. 579–606, The Metallurgical Society of the AIME.

Hinton, E. and J. S. Campbell (1974), Local and global smoothing of discontinuous finite element functions using a least squares method, *Int. J. Numer. Meth. Engng.*, vol. 8, pp. 461–480.

Hong, J. K., P. Dong and C. L. Tsai (1998), Application of plasic strain relaxation effect in numerical welding simulation, in: J. M. Vitek, S. A. David, J. A. Johnson, H. B. Smart and T. DebRoy (eds.), *Trends in Welding Research*, pp. 999–1004, ASM International.

Huerta, A., F. Casadei and J. Donea (1995), ALE stress update in transient plasticity problems, in: D. Owen and E. Oñate (eds.), *Computational Plasticity*, pp. 1865–1871.

Huétink, J. (1986), *On the Simulation of Thermomechanical Forming Processes*, Ph.D. thesis, University of Twente.

Huétink, J., L. H. J. F. Beckmann and H. J. M. Geijselaers (1990a), Finite element analysis of laser transformation hardening, in: H. Opower (ed.), *Intl. Congr. Optical Science and Engineering, meeting 1276, CO_2 Lasers and Applications*.

Huétink, J., P. T. Vreede and J. van der Lugt (1990b), Progress in mixed Euler-Lagrange FE simulation of forming processes, *Int. J. Numer. Meth. Engng.*, vol. 30, pp. 1441–1457.

Hulsen, M. A. (1991), The discontinuous Galerkin method with explicit Runge-Kutta time integration for hyperbolic and parabolic systems with source terms, Tech. Rep. MEMT 19, Delft Univ. Techn. Lab. Aero Hydro.

Inoue, T. and B. Raniecki (1978), Determination of thermal-hardening stress in steels by use of thermoplasticity theory, *J. Mech. Phys. Solids*, vol. 26, pp. 187–212.

Koistinen, D. P. and R. E. Marburger (1959), A general equation prescribing the extent of the austenite- martensite transformation in pure iron-carbon alloys and plain carbon steels, *Acta Metall.*, vol. 7, pp. 59–60.

Krielaart, G. P. (1995), *Primary Ferrite Formation from Supersaturated Austenite*, Ph.D. thesis, Delft University of Technology.

Leblond, J. B. and J. Devaux (1984), A new kinetic model for anisothermal metallurgical transformations in steels including effect of austenite grain size, *Acta Metall.*, vol. 32, pp. 137–146.

Leblond, J. B., J. Devaux and J. C. Devaux (1989), Mathematical modelling of transformation plasticity in steels I and II, *Int. J. Plast.*, vol. 5, pp. 551–591.

Leblond, J. B., G. Mottet, J. Devaux and J. C. Devaux (1985), Mathematical models of anisothermal phase transformations in steel and predicted plastic behaviour, *Mat. Sci. Techn.*, vol. 1, pp. 815–822.

Leblond, J. B., G. Mottet and J. C. Deveaux (1986), A theoretical and numerical approach to the plastic behaviour of steels during phase transformations I and II, *J. Mech. Phys. Solids*, vol. 34, pp. 395–432.

Lesaint, P. and P. A. Raviart (1974), On a finite element method for solving the neutron transport equation, in: C. de Boor (ed.), *Mathematical Aspects of Finite Elements in Partial Differential Equations*, pp. 89–123.

Lindgren, L.-E. (2001), Finite element modeling and simulation of welding part 1-3, *J. Therm. Stresses*, vol. 24, pp. 141–231, 305–335.

Liu, C. C., K. F. Yao and Z. Liu (2000a), Quantitative research on effects of stresses and strains on bainitic transformation kinetics and transformation plasticity., *Mat. Sci. Techn.*, vol. 16, pp. 643–647.

Liu, C. C., K. F. Yao, Z. Liu and G. Gao (2000b), Study of the effect of stress and strain on martensite transformation: Kinetics and transformation plasticity, *J. Comp. Aid. Mat. Des.*, vol. 7, pp. 63–69.

Liu, W. K., H. Chang, J. S. Chen and T. Belytschko (1988), Arbitrary Lagrangian-Eulerian Petrov-Galerkin finite elements for nonlinear continua, *Comp. Meth. Appl. Mech. Engng.*, vol. 68, pp. 259–310.

Lomtev, I. and G. E. M. Karniadakis (1999), A discontinuous Galerkin method for the Navier-Stokes equations, *Int. J. Numer. Meth. Fluids*, vol. 29, pp. 587–603.

Oddy, A. S., J. A. Goldak and J. M. J. McDill (1992), Transformation plasticity and residual stresses in single-pass repair welds, *ASME J. Press. Vess. Techn.*, vol. 114, pp. 33–38.

Oddy, A. S., J. M. J. McDill and J. A. Goldak (1990), Consistent strain fields in 3D finite element analysis of welds, *ASME J. Press. Vess. Techn.*, vol. 112, pp. 309–311.

Ohmura, E., K. Inoue and Y. Takamachi (1991), Theoretical analysis of laser transformation hardening of hypoeutectoid steel based on kinetics, *JSME Int. J. ser. I*, vol. 34, pp. 421–429.

Oñate, E. (1998), Derivation of stabilized equations for numerical solution of advective-diffusive transport and fluid flow problems, *Comp. Meth. Appl. Mech. Engng.*, vol. 151, pp. 233–265.

Orlich, J., A. Rose and P. Wiest (1973), *Atlas zur Wärmebehandlung von Stähle, III Zeit Temperatur Austenitisierung Schaubilder*, Verlag Stahleisen MBH, Düsseldorf.

Patel, J. R. and M. Cohen (1953), Criterion for the action of applied stress in the martensitic transformation, *Acta Metall.*, vol. 1, pp. 531–538.

Pichelin, E. and T. Coupez (1998), Finite element solution of the 3D mold filling problem for viscous incompressible fluid, *Comp. Meth. Appl. Mech. Engng.*, vol. 163, pp. 359–371.

Porter, D. A. and K. E. Easterling (1992), *Phase transformations in metals and alloys*, Chapman & Hall, London.

Rammerstorfer, F., D. Fischer, W. Mitter, K. Bathe and M. Snyder (1981), On thermo-elastic-plastic analysis of heat-treatment processes including creep and phase changes, *Comp. & Str.*, vol. 13, pp. 771–779.

Roberts, J. E. and J.-M. Thomas (1991), Mixed and hybrid methods, in: P. G. Ciarlet and J. L. Lions (eds.), *Handbook of Numerical Analysis*, vol. 2, pp. 523–639, North-Holland.

Rodriguez-Ferran, A., A. Agusti-Foguet and A. Huerta (2002), Arbitrary Lagrangian Eulerian (ALE) formulation for hyperelasticity, *Int. J. Numer. Meth. Engng.*, vol. 53, pp. 1831–1851.

Ronda, J. and G. J. Oliver (2000), Consistent thermo-mechano-metallurgical model of welded steel with unified approach to derivation of phase evolution laws and transformation-induced plasticity, *Comp. Meth. Appl. Mech. Engng.*, vol. 189, pp. 361–417.

Ruan, Y. (1999), A steady-state thermomechanical solution of continuously quenched axisymmetric bodies, *ASME J. Appl. Mech.*, vol. 66, pp. 334–339.

Schumann, H. (1979), Dilatationseffekte bei unter äusserer Spannungseinwirkung ablaufender martensitscher $\gamma \rightarrow \varepsilon$ Umwandlung, *Neue Hütte*, vol. 24, pp. 161–166.

Shanghvi, J. Y. and P. Michaleris (2002), Thermo-elasto-plastic finite element analysis of quasi-state processes in Eulerian reference frames, *Int. J. Numer. Meth. Engng.*, vol. 53, pp. 1533–1556.

Siegel, P., R. Mosé and P. Ackerer (1997), Solution of the advection-diffusion equation using a combination of discontinuous and mixed finite elements, *Int. J. Numer. Meth. Fluids*, vol. 24, pp. 595–613.

Simon, A., S. Denis and E. Gautier (1994), Effet des solicitations themomécaniques sur les transformations de phases dans l' état solide. aspects métallurgique et mécanique, *J. Phys. IV*, vol. 4 C3, pp. 199–213.

Sjöström, S. (1985), Interactions and constitutive models for calculating quench stresses in steel, *Mat. Sci. Techn.*, vol. 1, pp. 823–829.

Stähli, G. (1979), Mögligkeiten und Grenzen der Randschicht Kurzzeit Härtung von Stahl, *Härterei Techn. Mitt.*, vol. 32, pp. 55–63.

Starink, M. J. (1997), Kinetic equations for diffusion controlled precipitation reactions, *J. Mater. Sci.*, vol. 32, pp. 4061–4070.

Steen, W. M. and C. Courtney (1979), Surface heat treatment of En8 steel using a 2 kW continuous wave CO_2 laser, *Metals Technol.*, vol. 6, pp. 456–462.

Stoker, H. C. (1999), *Developments of the arbitrary Lagrangian-Eulerian method in nonlinear solid mechanics*, Ph.D. thesis, University of Twente.

Stringfellow, R. G. and D. M. Parks (1991), A self-consistent model of isotropic viscoplastic behaviour in multiphase materials, *Int. J. Plast.*, vol. 7, pp. 529–547.

Thompson, E. G. and S. W. Yu (1990), A flow formulation for rate equilibrium equations, *Int. J. Numer. Meth. Engng.*, vol. 30, pp. 1619–1632.

Veaux, M., J. C. Louin, J. P. Houin, S. Denis, P. Archambault and E. Aeby-Gautier (2001), Bainitic transformation under stress in medium alloyed steels, *J. Phys IV*, vol. 11, pp. 181–188.

Verbeeten, W. M. H., A. C. B. Bogaers, G. W. M. Peters and F. P. T. Baaijens (1998), Computation of steady 3D viscoelastic flows using the DEVSS/DG method, in: J. Huétink and F. P. T. Baaijens (eds.), *Proceedings 6th Int. Conf. Num. Meth. in Industrial Forming Processes*, pp. 435–440, A.A. Balkema, Rotterdam.

Videau, J. C., G. Cailletaud and A. Pineau (1996), Experimental study of the transformation induced plasticity in a Cr-Ni-Mo-Al-Ti steel, *J. Phys. IV*, vol. 6 C1, pp. 465–474.

Wever, F. and A. Rose (1961), *Atlas zur Wärmebehandlung von Stähle, I Zeit Temperatur Umwandlungs Schaubilder*, Verlag Stahl Eisen MBH, Düsseldorf.

Wisselink, H. H. (2000), *Analysis of guillotining and slitting, finite element simulations*,

Ph.D. thesis, University of Twente.

Yu, Y., H. J. M. Geijselaers and J. Huétink (2001), A new displacement based formulation for steady state problems, in: K.-I. Mori (ed.), *Proceedings 7th Int. Conf. Num. Meth. in Industrial Forming Processes, NUMIFORM 2001*, pp. 121–126, A.A. Balkema, Rotterdam.

Zhao, J. C. and M. Notis (1995), Continuous cooling transformation kinetics versus isothermal transformation kinetics of steels: a phenomenological rationalization of experimental observations, *Mat. Sci. Engng.*, vol. R15, pp. 135–208.

Zienkiewicz, O. C., B. Boroomand and J. Z. Zhu (1999), Recovery procedures in error estimation and adaptivity part I: adaptivity in linear problems, *Comp. Meth. Appl. Mech. Engng.*, vol. 176, pp. 111–125.

Zienkiewicz, O. C. and R. L. Taylor (1991), *The Finite Element Method*, McGraw-Hill Book Company, 4 edn.

Zwigl, P. and D. C. Dunand (1997), A non-linear model for internal stress superplasticity, *Acta Mater.*, vol. 45, pp. 5285–5294.

Dankwoord

Allereerst wil ik Han Huétink bedanken voor zijn steun bij het tot stand komen van dit proefschrift. Hij was het, die het onderwerp aandroeg en die de weg wees hoe uit de verschillende onderwerpen een samenhangend proefschrift kon worden samengesteld.

De overige leden van mijn leescommissie, Jenö Beyer, Ton van den Boogaard, Harm Wisselink en Ruud van Damme dank ik voor de tijd, die zij besteed hebben aan het ordenen van de verschillende conceptversies van dit proefschrift. De opmerkingen en aanwijzingen van Katrina Emmett zijn de leesbaarheid van dit boek zeer ten goede gekomen.

Ook de studenten, waarvan het werk in enigerlij mate bijgedragen heeft aan dit proefschrift, Frank Odijk, Wietze Pieter Kikstra, Erik Sloot, Bastiaan Kleine-Döpke, Suzelot Kruyver en Richard Joustra wil ik hierbij danken.

De hulp van Tanja van Scherpenzeel en Debbie Zimmerman is voor mij van groot belang geweest. Zonder hun aandacht voor de organisatie romdom de promotie zou er niet veel van terecht zijn gekomen.

Henk Tijdeman bedank ik voor het in mij gestelde vertrouwen, uitgedrukt in een aanstelling bij zijn vakgroep. Mijn collegas, met name Henk ter Steege, Bert Wolbert en Ruud Spiering dank ik voor hun bereidwilligheid om in de aanloop tot mijn promotie delen van mijn onderwijstaak op zich te nemen.

De promovendi van de leerstoel, Jaap, Peter, Remko, Eisso, Gerrit, Herman, Bart, Ruth, Christiaan, Bert, Timo, Timo, Joeri, Hermen, Pieter, Gertjan, Yuhong, Loes en de medewerkers Marcel, Piet, Pieter, Nico, Herman, Kasper en Joop wil ik danken voor het goede gezelschap; zelfs wanneer het niet verheffend was, was het toch altijd inspirerend.

De vrienden van mijn fietsclub wil ik bedanken, voor het feit, dat zij, ondanks dat ik de laatste tijd te weinig trainingskilometers maakte, mij toch altijd zonder morren uit de wind hebben gehouden.

Tenslotte Karin, Liset en Irene, van nu af aan kan ik mij niet meer verbergen achter de smoes, dat dit boekje af moet. Bedankt voor jullie liefde, jullie steun en jullie geduld.

Bert Geijselaers
Hellendoorn, September 2003